Controlling light emission by dielectric metasurfaces

Dissertation
zur Erlangung des akademischen Grades
doctor rerum naturalium (Dr. rer. nat.)

vorgelegt dem Rat der Physikalisch-Astronomischen Fakultät
der Friedrich-Schiller-Universität Jena

von Master of Applied Physics and Mathematics Aleksandr Vaskin
geboren am 6. Juli 1992 in Perm, Russia

Gutachter:

1. Prof. Dr. 1
2. Prof. Dr. 2
3. Prof. Dr. 3

Tag der Disputation: ....

Contents

Chapter 1

Introduction

The electromagnetic spectrum covers wavelengths ranging from less than a fraction of the size of an atom up to more than thousands of kilometers and is divided into several bands: gamma rays, X-rays, ultraviolet (UV), visible, infrared (IR) and radio waves [1, 2]. The electromagnetic waves in these bands differ by how they interact with matter and, therefore, have distinct practical applications. To name a few, many medical diagnostic and treatment [3, 4], microfabrication [5] and inspection methods [6] rely on ultra-short wavelengths and high absorption of the gamma and X-rays, or the UV range, while the low atmospheric absorption of the radio waves makes them a good platform for long-range free-space communications [7].

A basic component of any radio communication system is the antenna [8–10], a device for receiving and transmitting of the radio waves. Nowadays, antennas are everywhere around us: in our homes establishing Wi-Fi networks, in our smartphones and laptops connecting people all over the planet, in satellites voyaging far above the world, and in numerous other devices. A key characteristic of the antenna performance is its radiation pattern, which describes angular dependence of the intensity of the emitted radio waves. While radio broadcasting requires an omnidirectional antenna to reach a wide audience, a typical radar utilizes a narrow scanning beam. To shape the antenna radiation pattern, one needs to control the electromagnetic fields on the sub-wavelength scale [10, 11].

According to Maxwell's equations, the same principles of directing electromagnetic waves can be applied at any wavelength [1, 2]. Progress in nanolithography over the last years makes it possible to fabricate nanometer-scale structures [12]. This allowed for scaling the radio antennas down to operate in the visible and IR spectral bands. These nanoscale analogues, namely nanoantennas [13–15], include Yagi-Uda antennas [16–24], as well as fixed [25–27] and even dynamic phased array antennas [28, 29]. The nanoantenna technology can potentially affect many aspects of our life. For example, a dynamic phased array nanoantenna is a key component of a solid state LiDAR [30] (light detection and ranging), a holy grail of the autonomous vehicles industry. It will be cheaper, faster, and providing higher resolution than a traditional LiDAR. Furthermore, the rapidly growing industry of Augmented and Virtual Reality (AR,VR) is actively seeking for a technology allowing for reproducing lights fields accurately. The AR and VR devices of the current generation project the images at a single virtual focal plane and therefore suffer from vergence-accommodation conflict. However, the pixels based on nanoantennas have

tunable radiation patterns and can potentially compose a light field display to overcome this problem [31].

Apart from the control over the free-space radiation, nanoantennas can confine the light in sub-wavelength volumes and provide effective light-matter interaction [32]. This principle plays a key role in applications such as nonlinear frequency generation [33–38], single-molecule detection [39, 40], quantum-light sources [41] and photovoltaics [42, 43]. Furthermore, they represent a new paradigm of improving the performance of solid-state lighting, which requires a precise control over quantum efficiency (QY), radiative and non-radiative decay rates and extraction of light [44–48].

Early research has been mainly focused on plasmonic nanoantennas, whose operation relies on the excitation of plasmonic resonances in metallic nanoparticles [49]. However, the high dissipative losses in metals limit the possible applications of the plasmonic nanoantennas. Therefore, all-dielectric nanoantennas have recently attracted an increasing amount of attention. High index dielectric materials, such as VI group materials (e.g. Si [50]), III-V materials (e.g. GaAs [38], AlGaAs [33, 34], GaP [51]), oxides (e.g. TiO_2 [52]) and perovskites [53] were suggested as promising materials for nanoantennas. They benefit from low dissipative losses in the visible range and provide the high values of QY. Most dielectric nanoantennas rely on multipolar Mie-type resonances [22, 54–56], which allow to tailor both the far-field properties and near-field enhancement. Interestingly, even dielectric nanoparticles of simple shapes like spheres or cylinders support strong multipolar resonances [50, 56–58]. In contrast, the multipolar response in plasmonic nanoantennas requires complex geometries [59].

Light-emitting metasurfaces

A metasurface is formally defined as a planar arrangement of building blocks designed to tailor the scattering of light impinging from the far-field [56, 60–62]. Metasurfaces promise complete control of the wavefront with a single layer of building blocks thinner than the wavelength, and therefore were suggested as flat and efficient blazed gratings [63], lenses [64–67], beam shapers [68–71] and holographic phase masks [72–75]. However, their potential to control not only the propagation - as in wavefront shaping applications - but also the emission of light at the nanoscale is far less established.

Light-emitting metasurfaces can be created by integrating emitters such as quantum dots (QDs) or dye molecules into the metasurface architecture. The key idea is that the building blocks can be designed to act as nanoantennas that efficiently couple the emission from the integrated nanoscale sources to the far-field while imprinting desired properties onto the emitted light field. Significant progress in developing light-emitting metasurfaces was achieved using arrays of resonant plasmonic nanoparticles [76–80]. Interestingly, apart from the localized resonances of the individual building blocks, these arrays also exhibit lattice resonances due to the in-plane coupling between the elements [81–86]. For example, Lozano et al. [27] demonstrated an enhanced directional emission from hexagonal arrays of resonant plasmonic nanoparticles deposited on top of a layer of organic fluorophores. The scanning electron microscopy (SEM) images of the plasmonic metasurfaces with different periodicity are shown in Figure 1.1 (a).

Back focal plane (BFP) imaging, revealed that the photoluminescence (PL) emission from the metasurface is strongly influenced by the lattice modes originating from the periodic arrangement. Furthermore, Langguth et al.[26] reported a plasmonic metasurface imparting an asymmetric directional pattern on the spontaneous emission (see Figure 1.1 (b)). While the lattice modes enabled directional out-coupling of light along a set of preferential directions, the predominance along a specific predefined (non-normal) direction was introduced by tailoring the scattering properties of the individual building blocks, namely dimers consisting of two aluminum nanorods of different length.

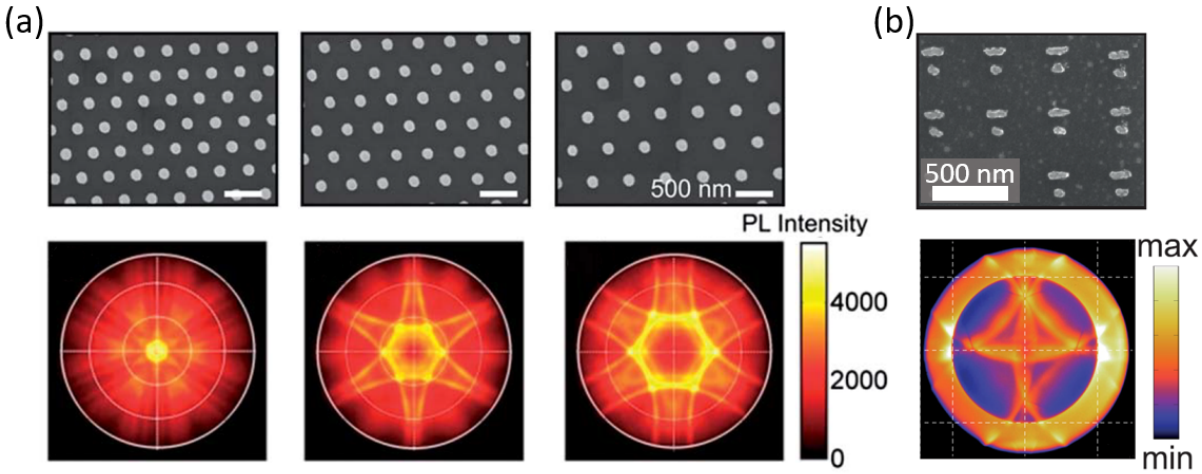

Figure 1.1: (a) Top row: SEM images of hexagonal aluminum nanoparticle arrays deposited on top of a layer of organic fluorophores. Periodicity of these arrays is 375, 425, and 475 nm, respectively. Bottom row: BFP images of the emission collected from the corresponding samples in the top row. Republished with permission of the Royal Society of Chemistry (Great Britain), from [27]; permission conveyed through Copyright Clearance Center, Inc. (b) Top: SEM image of a dimer array. Bottom: BFP image of the PL emission from dimer array for polarization aligned parallel to the rods. Reprinted with permission from L. Langguth, A. H. Schokker, K. Guo, and A. F. Koenderink, "Plasmonic phase-gradient metasurface for spontaneous emission control", Phys. Rev. B **92**, 205401 (2015); Copyright (2015) by the American Physical Society.

Dielectric metasurfaces

Similar to single nanoparticles, dielectric metasurfaces have been recently proposed as a low-loss alternative to plasmonic metasurfaces for tailoring the near- and far-fields. For example, as shown in Figure 1.2 (a) a periodic metasurface consisting of dielectric nanocylinders can inhibit the transmission of an incident plane wave at the wavelength of electric dipole (ED) or magnetic dipole (MD) Mie-type resonances. Furthermore, the nanocylinders can be tuned to exhibit both ED and MD resonances of equal strength at the same wavelength by adjusting their diameters [50]. This spectral overlap of the two resonances is called the Huygens' regime and provides near-unity transmittance, while providing full 2π-phase modulation of the transmitted plane wave [56] as the wavelength is swept over the spectral width of the resonances.

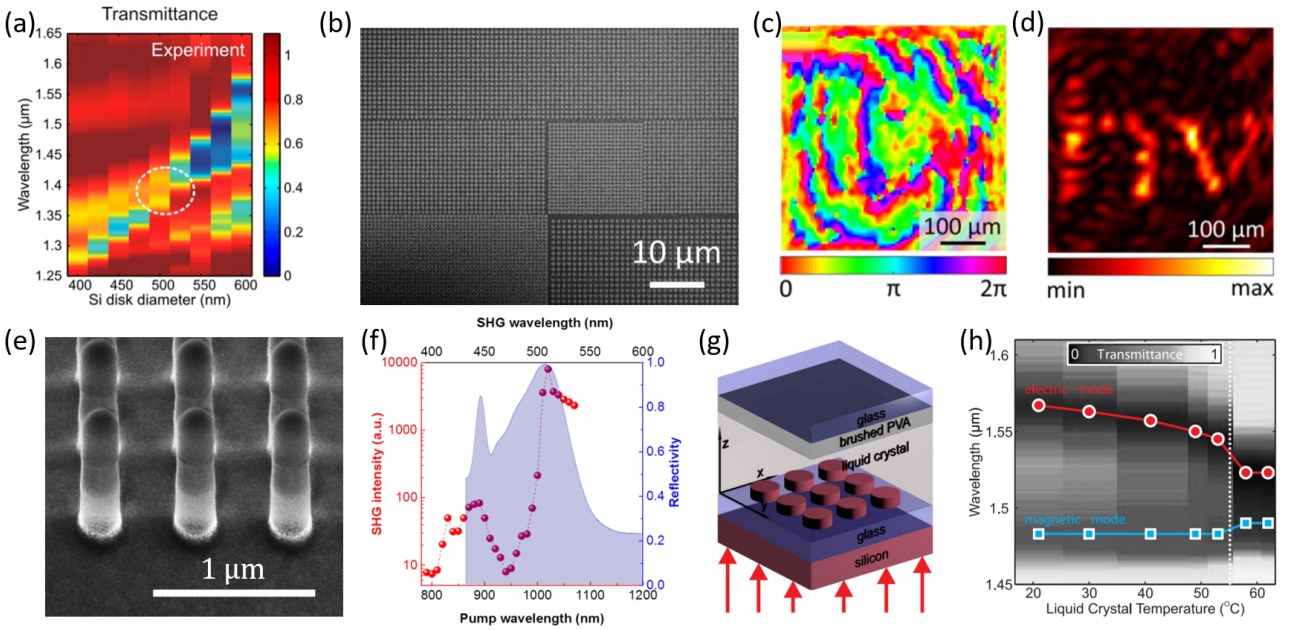

Figure 1.2: Applications of dielectric nanocylinder metasurface. (a) The modulation of the transmission spectra through metasurfaces with different nanocylinder diameters. (b) The pixelated metasurface creating a phase mask (c) and holographic image (d). (e) SEM image of the GaAs metasurface. (f) Resonantly enhanced second-harmonic generation from the GaAs metasurface. (g) Schematic of the dielectric nanocylinder metasurface covered by liquid crystal and (h) Transmittance spectra of the metasurface over a range of liquid crystal temperatures. (a) Reprinted with permission from [50]. Copyright (2013) American Chemical Society. (b-c) Reprinted with permission from [74]. Copyright (2016) American Chemical Society. (e,f) Reprinted with permission from [87]. Copyright (2017) American Chemical Society. (e,h) Reprinted with permission from [88]. Copyright (2015) American Chemical Society.

Since the Huygens' regime provides full-phase coverage combined with high efficiency in transmission, it offers a new route to design transmitting optical devices, such as flat optical components, holographic phase masks, and dispersion control devices [56]. The optical holography requires a metasurface to create a phase mask tailoring the far-field interference. Such metasurface [74] can be pixelated (see Figure 1.2 (b)) such that each pixel represents a smaller metasurface transmitting a plane wave with a certain relative phase. Taken together, all pixels form the phase mask shown in Figure 1.2 (c), which produces the holographic image shown in Figure 1.2 (d).

Apart from the far-field properties, Mie-resonances also enhance the near-fields. Since the enhanced near-fields are mostly localized inside the dielectric nanoresonators, Mie-resonances can significantly improve the interaction of light with the material of the nanoresonators enabling highly efficient nonlinear devices. For instance, Figure 1.2 (e,f) shows Mie-resonant GaAs metasurfaces that provide over 1000 times second-harmonic signal enhancement at the MD resonance [89] compared to a signal from GaAs wafer. In contrast to bulk nonlinear crystals, the nonlinear generation in the Mie-resonators happens at the sub-wavelength scale, which relaxes the phase-matching condition, thus allowing for the simultaneous occurrence of various nonlinear processes [36]. Furthermore, it is possible to design the resonators (for example, flat nanocylinders) such that the enhanced near-field leaks outside the nanocylinder. Thereby, the Mie-resonances become very sensitive to the refractive index of the surrounding media. This

effect allows for sensing, although, plasmonic nanoresonators can also be effective in this application [56]. However, the choice of dielectric material for the nanoresonators becomes crucial in liquid crystal tuning, because polar molecules of the liquid crystal induce image charges on the metal surface leading to anchoring effects and making the system less sensitive to the temperature or voltage switching. A work by Sautter et al. [88] demonstrates a metasurface composed of Mie-resonant silicon nanocylinders, whose wavelengths of ED and MD resonances could be actively controlled by the temperature of the liquid crystal placed on the metasurfaces (see Figure 1.2 (g,h)).

The aim of this thesis

The dielectric metasurfaces have been widely recognized as a low-loss platform allowing for manipulation of the near- and far-fields. However, the field of light-emitting dielectric metasurfaces is less developed. The main objective of this thesis is to demonstrate how dielectric metasurfaces can improve and control the emission of nanoscale light sources coupled to them. This includes experimental realization of coupled photonic systems consisting of emitters and dielectric metasurfaces, development of optical setups for characterization of the emission properties and numerical simulations to support the experimental data and to analyze the underlying physical mechanisms.

The thesis is structured as follows:

- Chapter 2 is dedicated to the fundamental physical concepts governing the response of dielectric metasurfaces. First, we focus on the individual building blocks. We introduce Mie theory and apply it to describe the properties of dielectric nanoparticles. Then, we analyze the collective effects originating due to coherent scattering in the arrangements of the resonant dielectric nanoparticles composing a metasurface. The last part of the chapter is dedicated to the physics of quantum emitters coupled to the metasurfaces.

- Chapter 3 focuses on the numerical methods used to simulate and analyze the optical properties of coupled photonic systems consisting of dielectric metasurfaces and emitters. We start with describing the general approaches for simulating the system performance. Importantly, we introduce a method based on the reciprocity principle, which was adapted by the author for calculating the emission patterns from the light-emitting dielectric metasurfaces. Then we introduce the multipole decomposition method allowing for identifying the nature of the resonances in the dielectric metasurfaces. Finally, we discuss the implementation of these methods in COMSOL Multiphysics package.

- Chapter 4 focuses on experimental techniques and fabrication of the dielectric nanostructures and for their consequent optical characterization. Most prominently, we describe the experimental setup for BFP imaging, which was built by the author during his doctoral studies.

- Chapter 5 explores the modification of the emission from various types of emitters coupled to dielectric metasurfaces and presents the results of the work done by the author during

his doctoral studies. First, we investigate a dielectric metasurface composed of silicon nanoantennas situated on a fluorescent glass substrate. We experimentally demonstrate the emission enhancement by the Mie-resonant dielectric nanoantennas in combination with out-of-plane directional emission due to the coherent scattering in a tailored periodic arrangement. Second, we study the light emission from a metasurface composed of III-V semiconductor nanoantennas with integrated QDs. In this system, we demonstrate the control over the angular emission distribution not only by tailoring the arrangement of the nanoantennas, but also by engineering the scattering properties of an individual nanoantenna. Next, in order to reach higher values of the PL signal enhancement, we engineer a metasurface that supports more complex high quality (Q) mode originating from the hybridization of a localized Mie and lattice resonances. This metasurface is composed of broken-symmetry III-V semiconductor nanoantennas with integrated QD. We demonstrate a strong PL signal enhancement by two orders of magnitude and emission pattern reshaping due to the coupling to this mode. Finally, we extend our study to the nanoscale sources exhibiting magnetic dipole transitions and investigate the possibility of using the dielectric metasurfaces for the enhancement of magnetic local density of states. For this reason, we cover the dielectric metasurfaces composed of silicon nanoantennas by a polymer doped by lanthanide ions exhibiting magnetic dipole transition in the visible. We demonstrate the enhancement of both electric and magnetic local densities of states through the excitation of Mie resonances in the metasurfaces. Interestingly, for selected parameters of the metasurface, it preferentially enhances the magnetic emission.

- Finally, Chapter 6 concludes the thesis and summarizes the results.

Chapter 2

Fundaments of dielectric metasurfaces

2.1 Optical properties of high-permittivity dielectric nanoparticles

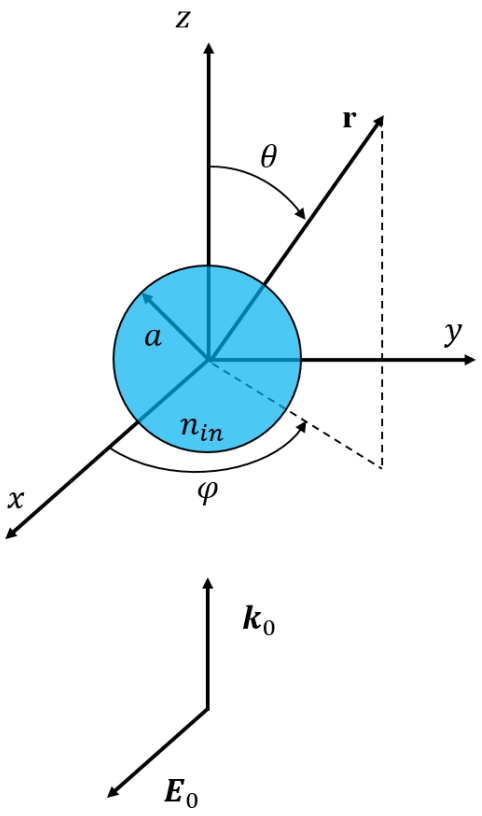

Figure 2.1: Sketch of the considered geometry. A plane wave with a wave vector $\mathbf{k}_0$ and electric field amplitude $\mathbf{E}_0$ is incident onto a spherical particle of radius a and refractive index n_{in} placed in the origin of a coordinate system.

Several scientists independently developed mathematical approaches to solve the problem of light scattering by a dielectric sphere [55]. Prominent contributions are done by Alfred Clebsch (1833 – 1872), Ludvig Lorenz (1829 – 1891), Gustav Mie (1868 – 1957) and Peter Debye (1884 – 1966). Gustav Mie was the first who successfully applied his theory to explain the

appearance of colours in solutions of metallic colloids. Therefore, most commonly the solution of this problem is referred to as Mie-theory [54], which provides the exact solution of Maxwell's equations.

In this paragraph, we consider a dielectric spherical particle with a radius a and complex refractive index n_{in}, placed in a homogeneous medium of complex refractive index n_o and illuminated by an x-polarized plane wave with a wavelength λ propagating along z-axis (see Figure 2.1).

Wave equation

The following analysis is adapted from [1, 90]. We start with macroscopic Maxwell's equations in differential form to describe the electromagnetic fields in a medium:

$$\nabla \times \mathbf{E}(\mathbf{r},t) + \frac{\partial \mathbf{B}(\mathbf{r},t)}{\partial t} = 0 \tag{2.1}$$

$$\nabla \times \mathbf{H}(\mathbf{r},t) - \frac{\partial \mathbf{D}(\mathbf{r},t)}{\partial t} = \mathbf{J}(\mathbf{r},t) \tag{2.2}$$

$$\nabla \cdot \mathbf{D}(\mathbf{r},t) = \rho(\mathbf{r},t) \tag{2.3}$$

$$\nabla \cdot \mathbf{B}(\mathbf{r},t) = 0 \tag{2.4}$$

and constitutive relations:

$$\mathbf{D}(\mathbf{r},t) = \varepsilon_0 \varepsilon(\mathbf{r},t)\mathbf{E}(\mathbf{r},t) \tag{2.5}$$

$$\mathbf{B}(\mathbf{r},t) = \mu_0 \mu(\mathbf{r},t)\mathbf{H}(\mathbf{r},t) \tag{2.6}$$

where $\varepsilon(\mathbf{r},t)$ and $\mu(\mathbf{r},t)$ are the relative permittivity and permeability tensors, respectively.

Next, we assume no sources are present and time harmonic fields ($\mathbf{E}(\mathbf{r},t) = \mathbf{E}(\mathbf{r})e^{-i\omega t}$). The Equations (2.1) to (2.4) now read as:

$$\nabla \times \mathbf{E}(\mathbf{r},\omega) - i\omega\mu_0 \mu(\mathbf{r},\omega)\mathbf{H}(\mathbf{r},\omega) = 0 \tag{2.7}$$

$$\nabla \times \mathbf{H}(\mathbf{r},\omega) + i\omega\varepsilon_0 \varepsilon(\mathbf{r},\omega)\mathbf{E}(\mathbf{r},\omega) = 0 \tag{2.8}$$

$$\nabla \cdot [\varepsilon(\mathbf{r},\omega)\mathbf{E}(\mathbf{r},\omega)] = 0 \tag{2.9}$$

$$\nabla \cdot [\mu(\mathbf{r},\omega)\mathbf{H}(\mathbf{r},\omega)] = 0 \tag{2.10}$$

We apply the operator $\nabla\times$ to the Equation (2.7): $\nabla\times(\nabla\times\mathbf{E}(\mathbf{r},\omega)) - i\omega\mu_0\nabla\times[\mu(\mathbf{r},\omega)\mathbf{H}(\mathbf{r},\omega)] = 0$. We exploit the relation $\nabla \times (\nabla \times \mathbf{E}) = \nabla(\nabla \cdot \mathbf{E}) - \Delta\mathbf{E}$ and consider the homogeneous non-magnetic medium in the visible to NIR spectral region: $\varepsilon(\mathbf{r},\omega) = \varepsilon(\omega)$ and $\mu(\mathbf{r},\omega) = 1$, so that $\nabla \times [\mu(\mathbf{r},\omega)\mathbf{H}(\mathbf{r},\omega)] = \nabla \times \mathbf{H}(\mathbf{r},\omega)$ and the Equation (2.9) reads as $\nabla \cdot \mathbf{E} = 0$. Now we can eliminate the magnetic field $\mathbf{H}(\mathbf{r},\omega)$ by substituting its curl using Equation (2.8). As the result, we obtain the vector wave equation for the electric field $\mathbf{E}(\mathbf{r},\omega)$:

$$\Delta\mathbf{E}(\mathbf{r},\omega) + k_0^2\varepsilon(\omega)\mathbf{E}(\mathbf{r},\omega) = 0 \tag{2.11}$$

The same approach can be used to derive the wave equation for the magnetic field $\mathbf{H}(\mathbf{r},\omega)$:

$$\Delta\mathbf{H}(\mathbf{r},\omega) + k_0^2\varepsilon(\omega)\mathbf{H}(\mathbf{r},\omega) = 0 \tag{2.12}$$

Both the electric and magnetic fields are divergence-free:

$$\nabla \cdot \mathbf{E}(\mathbf{r},\omega) = 0 \tag{2.13}$$

$$\nabla \cdot \mathbf{H}(\mathbf{r},\omega) = 0 \tag{2.14}$$

We further use the wave vector $k^2 = \varepsilon(\omega)k_0^2$, where $k_0 = \omega/c$ is the free-space wave vector.

Basis functions

In order to solve the vector wave Equations (2.11) and (2.12) in spherical coordinates (r,θ,ϕ), we introduce a scalar function $\psi(\mathbf{r})$ and make the following ansatz for a divergence-free vector function $\mathbf{M}(\mathbf{r})$:

$$\mathbf{M}(\mathbf{r}) = \nabla \times (\mathbf{r}\psi(\mathbf{r})) \tag{2.15}$$

We apply the operator $\Delta + k^2$ to the Equation (2.15):

$$\Delta\mathbf{M}(\mathbf{r}) + k^2\mathbf{M}(\mathbf{r}) = (\Delta + k^2)(\nabla \times (\mathbf{r}\psi(\mathbf{r}))) = \nabla(\Delta\psi(\mathbf{r}) + k^2\psi(\mathbf{r})) \times \mathbf{r} \tag{2.16}$$

Thereby, the sufficient condition for $\mathbf{M}(\mathbf{r})$ to satisfy the vector wave equation, is that $\psi(\mathbf{r})$ satisfies the scalar vector equation:

$$\Delta\psi(\mathbf{r}) + k^2\psi(\mathbf{r}) = 0 \tag{2.17}$$

The other solutions for $\nabla(\Delta\psi(\mathbf{r}) + k^2\psi(\mathbf{r})) \times \mathbf{r} = 0$ lead to $\mathbf{M}(\mathbf{r}) = 0$. We introduce another divergence-free vector function $\mathbf{N}(\mathbf{r})$:

$$\mathbf{N}(\mathbf{r}) = \frac{\nabla \times \mathbf{M}(\mathbf{r})}{k} \tag{2.18}$$

which satisfies the vector wave equation if $\mathbf{M}$ satisfies it. We expand the Equation (2.17) in spherical coordinates:

$$\frac{1}{r^2}\frac{\partial}{\partial r}\left(r^2\frac{\partial\psi}{\partial r}\right) + \frac{1}{r^2\sin\theta}\frac{\partial}{\partial\theta}\left(\sin\theta\frac{\partial\psi}{\partial\theta}\right) + \frac{1}{r^2\sin\theta}\frac{\partial^2\psi}{\partial\phi^2} + k^2\psi = 0 \tag{2.19}$$

Next, we attempt to find a solution of the Equation (2.19) by the separation of variables:

$$\psi(r,\theta,\phi) = R(r)\Theta(\theta)\Phi(\phi) \tag{2.20}$$

and substituting this particular solution in the Equation (2.19):

$$\frac{d}{dr}\left(r^2\frac{dR}{dr}\right) + [k^2r^2 - l(l+1)]R = 0 \tag{2.21}$$

$$\frac{1}{\sin\theta}\frac{d}{d\theta}\left(\sin\theta\frac{d\Theta}{d\theta}\right) + \left[l(l+1) - \frac{m^2}{\sin^2\theta}\right]\Theta = 0 \tag{2.22}$$

$$\frac{d^2\Phi}{d\phi^2} + m^2\Phi = 0 \tag{2.23}$$

We can solve each of the Equations (2.21) to (2.23) independently. The solution for the Equation (2.19) with the normalization coefficient can then be expressed as:

$$\psi_{lm}^{(n)}(r,\theta,\phi) = i^{l+1}(2l+1)\sqrt{\frac{1}{4l(l+1)}\frac{(l-m)!}{(l+m)!}}e^{im\phi}P_l^m(\cos\theta)z_l^{(n)}(kr) \tag{2.24}$$

where $l \in \{0,1,2...\}$ and $m \in \{-l,-l+1,...,l\}$, P_l^m are the associated Legendre functions of the first kind of degree l and order m, $z_l^{(n)}$ are the corresponding spherical Bessel or Hankel functions: $z_l^{(1)} = j_l, z_l^{(2)} = y_l, z_l^{(3)} = h_l^{(1)}$ or $z_l^{(4)} = h_l^{(2)}$. Note, that generally $z_l^{(n)}$ may be any linear combination of j_l and y_l.

Using the constructs that we introduced in the Equations (2.15) and (2.18), we can derive the vector spherical harmonics, which generate a complete basis for the solutions of the vector wave equation:

$$\mathbf{M}_{lm}^{(n)} = \nabla \times (\mathbf{r}\psi_{lm}^{(n)}) \tag{2.25}$$

$$\mathbf{N}_{lm}^{(n)} = (\nabla \times \mathbf{M}_{lm}^{(n)}(\mathbf{r}))/k \tag{2.26}$$

They fulfil the following orthogonality conditions:

$$\int_0^{2\pi}\int_0^{\pi}(\mathbf{M}_{l'm'}^{(n)})^* \cdot \mathbf{M}_{lm}^{(n)}\sin\theta d\theta d\phi = 0 \tag{2.27}$$

$$\int_0^{2\pi}\int_0^{\pi}(\mathbf{N}_{l'm'}^{(n)})^* \cdot \mathbf{N}_{lm}^{(n)}\sin\theta d\theta d\phi = 0 \tag{2.28}$$

for any $m \neq m'$ or $l \neq l'$ and

$$\int_0^{2\pi}\int_0^{\pi}(\mathbf{M}_{l'm'}^{(n)})^* \cdot \mathbf{N}_{lm}^{(n)}\sin\theta d\theta d\phi = 0 \tag{2.29}$$

for any m, l, m', l'.

The electromagnetic modes described by the functions $\mathbf{M}_{lm}^{(n)}$ and $\mathbf{N}_{lm}^{(n)}$ are called electric and magnetic (in analogy to Transverse Electric (TE) and Transverse Magnetic (TM) polarizations) dipole ($l = 1$), quadrupole ($l = 2$), octupole ($l = 3$), etc modes, respectively.

Expansion of the incident field

The spherical particle in Figure 2.1 is excited by an x-polarized plane wave:

$$\mathbf{E}_i = E_0 e^{ikr\cos\theta}\hat{\mathbf{x}}, \tag{2.30}$$

where $\hat{\mathbf{x}} = (\sin\theta\cos\phi, \cos\theta\cos\phi, -\sin\phi)$ is the unit vector along the positive x-axis.

We can expand the $\mathbf{E}_i(\mathbf{r})$ into an infinite series of the vector spherical harmonics:

$$\mathbf{E}_i = E_0 \sum_{l=0}^{\infty}\sum_{m=-l}^{l}(A_{lm}\mathbf{N}_{lm}^{(3)} + B_{lm}\mathbf{M}_{lm}^{(3)}), \tag{2.31}$$

with expansion coefficients:

$$A_{lm} = \frac{\int_0^{2\pi}\int_0^{\pi}(\mathbf{N}_{lm}^{(3)})^* \cdot \mathbf{E}_i \sin\theta d\theta d\phi}{E_0 \int_0^{2\pi}\int_0^{\pi}|\mathbf{N}_{lm}^{(3)}|^2 \sin\theta d\theta d\phi} \tag{2.32}$$

and analogue expressions for B_{lm}. Note that, since the electric field of the incident plane wave is finite at $\mathbf{r} = 0$, we reject the spherical Bessel functions of the second kind due to their singularity at the origin.

We then evaluate the integrals and obtain $A_{lm} = B_{lm} = 0$ for all $m \neq \pm 1$. The residual non-zero coefficients give us the expansion of the plane wave in spherical harmonics:

$$\mathbf{E}_i = E_0 \sum_{l=1}^{\infty}(\mathbf{N}_{l,1}^{(3)} - \mathbf{N}_{l,-1}^{(3)} + \mathbf{M}_{l,1}^{(3)} + \mathbf{M}_{l,-1}^{(3)}) \tag{2.33}$$

The internal and external fields

As it was shown above, the electromagnetic fields in a homogeneous medium can be expanded into infinite series of vector spherical harmonics. Now, we separate the geometry in the Figure 2.1 into two areas, inside and outside the sphere, each with a homogeneous refractive index.

The electric field outside the sphere is a sum of the incident plane wave $\mathbf{E}_i$ and the scattered field $\mathbf{E}_s$:

$$\mathbf{E}_{out} = \mathbf{E}_i + \mathbf{E}_s \tag{2.34}$$

$$\mathbf{H}_{out} = -\frac{i}{\omega\mu_0}\nabla \times \mathbf{E}_{out} \tag{2.35}$$

The scattered field $\mathbf{E}_s$ originates from the displacement currents excited in the sphere, so it follows the asymptotic of an outgoing spherical wave ($\sim \frac{e^{ikr}}{r}, r \to \infty$). Therefore, we have the following series for the scattered field $\mathbf{E}_s$:

$$\mathbf{E}_s = E_0 \sum_{l=0}^{\infty}\sum_{m=-l}^{l}(a_{lm}\mathbf{N}_{lm}^{(3)} + b_{lm}\mathbf{M}_{lm}^{(3)}) \tag{2.36}$$

The electromagnetic fields inside the sphere are:

$$\mathbf{E}_{in} = E_0 \sum_{l=0}^{\infty} \sum_{m=-l}^{l} \left(d_{lm} \mathbf{N}_{lm}^{(1)} + c_{lm} \mathbf{M}_{lm}^{(1)} \right) \tag{2.37}$$

$$\mathbf{H}_{in} = -\frac{i}{\omega \mu_0} \nabla \times \mathbf{E}_{in} \tag{2.38}$$

where we only considered the spherical Bessel functions of the first kind to avoid the singularity in the origin. At the boundary of the sphere (r=a), the external and internal fields must satisfy the boundary conditions:

$$(\mathbf{E}_{out} - \mathbf{E}_{in}) \times \hat{\mathbf{r}} = (\mathbf{H}_{out} - \mathbf{H}_{in}) \times \hat{\mathbf{r}} = 0, \tag{2.39}$$

where $\hat{\mathbf{r}}$ is the unit vector along $\mathbf{r}$. Based on the boundary condition (Equation (2.39)) and the orthogonality of the vector spherical harmonics we derive the exact expressions for the expansion coefficients:

$$a_{l,\pm 1} = \pm \frac{j_{l+\frac{1}{2}}(ak_0 n_i) \left(2ak_0 n_i^2 a j_{l+\frac{3}{2}}(ak_0) + \left(1 - 2(l+1)n_i^2\right) j_{l+\frac{1}{2}}(ak_0) \right) + ak_0 n_i j_{l+\frac{1}{2}}(ak_0) j_{l-\frac{1}{2}}(ak_0 n_i) - ak_0 n_i j_{l+\frac{1}{2}}(ak_0) j_{l+\frac{3}{2}}(ak_0 n_i)}{j_{l+\frac{1}{2}}(ak_0 n_i) \left(2ak_0 n_i^2 h^{(1)}_{l-\frac{1}{2}}(ak_0) - 2l\left(n_i^2 - 1\right) h^{(1)}_{l+\frac{1}{2}}(ak_0) \right) - 2ak_0 n_i h^{(1)}_{l+\frac{1}{2}}(ak_0) j_{l-\frac{1}{2}}(ak_0 n_i)} \tag{2.40}$$

$$b_{l,\pm 1} = \frac{\left(j_{l+\frac{3}{2}}(ak_0) - j_{l-\frac{1}{2}}(ak_0) \right) j_{l+\frac{1}{2}}(ak_0 n_i) + n_i j_{l+\frac{1}{2}}(ak_0) \left(j_{l-\frac{1}{2}}(ak_0 n_i) - j_{l+\frac{3}{2}}(ak_0 n_i) \right)}{2n_i h^{(1)}_{l+\frac{1}{2}}(ak_0) j_{l+\frac{3}{2}}(ak_0 n_i) - 2h^{(1)}_{l+\frac{3}{2}}(ak_0) j_{l+\frac{1}{2}}(ak_0 n_i)} \tag{2.41}$$

$$c_{l,\pm 1} = -\frac{4in_i}{\pi \sqrt{ak_0} \sqrt{ak_0 n_i} \left(n_i h^{(1)}_{l+\frac{1}{2}}(ak_0) \left(j_{l-\frac{1}{2}}(ak_0 n_i) - j_{l+\frac{3}{2}}(ak_0 n_i) \right) + \left(h^{(1)}_{l+\frac{3}{2}}(ak_0) - h^{(1)}_{l-\frac{1}{2}}(ak_0) \right) j_{l+\frac{1}{2}}(ak_0 n_i) \right)} \tag{2.42}$$

$$d_{l,\pm 1} = \pm \frac{2in_i \sqrt{ak_0 n_i}}{\pi \sqrt{ak_0} \left(ak_0 n_i^2 h^{(1)}_{l-\frac{1}{2}}(ak_0) j_{l+\frac{1}{2}}(ak_0 n_i) - h^{(1)}_{l+\frac{1}{2}}(ak_0) \left(l\left(n_i^2 - 1\right) j_{l+\frac{1}{2}}(ak_0 n_i) + ak_0 n_i j_{l-\frac{1}{2}}(ak_0 n_i) \right) \right)} \tag{2.43}$$

All coefficients with $m \neq \pm 1$ are equal to zero.

Scattering cross section

The scattered field $\mathbf{E}_s$ of an arbitrary scatterer in a homogeneous photonic environment can be decomposed in spherical harmonics in accordance with the Equation (2.36). We can estimate the corresponding time-averaged Poynting vector as:

$$\mathbf{S} = \frac{1}{2} \mathrm{Re}(\mathbf{E}_s \times \mathbf{H}_s^*) \tag{2.44}$$

The scattering cross section is the ratio of the scattered power and the incident light irradiance I:

$$C_{sc} = \frac{1}{I} \oiint_A \mathbf{S} \cdot d\mathbf{A} \tag{2.45}$$

where A is an arbitrary closed surface surrounding the scatterer and $d\mathbf{A}$ is a vector element of the surface.

Substituting the Equation (2.36) in the Equation (2.45) we can estimate the scattering cross section as a sum of the contributions from different multipolar modes excited in the scatterer:

$$C_{sc} = \frac{\pi}{k^2} \sum_{l=1}^{\infty} \sum_{m=-l}^{l} (2l+1)(|a_{l,m}|^2 + |b_{l,m}|^2) \tag{2.46}$$

Resonances of a dielectric sphere

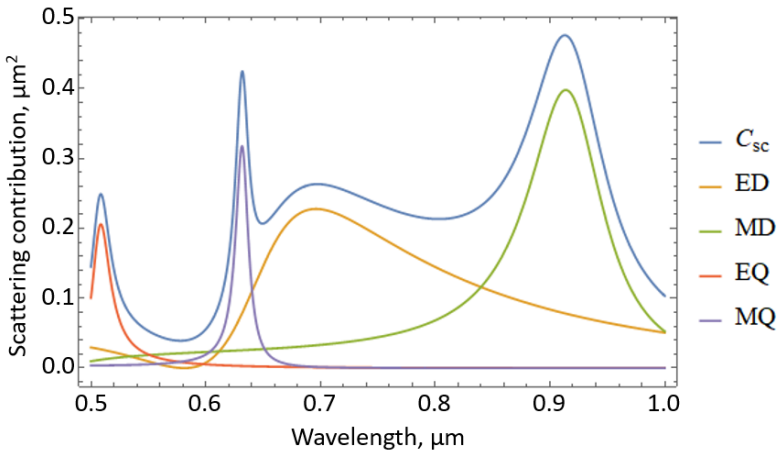

Figure 2.2: Scattering cross section as a function of the wavelength calculated according to the exact Mie-solution and the corresponding contributions of the electric dipole (ED) mode $\mathbf{N}^{(3)}_{1,\pm1}$, magnetic dipole (MD) mode $\mathbf{M}^{(3)}_{1,\pm1}$, electric quadrupole (EQ) mode $\mathbf{N}^{(3)}_{2,\pm1}$ and magnetic quadrupole (MQ) mode $\mathbf{M}^{(3)}_{2,\pm1}$.

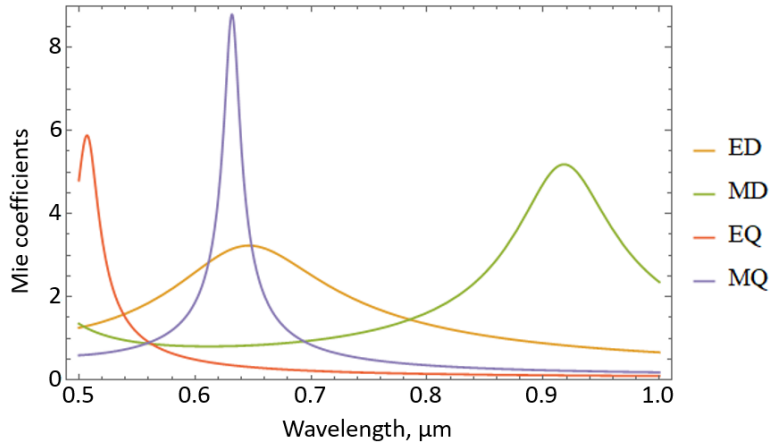

Figure 2.3: Amplitude of Mie-coefficients for inner fields for different modes: $d_{1,\pm1}$ (ED), $c_{1,\pm1}$ (MD), $d_{2,\pm1}$ (EQ) and $c_{2,\pm1}$ (MQ).

As an application example, we consider a sphere with radius $r = 0.125$ μm and constant refractive index $n_{in} = 3.5$ placed in a vacuum and illuminated by a plane wave with wavelength λ. The analytically calculated the total scattering cross section C_{sc} of the sphere is depicted in Figure 2.2. We observe four distinct peaks (Mie-resonances) distributed over the chosen wavelength range. The peak values of the scattering cross section are significantly enhanced compared to the geometrical cross section of the sphere of around 0.045 μm^2. We plot the

scattering contributions from electric dipole (ED) $\mathbf{N}^{(3)}_{1,\pm1}$, magnetic dipole (MD) $\mathbf{M}^{(3)}_{1,\pm1}$, electric quadrupole (EQ) $\mathbf{N}^{(3)}_{2,\pm1}$ and magnetic quadrupole (MQ) $\mathbf{M}^{(3)}_{2,\pm1}$ modes in the same Figure 2.2. The modes with higher l-number have a negligible contribution for the current sphere parameters and within the considered wavelength range. As one can notice, peaks in the C_{sc} spectrum are due to the resonant excitation of different Mie-modes.

Amplitudes of the Mie-coefficients of the fields excited inside the sphere (see Equation (2.37)) are displayed in Figure 2.3. The resonances observed in the far-field scattering C_{sc} are associated with the near-field resonances excited inside the sphere. However, the peak wavelengths can be slightly shifted due to the far-field coupling. The dipole resonances have lower Q-factor compared to the quadrupole resonances due to higher radiative losses.

Electric field profiles of dipole and quadrupole modes

As we have demonstrated, the far-field properties of the dielectric nanoparticles are defined by the modes excited in them. Later in this thesis, we introduce a multipole decomposition method for reliable and quantitative analysis of the origin of a particular far-field feature. However, each Mie-mode also has a specific electromagnetic field distribution, allowing for intuitive identification of the resonant mode by the appearance of the near-field profiles.

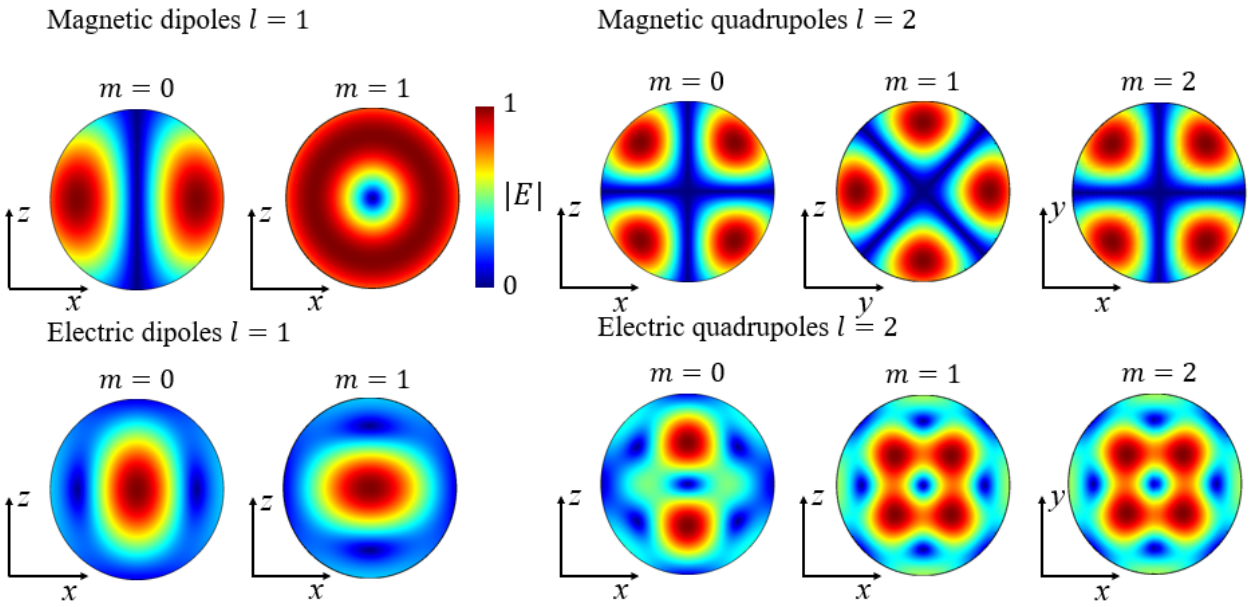

Figure 2.4: Electric field distribution $|\mathbf{E}|$ in the specified cross-section through the center of the sphere for different Mie Eigenmodes.

In Figure 2.4 we plot the distribution of the electric field amplitude $|\mathbf{E}|$ in the cross-sections through the center of the sphere for different electric $\mathbf{N}^{(1)}_{l,m}$ and magnetic $\mathbf{M}^{(1)}_{l,m}$ Eigenmodes at the corresponding resonant wavelengths. The l number characterizes the polar order and the m number characterizes the polar mode orientation. For example, an electric dipole mode with dipole moment along z-axis is composed of $\mathbf{N}^{(1)}_{1,0}$ and an electric dipole with dipole moment in $x-y$-plane $p(\cos\phi, \sin\phi, 0)$ is composed of two functions $\mathbf{N}^{(1)}_{1,1} - e^{2i\phi}\mathbf{N}^{(1)}_{1,-1}$. We observe that the electric (magnetic) dipole modes exhibit the maximum of the electric field amplitude

maximum (minimum) in the center of the sphere and a circulating magnetic (electric) current. The quadrupole modes have more complicated structure and exhibit four poles in the field distribution picture.

2.2 Directional radiation by nanoantennas

This section describes two concepts of tailoring the radiation patterns of nanoantennas. The first approach applies to the design of a single particle nanoantenna and relies on the coherent excitation of several multipolar modes in the particle [59, 91–94]. Alternatively, a nanoantenna can be composed of multiple particles, and the control over the far-field patterns is achieved through the arrangement of the elements [17, 28, 89, 95].

2.2.1 Directional radiation of a single particle nanoantenna

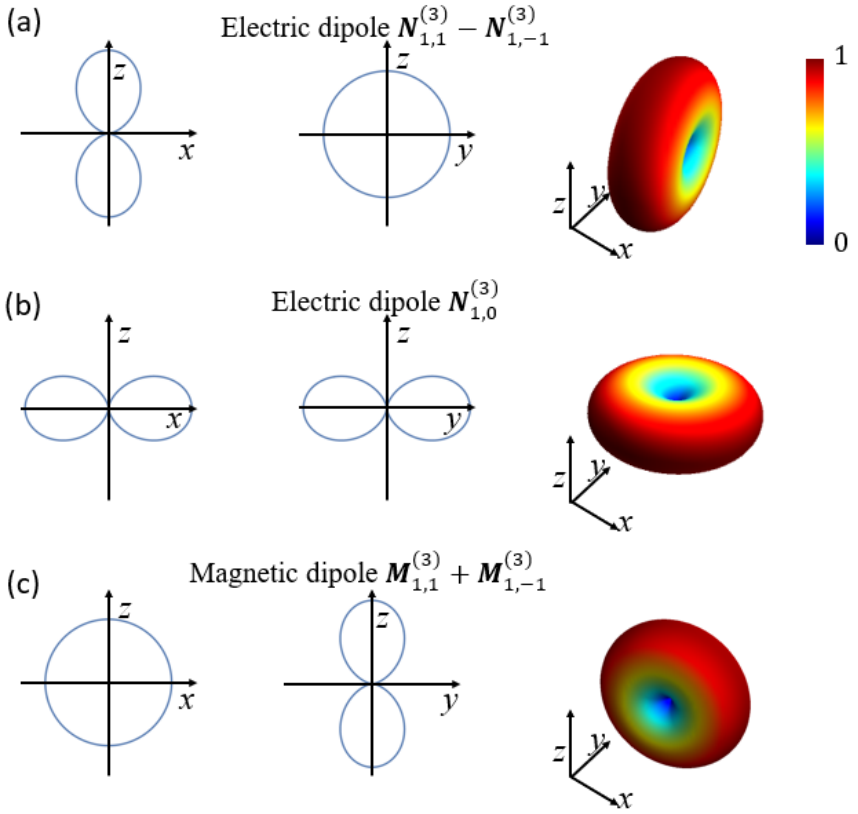

Figure 2.5: Angular radiation patters of exemplary dipolar Mie-modes. (a) ED mode with the dipole moment along the x-axis. (b) ED mode with the dipole moment along the z-axis. (c) MD mode with the dipole moment along the y-axis.

In this section we investigate the angular radiation characteristics attributed to a single or a set of Mie-modes induced in a nanoantenna. The radiation patterns are calculated using Equations (2.44) and (2.62) and demonstrate the angular distribution of the radiated power. In Figure 2.5 we depict the typical doughnut-shaped radiation patterns shared by the ED and MD modes of different orientations [1, 56]. In the 3D plots, color from blue to red indicates the normalized intensity of the radiated power. The radiation patterns of MQ modes are shown in Figure 2.6 and exhibit narrower lobes allowing for directional radiation into a reduced solid angle [56].

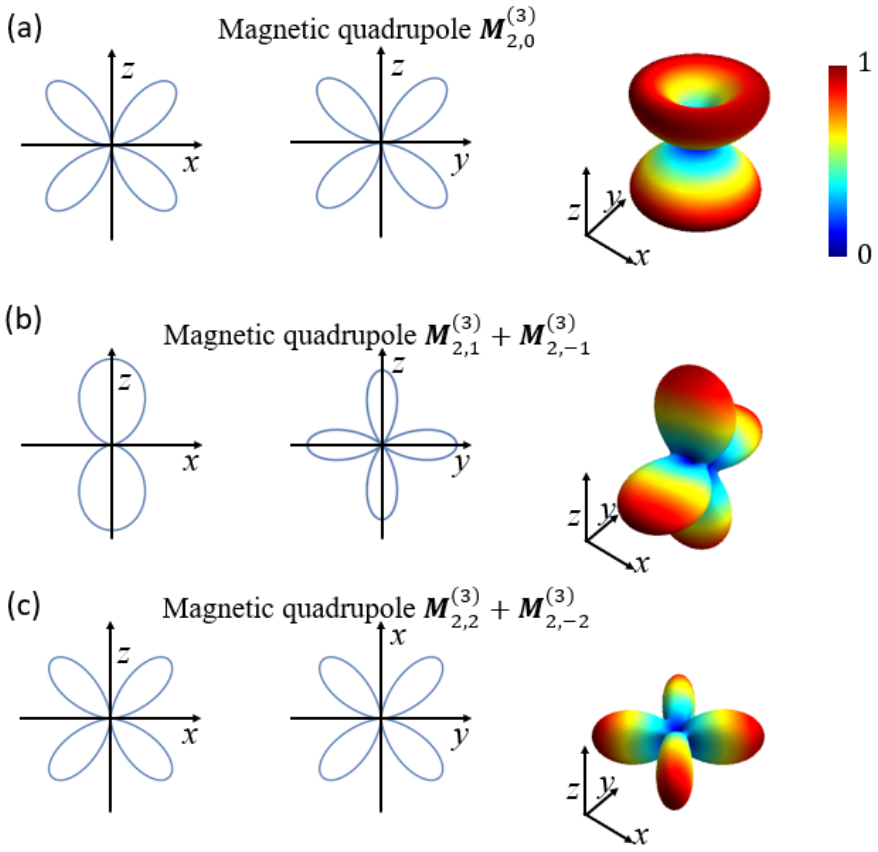

Figure 2.6: Angular radiation patters of the MQ modes with different m-number. (a) $m = 0$. (b) $m = \pm 1$. (c) $m = \pm 2$.

If different Mie-modes are simultaneously induced in a single nanoantenna, the radiation pattern will be shaped in accordance with the interference of the associated radiated fields [94]. For instance, the simultaneous excitation of the x-polarized ED and y-polarized MD modes of the same strength leads to the constructive interference in one direction and to destructive interference in the opposite direction (see Figure 2.7 (a)). This regime is known as the first Kerker condition [96] and can be employed to establish the Huygens' regime in the metasurfaces composed of such particles [50, 97]. The generalized Kerker condition can be fulfilled when the higher order electric and magnetic modes are excited. Figure 2.7 (b,c) show examples of radiation patterns obeying the generalized Kerker condition [98] involving the quadrupole modes. Apart from the suppression of the radiation along the $(0, 0, -1)$ direction, these patterns exhibit the directional radiation into a reduced solid angle.

Generally, the excitation of a desired set of Mie-modes by a plane wave at a certain wavelength can be achieved in dielectric nanoparticles with several geometrical degrees of freedom. For example, the Huygens' regime was demonstrated in a simple case of cylinder nanoparticles with just two degrees of freedom [50].

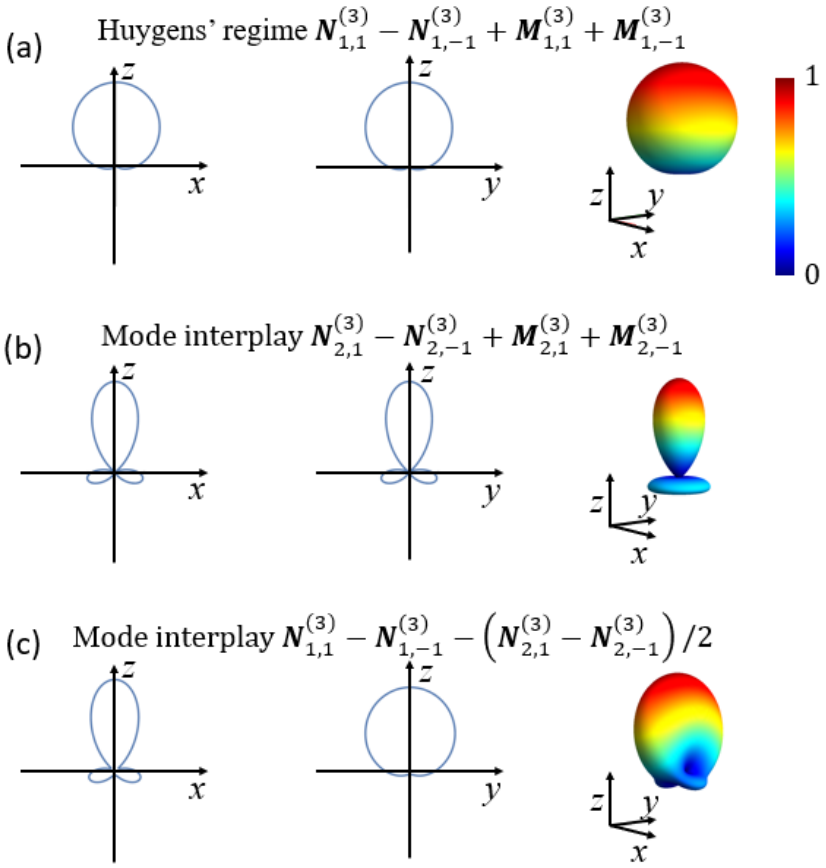

Figure 2.7: Angular radiation patters for the case of simultaneous excitation of several different Mie-modes obeying the generalized Kerker condition [96]. (a) First Kerker condition, when the equal contributions form ED and MD modes suppress the radiation in $(0, 0, -1)$ direction. (b) EQ and MQ modes suppress the radiation in the $(0, 0, -1)$ direction and squeeze the main lobe. (c) ED and EQ modes suppress the radiation in the $(0, 0, -1)$ direction.

2.2.2 Phased arrays

Another important concept of a system allowing to implement tailored far-field patterns is the phased array antenna (see Figure 2.8). A typical phased array antenna consists of several scattering elements. The elements are arranged and designed in a way that the interference of the light fields scattered by different elements results in the desired far-field pattern.

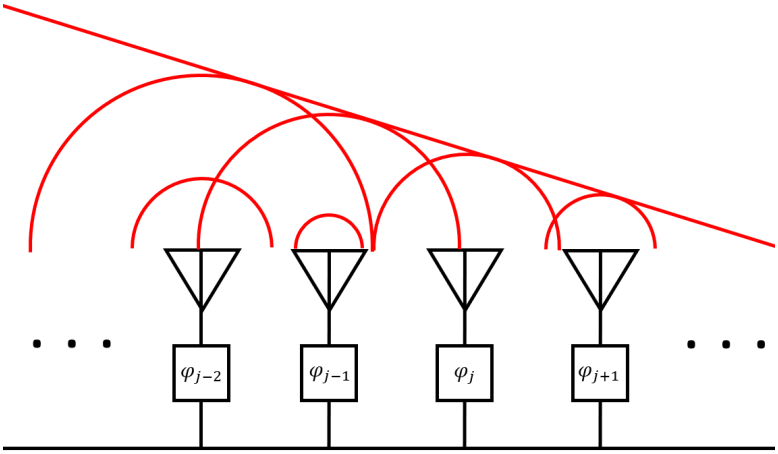

Figure 2.8: Schematic of a phased array antenna. The antenna consists of several scattering elements j. Each element scatters a spherical wave with a certain phase ϕ_j. The phase shift over the elements forms a beam steered in a desired direction.

The far-field $\mathbf{E}(\mathbf{k})$ of the phased array can be expressed as follows [45]:

$$\mathbf{E}(\mathbf{k}) = \frac{e^{ikR}}{R} \sum_j S_j(\mathbf{k}) \alpha_j E_{drive}(\mathbf{r}_j) e^{i\mathbf{k}\cdot\mathbf{r}_j}, \tag{2.47}$$

where R is the radius of the observation sphere ($R \gg$ size of the array), $\mathbf{k}$ is the wavevector in the direction of light propagation. $S_j(\mathbf{k})$ is the form factor of the scattering pattern, α_j is the polarizability and $\mathbf{r}_j$ is the position of the individual element j. $E_{drive}(\mathbf{r})$ is the driving field [25]. Note that Equation (2.47) is used as a didactic illustration of the main principles behind the formation of a certain far-field pattern. The accurate calculations of the far-field should be done by evaluating the Kirchhoff's integral.

The nanoscale phased array antennas were demonstrated in multiple platforms [21, 22, 28]. For example, Figure 2.9 illustrates the scanning electron microscopy (a) and the emission pattern (b) from an optical frequency Yagi-Uda antenna driven by localized QDs [17]. The antenna consists of gold nanoparticles operating near their plasmonic resonance. The variation in the nanoparticle size is implemented to tune the polarizability α_j and consequently, the phase of the scattered field. The fields scattered by different elements interfere constructively in forward direction (left to right) and destructively in backward direction (right to left) as shown in Figure 2.9 (b). The overall shape of the emission pattern is further affected by the angular scattering pattern of each individual element $S_j(\mathbf{k})$. Indeed, each element can be represented as a point electric dipole at the interface between air and substrate. The scattering pattern of such elements exhibit two main lobes directed into the substrate (see Figure 4.7 (b)).

Another illustration of the phased array antenna principle in optics is a metasurface beam deflector [99] depicted in Figure 2.9 (c). The metasurface consists of periodically arranged dielectric nanoparticles that are driven by a normally incident plane wave, i.e. with the same phase and amplitude. However, the nanoparticles have different sizes, as can be seen in Figure 2.9 (c), and thereby exhibit different polarizabilities. As the polarizability affects the amplitude and the phase of the scattered light, the metasurface acts as a blazed grating suppressing the zeroth-order transmission ($k_x = 0$) and directing the light into a desired diffraction order ($k_x = 0.33k_0$) as it is shown in Figure 2.9 (d).

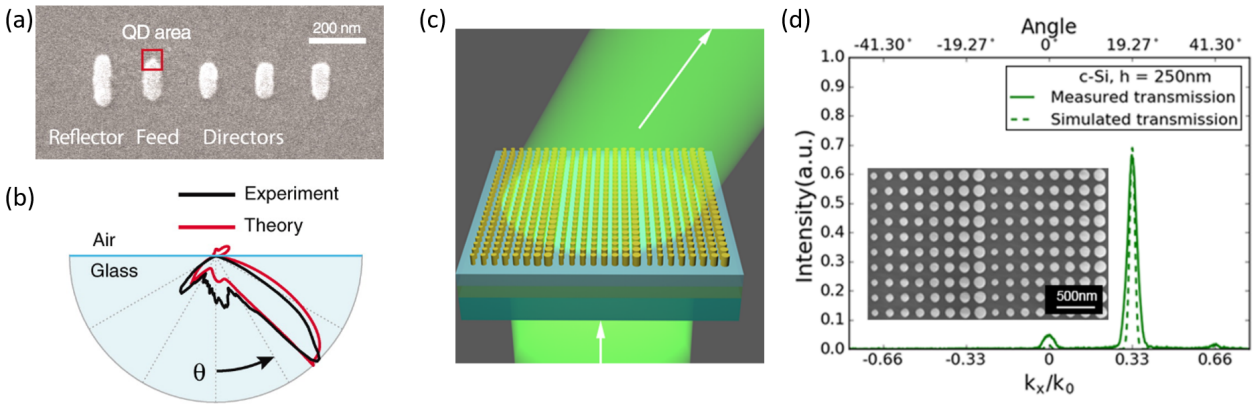

Figure 2.9: (a) Scanning electron microscopy (SEM) image of Yagi-Uda antenna driven by localized QDs. (b) Angular emission pattern in the polar angle θ for the Yagi-Uda antenna. (c) A sketch of metasurface acting as a beam deflector. (d) Angular scattering by the metasurface conceptually shown in (c). The inset shows the SEM of the fabricated metasurface. (a,b) Republished with permission of the American Association for the Advancement of Science, from [17] ; permission conveyed through Copyright Clearance Center, Inc. (c,d) Reprinted with permission from [99]. Copyright (2017) American Chemical Society.

Double cylinder nanoantenna

We can combine both principles of far-field engineering by composing a phased array antenna of directional elements. For example, in Liu et al. [87] we considered a nanoantenna made of two high-index dielectric nanocylinders separated by a layer of low-index oxide and driven by a point electric dipole. When a single nanocylinder is excited by a point electric dipole as depicted in Figure 2.10 (a), it exhibits a directional emission pattern as shown in Figure 2.10 (b). By stacking two of such nanocylinders as in Figure 2.10 (c) and optimizing the separation distance, we can improve the emission directionality by suppressing the parasitic lobes and slightly squeezing the main lobe as shown in Figure 2.10 (d). The fraction of the emission integrated over the directions within the backward semi-sphere was reduced from 42% to 24%.

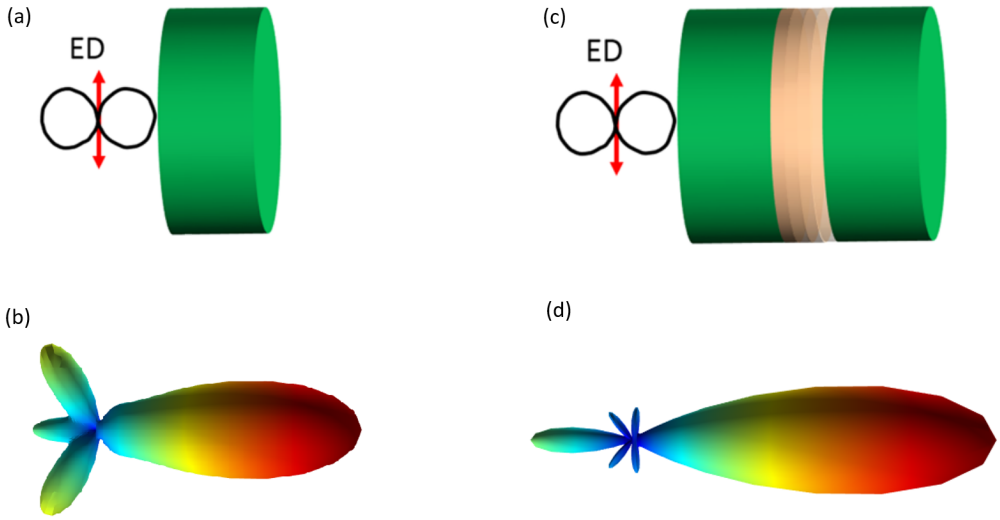

Figure 2.10: (a) Schematic of a single high-index nanocylinder driven by point electric dipole (ED). (b) Corresponding emission pattern at a wavelength of 990 nm. (c) Schematic of a two adjusted high-index nanocylinders driven by point electric dipole (ED). (d) Corresponding emission pattern at a wavelength of 990 nm. Reprinted with permission from [87]. Copyright (2017) American Chemical Society.

2.3 Collective resonances in dielectric metasurfaces

2.3.1 General considerations for collective resonances

In periodic metasurfaces, apart from the localized resonances of the building blocks, hybrid resonances occur due to the strong coupling of collective oscillations of the lattice and individual polarizabilities [82, 84, 100].

To understand this hybridization, we consider a periodic lattice driven by a plane wave [81, 100, 101]. The induced dipole moment of the i-th particle $\mathbf{P}_i$ is determined as a bare polarizability $\hat{\alpha}$ acting on a background field $\mathbf{E}_i^{bg}$. We also introduce the effective polarizability $\hat{\alpha}^{eff}$ that connects the induced dipole moment with the incident field $\mathbf{E}_i^0$:

$$\mathbf{P}_i = \hat{\alpha}\mathbf{E}_i^{bg} = \hat{\alpha}^{eff}\mathbf{E}_i^0, \tag{2.48}$$

The background field is the sum of the incident field and the field scattered by the dipole moments $\mathbf{P}_j$ induced in other resonators:

$$\mathbf{E}_i^{bg} = \mathbf{E}_i^0 + \sum_{j\neq i} \hat{G}(\mathbf{r}_i, \mathbf{r}_j)\mathbf{P}_j, \tag{2.49}$$

where $\hat{G}(\mathbf{r}_i, \mathbf{r}_j)$ is a Green's function describing the electric field induced at the position $\mathbf{r}_i$ by a dipole placed at the coordinate $\mathbf{r}_j$ in the considered photonic environment. The sum is taken over all resonators except for the i-th.

The effective polarizability can finally be derived as:

$$\hat{\alpha}^{eff} = (\hat{\alpha}^{-1} - \hat{C}(\mathbf{k}_{||}))^{-1}, \tag{2.50}$$

where $\hat{C}(\mathbf{k}_{||}) = \sum_{j\neq i} \hat{G}(\mathbf{r}_i, \mathbf{r}_j)e^{-i\mathbf{k}_{||}(\mathbf{r}_i - \mathbf{r}_j)}$ is the term describing the interactions between the particles. The parallel momentum $\mathbf{k}_{||}$ is the in-plane component of the wavevector of the incident plane wave.

The effective polarizability describes the hybridization between the lattice and localized resonances. To illustrate this, we depict the absolute values of $\hat{\alpha}$, $\hat{C}(\mathbf{k}_{||})$ and $\hat{\alpha}^{eff}$ in Figure 2.11. As an example of the bare polarizability representing a localized resonance, we used a Lorentzian with a resonant wavelength of 1260 nm (see Figure 2.11 (a)). The Q-factor of the resonance is around 10, which is typical for ED and MD resonances (see Figure 2.2). We observe no dependence on the parallel momentum. The second term $\hat{C}(\mathbf{k}_{||})$ shown in Figure 2.11 (b) describes the lattice resonances of a 1D periodic arrangement of particles with 1000 nm spacing placed in vacuum. The resonances due to the collective effects in the lattice have a strong dependence on the parallel momentum and are very sharp as the energy is stored within the lattice and the radiation losses are suppressed. In the hybridization regime shown in Figure 2.11 (c), Fano features arise due to the interference of the sharp lattice and broad localized resonances. The hybridized resonance exhibits characteristic features of strong coupling such as bendings and anticrossings arise [100, 102, 103].

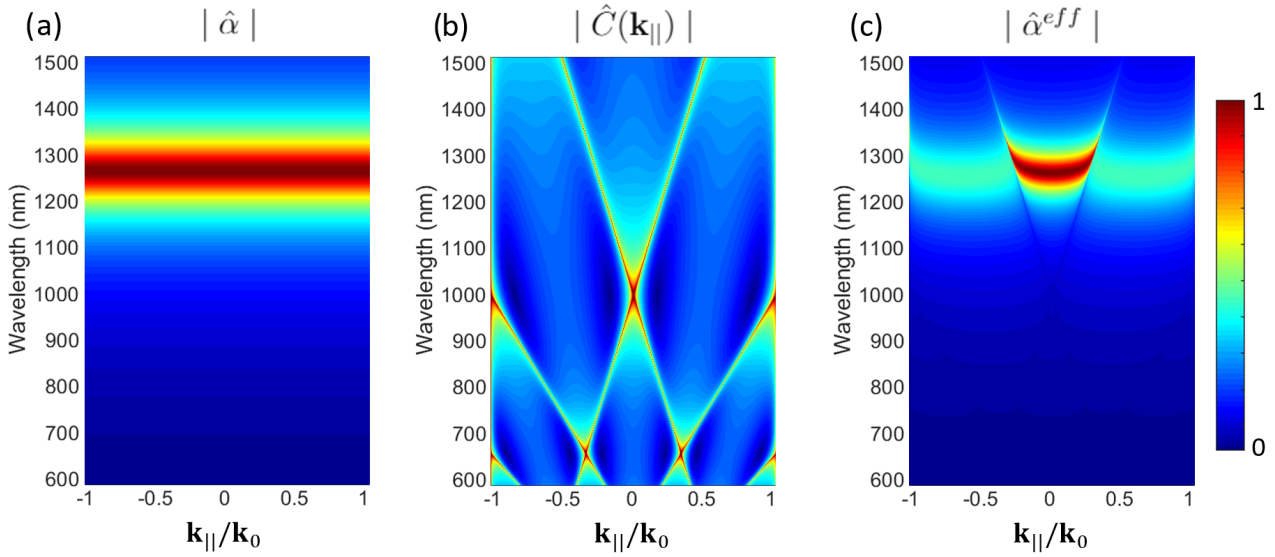

Figure 2.11: Absolute values of (a) the bare polarizability $\hat{\alpha}$, (b) the term describing interactions between the particles $\hat{C}(\mathbf{k}_{||})$, (c) the effective polarizability $\hat{\alpha}^{eff}$.

The considerations above assumed only dipole-dipole interactions and are accurate only if the background field doesn't change significantly at the scale of the nanoparticle size. To solve the general case of the self-consistent scattering problem, robust methods taking into account higher order multipolar interactions were suggested [104–108].

2.3.2 Out-of-plane dipole resonances

In this section we discuss a notable case of hybridized out-of-plane MD and lattice modes [109–112]. We consider a metasurface which is composed of cubic dielectric resonators and periodic in x and y directions. A normally incident (along z-axis) plane wave has electric and magnetic field vectors in the $x-y$-plane. Therefore, it can excite the ED and MD modes with dipole moments parallel to the same plane. We call these modes in-plane dipole modes and Figure 2.5 (a,c) illustrates their scattering patterns. Such modes effectively scatter the light along the z-axis, which then couples to zero-order reflection or transmission or higher diffraction orders.

Under the oblique incidence, in contrast, the incident plane wave gives rise to the z-components of the electric (TM polarization) or magnetic (TE polarization) field vectors of the incident plane wave. Under these conditions, it becomes possible to also excite the modes with the dipole moment along the z-axis (out-of-plane dipole modes). The corresponding scattering pattern is shown in Figure 2.5 (b). Most of the light is scattered along the metasurface. This fact leads to more pronounced hybridization between the dipolar Mie- and the lattice modes, since the energy transfer, and thus the coupling of the modes, is more effective. Furthermore, the electromagnetic energy is stored within the metasurface and the radiation losses are suppressed. Consequently, such hybridized modes exhibit high Q-factors.

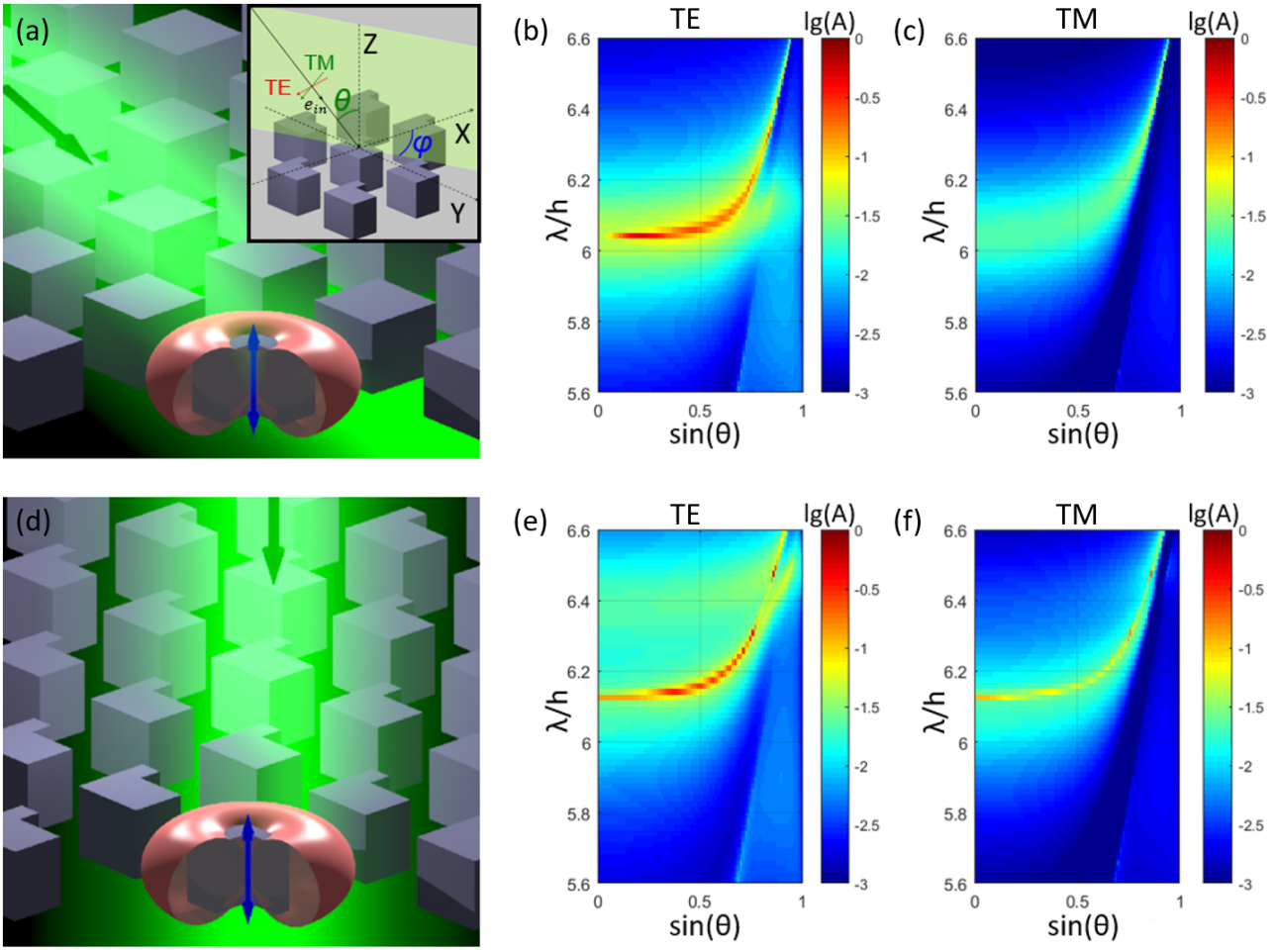

Figure 2.12: In-plane and out-of-plane MD resonances. (a) Sketch of a symmetric metasurface (not to scale). The inset illustrates the coordinate system that denotes the angles of incidence. (b,c) Calculated absorbance spectra of the metasurface depicted in (a) for TE and TM polarized incident plane waves, respectively, for a variation of the polar angle θ. The azimuthal angle ϕ is kept equal to 0°. The out-of-plane MD mode appears as a narrow band of enhanced absorption in (b) and can only be excited for TE polarized light and oblique-incidence. (d) Sketch of a symmetry-broken dielectric metasurface (not to scale). (e,f) Calculated absorbance spectra of the metasurface depicted in (d) for TE and TM polarized incident light, respectively, for a variation of the polar angle θ. The azimuthal angle ϕ is kept equal to 0°. The out-of-plane MD mode now appears as a narrow band of strong absorption both for TE and TM polarized light. The symmetry break also allows for excitation of the out-of-plane MD mode at normal incidence. Reprinted with permission from [111]. Copyright (2018) American Chemical Society.

We performed numerical simulations of the angular-dependent absorption (A) spectra of Mie-resonant metasurfaces to demonstrate the out-of-plane MD mode and investigate the excitation conditions. First, we consider a metasurface with a period of 4000 nm consisting of cubic resonators having the same width, depth and height of 1200 nm (see Figure 2.12 (a)). The inset illustrates the coordinate system that defines the angles of incidence and is used later in this thesis. The refractive index of the resonators was $5 + 0.001i$, and the refractive index of the surrounding medium is 1. The TE or TM polarized plane wave is incident onto the structure at the polar angle θ, which is varied from 0° to 90°. In Figure 2.12 (b,c) we observe the excitation of a broad MD mode with an in-plane dipole moment for both polarizations. In addition, for oblique incidence and TE polarization (Figure 2.12 (b)), we excite a high-Q out-of-plane MD mode leading to the significantly enhanced absorption. Since the out-of-plane MD mode

doesn't scatter any light along the normal direction (z-axis), by reciprocity this mode is not excited for normal incidence. Therefore, the absorption band is interrupted at $\theta = 0°$.

The excitation conditions of the out-of-plane modes can be altered by breaking the symmetry of the Mie-resonators. To illustrate this point, we consider another metasurface, which consists of resonators having a rectangular $1000 \times 400\,\mathrm{nm}^2$ region removed at one of the corners (see Figure 2.12 (d)). The width and depth of these resonators are increased to 1460 nm. This notch introduces intermode coupling between the in-plane and out-of-plane dipole modes and allows for the excitation of the high-Q out-of-plane MD mode for any angle of incidence and polarization as shown in Figure 2.12 (e,f).

2.4 Light-emitting metasurfaces

2.4.1 Quantum emitters

Controlling and enhancing the emission from metasurfaces is at the heart of this thesis. Light-emitting metasurfaces can be fabricated by integrating emitters into the metasurface architecture. Apart from tailoring the far-field properties of the emission, the near-field enhanced by metasurfaces leads to the modification of the local density of optical states (LDOS) and affects the decay rate of the emitters [113]. This effect was first observed by Edward Mills Purcell in high-Q resonant cavities [114] and, therefore, is often referred to as the Purcell effect and the ratio between the enhancement LDOS and the free-space LDOS is called the Purcell factor.

To explain the influence of the metasurface, we consider an atom in an external electromagnetic field. The Hamiltonian of the system is [113, 115]:

$$\hat{H} = \hat{H}_A + \hat{H}_F + \hat{H}_{A-F} \tag{2.51}$$

where $\hat{H}_A$ is the Hamiltonian of the atom in the absence of the external electromagnetic field, $\hat{H}_F$ is the Hamiltonian of the electromagnetic field in the absence of the atom and $\hat{H}_{A-F}$ is the interaction Hamiltonian. We use multipole expansion of the interaction Hamiltonian:

$$\hat{H}_{A-F} = -\hat{\mathbf{p}} \cdot \hat{\mathbf{E}} - \hat{\mathbf{m}} \cdot \hat{\mathbf{B}} - [\hat{Q}\nabla] \cdot \hat{\mathbf{E}} - ... \tag{2.52}$$

where the electric dipole moment $\hat{\mathbf{p}}$, the magnetic dipole moment $\hat{\mathbf{m}}$, and the electric quadrupole moment $\hat{Q}$ [115] (and so on) terms correspond to different multipolar moments of the electronic charge distribution.

The interaction Hamiltonian mediates the transition rate Γ between the initial state $|i\rangle$ and the final state $|f\rangle$ of the atom following the Fermi's golden rule:

$$\Gamma = \frac{2\pi}{\hbar^2} \mid \langle f | \hat{H}_{A-F} | i \rangle \mid^2 g(\omega) \tag{2.53}$$

where $g(\omega)$ is the density of photon states at the energy $\hbar\omega = \langle i | \hat{H}_A | i \rangle / \langle i | i \rangle - \langle f | \hat{H}_A | f \rangle / \langle f | f \rangle$.

A simple particle-in-a-box model demonstrates that in order to have an emission of the photon with a frequency in the visible or NIR spectral range due to the transition between the eigenstates, the electron confinement scale should be in a range of a few nanometers [14]. Using the Bohr model of the atom, we can estimate that the electric dipole term has a dominant contribution due to this strong wavelength-size mismatch [116]. Therefore, most of the transitions leading to spontaneous emission are electric dipole transitions. However, for certain initial and final states, the integral $\langle f | -\hat{\mathbf{p}} \cdot \hat{\mathbf{E}} | i \rangle$ vanishes [117]. This effect is described by selection rules, which forbid the electric dipole (or any other) transition between certain electronic states and gives rise to the higher order multipolar transitions.

The Fermi's golden rule for the electric dipole transition can be formulated as:

$$\Gamma = \frac{2\pi}{\hbar^2} \mid \langle f | -\hat{\mathbf{p}} \cdot \hat{\mathbf{E}} | i \rangle \mid^2 \rho^e(\mathbf{r}_0, \omega) \tag{2.54}$$

where $\rho^e(\mathbf{r}_0, \omega)$ is the electric LDOS defined by the photonic environment:

$$\rho^e(\mathbf{r}_0, \omega) = \frac{2\omega_0}{\pi c^2} \mathbf{n} \cdot \mathfrak{Im}\{\hat{G}^{(e)}(\mathbf{r}_0, \mathbf{r}_0, \omega_0)\} \cdot \mathbf{n} \tag{2.55}$$

where $\hat{G}^{(e)}(\mathbf{r}_i, \mathbf{r}_j, \omega_0)$ is the Green's function, which describes the electric field induced at the position $\mathbf{r}_i$ by an electric dipole oscillating at the frequency ω placed at the coordinate $\mathbf{r}_j$ in the considered photonic environment.

For the magnetic dipole transition Fermi's Golden rule reads:

$$\Gamma = \frac{2\pi}{\hbar^2} \mid \langle f \mid - \hat{\mathbf{m}} \cdot \hat{\mathbf{B}} \mid i \rangle \mid^2 \rho^m(\mathbf{r}_0, \omega) \tag{2.56}$$

Here, $\rho^m(\mathbf{r}_0, \omega)$ is the magnetic LDOS defined by the photonic environment:

$$\rho^m(\mathbf{r}_0, \omega) = \frac{2\omega_0}{\pi c^2} \mathbf{n} \cdot \mathfrak{Im}\{\hat{G}^{(m)}(\mathbf{r}_0, \mathbf{r}_0, \omega_0)\} \cdot \mathbf{n} \tag{2.57}$$

where $\hat{G}^{(m)}(\mathbf{r}_i, \mathbf{r}_j, \omega_0)$ is the Green's function, which describes the magnetic field induced at the position $\mathbf{r}_i$ by a magnetic dipole oscillating at the frequency ω placed at the coordinate $\mathbf{r}_j$ in the considered photonic environment, and $\mathbf{n}$ is the unit vector in the direction of the emitting dipole moment [118].

An experimental demonstration of the modification of the electric and magnetic LDOS by the photonic environment and the resulting influence on the transition rates was done by Karaveli et al. [119], who repeated the Drexhage experiment using trivalent Europium ions (Eu^{3+}) exhibiting both electric and magnetic dipole transitions in the visible spectral range.

2.4.2 Emitters coupled to a metasurface

When a single emitter is coupled to a metasurface, the measured PL signal (intensity, count rate) from the system will be determined by four factors [15, 45, 120]:

$$I(\mathbf{r}_{em}, \omega_{exc}, \omega_{em}) \propto \Gamma_{exc}(\mathbf{r}_{em}, \omega_{exc}) \cdot QY(\mathbf{r}_{em}, \omega_{em}) \cdot \eta_{ext}(\mathbf{r}_{em}, \omega_{em}) \cdot \eta_{coll}(\mathbf{r}_{em}, \omega_{em}), \tag{2.58}$$

where $\mathbf{r}_{em}$ is the position of the emitter integrated into the metasurface, ω_{exc} is the frequency of the excitation field and ω_{em} is the frequency of the emission.

The first term describes the excitation rate Γ_{exc}, which can be improved by the metasurface. Indeed, the metasurface, being illuminated by the excitation field, can produce enhanced near-fields. An emitter placed on the metasurface will then be exposed to these enhanced near-fields resulting in an effective interaction of the excitation field with the emitter [27, 44]. For an isotropic emitter at position $\mathbf{r}_{em}$, the excitation rate enhancement is $\Gamma_{exc}(\mathbf{r}_{em}, \omega_{exc})/\Gamma^0_{exc} = \mid \mathbf{E}(\mathbf{r}_{em}, \omega_{exc}) \mid^2 / \mid \mathbf{E}_0 \mid^2$, where Γ^0_{exc} is the excitation rate of the emitter in vacuum, $\mathbf{E}_0$ is the electric field of the excitation, and $\mathbf{E}(\mathbf{r}_{em}, \omega_{exc})$ is the electric field at the position $\mathbf{r}_{em}$ [113]. Note that such estimation of the excitation rate enhancement is only valid in the weak excitation regime, when the PL signal stays proportional to the excitation power.

Once the emitter is excited, it can decay upon emitting a photon at the Stokes-shifted

frequency (ω_{em}) at a radiative decay rate Γ^0_{rad} or without emitting the photon following intramolecular dissipation with a decay rate Γ^0_i. These two rates define an intrinsic QY of the emitter as $QY^0 = \Gamma^0_{rad}/(\Gamma^0_{rad} + \Gamma^0_i)$. If the emitter is coupled to a metasurface, the decay rate Γ^0_{rad} of the radiative channel will be modified to Γ in accordance with Fermi's Golden Rule (see Equation (2.54)). The decay rate Γ is a sum of a radiative decay rate Γ_{rad} and a non-radiative decay rate Γ_{nr} corresponding to quenching. The modified QY is $QY = \Gamma_{rad}/(\Gamma_{rad} + \Gamma_{nr} + \Gamma^0_i)$.

The decay rate enhancement can be estimated using classical electromagnetic simulations due to the fact that the enhancement of the decay rate Γ of the emitter by the photonic environment is related to the enhancement of the power P_d dissipated by a classical point electric dipole $\mathbf{p}_{em}$ placed in the same photonic environment: $P_d/P^0_d = \Gamma/\Gamma^0_{rad}$ [13, 113, 121]. We apply the Poynting's theorem to reveal the classical mechanism of the radiated power enhancement [113, 122]. When $\mathbf{p}_{em}$ is placed in the vicinity of a metasurface it is affected by its own field scattered back and enhanced by the nanostructure. The associated power can be calculated as:

$$\frac{P_d}{P^0_d} = 1 + \frac{6\pi\varepsilon\varepsilon_0}{\mid \mathbf{p}_{em} \mid^2}\frac{1}{k^3}\mathfrak{Im}\{\mathbf{p}^*_{em} \cdot \mathbf{E}_{scat}(\mathbf{r}_{em}, \omega_{em})\}, \tag{2.59}$$

where $\mathbf{E}_{scat}(\mathbf{r}_{em}, \omega_{em})$ is the scattered electric field excited by the dipole $\mathbf{p}_{em}$, oscillating at the frequency ω_{em} and placed in $\mathbf{r}_{em}$, P^0_d is the power radiated by the emitter placed in vacuum. The power P_d dissipated by the dipole is the sum of the radiated power P_{rad} and the power P_{loss} quenched due to Ohmic losses: $P_{loss} = \frac{1}{2}\iiint_V \sigma(\mathbf{r}, \omega_{em}) \mid \mathbf{E}(\mathbf{r}, \omega_{em}) \mid^2 d^3\mathbf{r}$, where $\mathbf{E}(\mathbf{r}, \omega_{em})$ is the local electric field excited by $\mathbf{p}_{em}$, σ is the electrical conductivity proportional to the imaginary part of the dielectric permittivity: $\sigma(\mathbf{r}, \omega) = \varepsilon_0\varepsilon''(\mathbf{r}, \omega)\omega$, and the integration is over the whole metasurface.

The next factor $\eta_{\text{ext}}(\mathbf{r}_{em}, \omega_{em})$ is the extraction efficiency, indicating the probability that the emitted photon can escape the metasurface [44, 123]. We can estimate the extraction efficiency $\eta_{\text{ext}}(\mathbf{r}, \omega_{em})$ as the ratio between the power radiated to free-space P^{out}_{rad} and the total power radiated by the emitter: $\eta_{\text{ext}}(\mathbf{r}_{em}, \omega_{em}) = P^{out}_{rad}/P_{rad}$. The total power radiated in free-space is calculated by integrating the flux of the Poynting vector $\mathbf{S}(\mathbf{r}, \omega_{em})$ through two planes parallel to the metasurface plane and positioned above (Σ_1) and below (Σ_2) it:

$$P^{out}_{rad} = \iint_{\Sigma_{1,2}} \mathbf{S}(\mathbf{r}, \omega_{em}) \cdot d\mathbf{A}. \tag{2.60}$$

The remaining part of the P_{rad} is captured by dark electromagnetic modes, such as guided modes, and cannot couple to free-space.

The power radiated to free-spaced will be distributed within the full solid angle. In a typical experiment, however, only the emission collected by optics with a limited numerical aperture (NA) contributes to the measured PL signal. We can define the collection efficiency as the ratio between the power harvested by the collection optics (CO) and the total power radiated in free-space P^{out}_{rad}:

$$\eta_{coll} = \frac{1}{P^{out}_{rad}} \iint_{CO} P(\theta, \phi) \sin\theta d\phi d\theta, \tag{2.61}$$

where $P(\theta, \phi)$ is the angular power density radiated in free-space along the direction defined by

the polar angle θ and azimuthal angle ϕ. Note, that $P(\theta, \phi)$ is power per steradian, as opposed to the time-averaged Poynting vector $\mathbf{S}(\mathbf{r}, \omega_{em}) = \frac{1}{2}\mathfrak{Re}\{\mathbf{E}(\mathbf{r}, \omega_{em}) \times \mathbf{H}^*(\mathbf{r}, \omega_{em})\}$ that quantifies directional flux (power per square meter) [45]. The power per steradian emitted in the far-field is calculated as:

$$P(\theta, \phi) = \lim_{r/\lambda \to \infty} r^2 \frac{\mathbf{r}}{r} \cdot \mathbf{S}(\mathbf{r}, \omega_{em}), \tag{2.62}$$

where $\mathbf{r} = (r \sin\theta \cos\phi, r \sin\theta \sin\phi, r \cos\theta)$ and $\lambda = 2\pi c/\omega_{em}$. A properly designed metasurface is capable of redirecting light to improve the collection efficiency.

In common light-emitting metasurface architectures, ensembles of emitters are distributed over the whole metasurface and are arbitrarily oriented. In the *weak* coupling regime, the behavior of each emitter can be considered independently, and their PL adds incoherently to the total metasurface PL. The factorization of the total PL is generally invalid, since each contributing factor in Equation (2.58) is strongly depending on the exact position and orientation of a particular emitter.

Chapter 3

Numerical simulations

3.1 Emission calculations

This section deals with numerical simulations methods focusing on predicting the emission properties of emitters, coupled to a metasurface. In the previous Section 2.4.2, we discussed how metasurfaces can tailor the properties of emitters coupled to them. An obvious way to simulate these effects is to excite the metasurface with a point dipole source [121]. In case of single particle nanoantennas [93, 124], such simulations allow for accurate calculations of the decay rate enhancement, directionality and extraction efficiency (see Equation (2.58)). Indeed, the total dissipated power, as well as its constituents can be calculated by simply integrating the local dissipation and Poynting vector flow. The angular power density of the far-field emission $P(\theta, \phi)$ is the Poynting vector evaluated on a far-field spherical surface in the limit of infinite radius. The excitation enhancement requires separate calculations with the excitation corresponding to the experimental conditions [13].

The metasurfaces are periodic arrangements of nanoresonators and infinitely extended compared to the wavelength of the emission. Transmission or reflection calculations (see Section 3.3) imply a plane wave excitation and make use of periodic boundary conditions limiting the computational domain to a single unit cell. However, if we follow the same approach and perform the simulations for a single unit cell incorporating a point dipole source using Floquet periodic boundary conditions with a wavevector $\mathbf{k}_F$, we will effectively create an array of coherent point dipole sources with a phase relation $e^{i\mathbf{k}_F \cdot \mathbf{r}}$. Clearly, the single point source excitation breaks the periodicity and requires a different method. An interesting example is the array scanning method [45] allows for a reconstruction of the emission response of a single dipole source in a periodic metasurface by combining the response for the arrays of coherent point dipole sources with varied phase relation via sweeping the Floquet wavevector over the whole Brillouin zone. Below we describe two alternative methods for emission simulations, which were adapted and applied by the author during his research.

3.1.1 Finite array simulations

The idea of this method is to construct a finite array of several unit cells within a computational domain with PML (perfectly matched layer) boundary conditions [45, 83]. Since the finite size of the array can affect the wavelength and Q-factor of the resonances in the metasurface [125, 126], this method offers a trade-off between the accuracy and the computational resource demand, in particular, the time and computer memory required by the computational process.

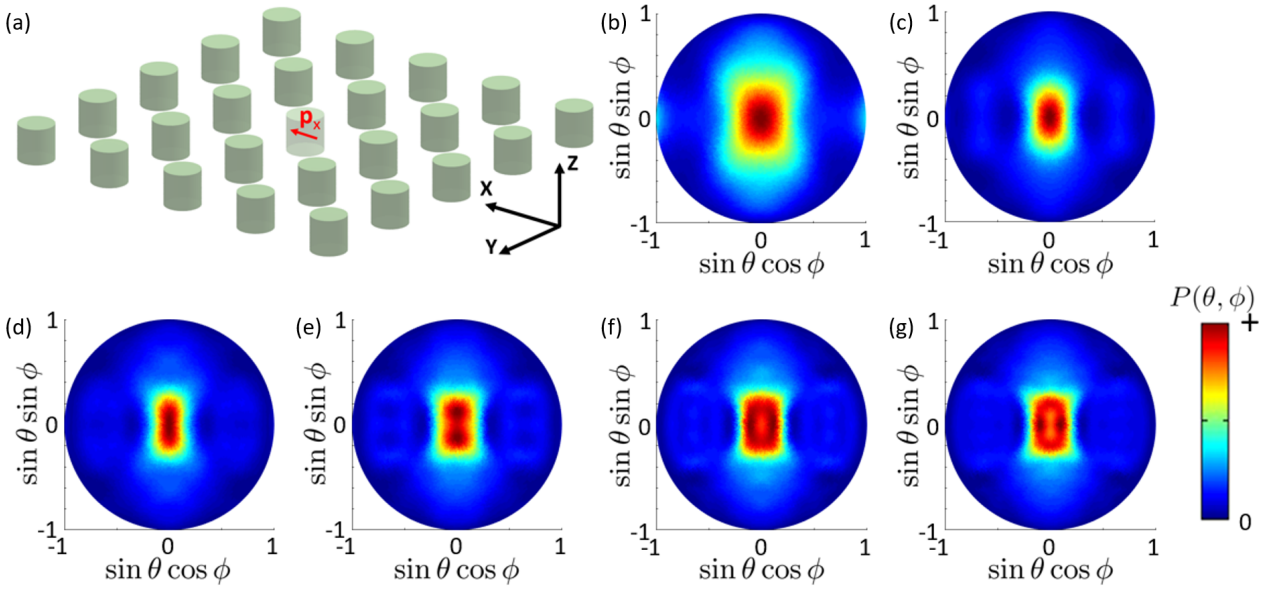

Figure 3.1: (a) An example of finite array consisting of 5×5 dielectric nanocylinders and excited by the x-polarized point electric dipole $\mathbf{p}_x$ placed in the center of the array. Far-field emission pattern $P(\theta, \phi)$ in the upper semi-sphere ($z > 0$) of a finite array consisting of (b) 3×3 unit cells, (c) 5×5 unit cells, (d) 7×7 unit cells, (e) 9×9 unit cells, (f) 11×11 unit cells, (g) 13×13 unit cells. Reprinted with permission from [45]. Copyright (2019) Walter de Gruyter and Company.

We tested how the size of the finite array influences the far-field emission pattern using finite element package COMSOL, which includes electric and magnetic point dipole sources. Alternatively, arbitrary point sources can be implemented by imposing external currents on specifically designed geometrical objects. Due to the limitations of the computational domain, the far-field emission pattern calculations require a near- to far-field transformation. In particular, COMSOL implements the approach based on the Stratton-Chu formula. This transformation requires a closed surface including all scattering objects and sources, and a homogeneous medium outside the surface.

The considered array is shown in Figure 3.1 (a) and consists of periodically arranged high-index dielectric nanocylinders surrounded by vacuum. The lattice constant is 1000 nm. The driving source is an x-polarized point electric dipole placed in the center of the array. The nanocylinders are designed to exhibit ED resonance at the oscillation frequency of the source. Figure 3.1 (b-g) show the simulated angle-resolved far-field emission into the upper semi-sphere ($z > 0$). Note that unlike the Chapter 2, where we showed the far-field patterns in 3D, here we present the angle-resolved far-field emission intensity $P(\theta, \phi)$ as a 2D color plot in $(\sin\theta\cos\phi, \sin\theta\sin\phi)$ coordinate system. The color from blue to red indicates the emission

intensity value. The smallest 3×3 array exhibits a broad emission pattern in Figure 3.1 (b), which becomes narrower with increasing number of unit cells. For finite arrays consisting of 9×9 and more unit cells (Figure 3.1 (e-g)), the emission patterns show only slight changes. Interestingly, the overall shape of the emission pattern (narrow lobe in the forward direction) can be explained by the hybridization of the ED and lattice resonances (see Figure 2.11).

3.1.2 Calculations based on the reciprocity principle

In our work we need an efficient approach for simulating angular emission from metasurfaces. As discussed, the finite array simulations are resource-demanding, require homogeneous background, and only provide limited accuracy. Here, we describe a method for calculating the angular emission from metasurfaces, which is based on the reciprocity principle (see Figure 3.2), allowing us to overcome these limitations.

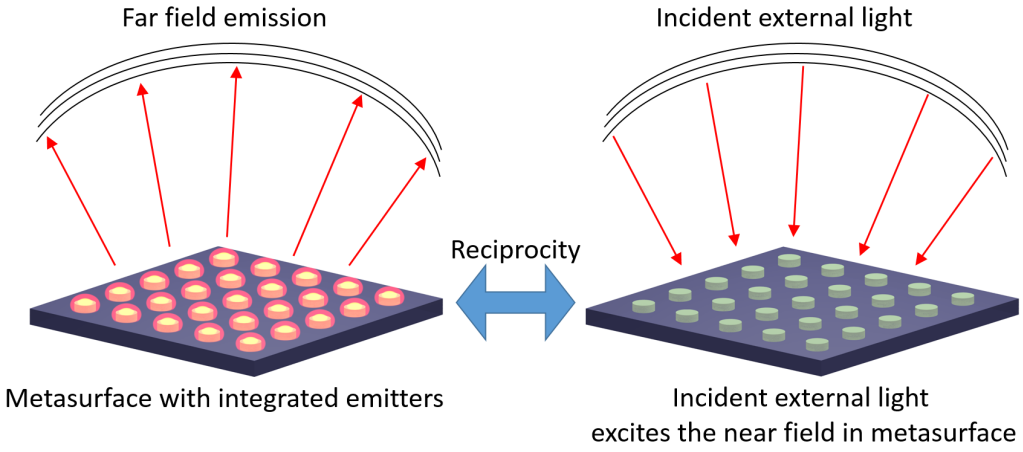

Figure 3.2: The concept of the calculations based on the reciprocity principle. The far-field emission from the metasurface with coupled incoherent emitters is reciprocal to the intensity of the near-field excited in the metasurface by the incident external light averaged over the positions of the emitters. Reprinted with permission from [45]. Copyright (2019) Walter de Gruyter and Company.

The monochromatic electromagnetic radiation generated by an external current source $\mathbf{J}_1$ in an arbitrarily medium is described by the following set of equations [2]:

$$\nabla \times \mathbf{E}_1 = i\omega \mathbf{B}_1 \tag{3.1}$$

$$\nabla \times \mathbf{H}_1 = -i\omega \mathbf{D}_1 + \mathbf{J}_1 \tag{3.2}$$

We consider another source $\mathbf{J}_2$ oscillating at the same frequency in the same medium. The fields produced by each of these sources independently are labeled by indices 1 or 2. In the following, we restrict the discussion to media that satisfy the linear relations $D_i = \varepsilon_0 \varepsilon_{ik} E_k$ and $B_i = \mu_0 \mu_{ik} H_k$ with symmetric tensors $\varepsilon_{ik} = \varepsilon_{ki}$ and $\mu_{ik} = \mu_{ki}$.

Next, we multiply Equation (3.1) by $\mathbf{H}_2$ and Equation (3.2) by $\mathbf{E}_2$, and the corresponding equations for the fields $\mathbf{E}_2$ and $\mathbf{H}_2$ by $-\mathbf{H}_1$ and $-\mathbf{E}_1$, respectively. Then we sum up all four equations:

$$\begin{aligned}&(\mathbf{H}_2 \cdot (\nabla \times \mathbf{E}_1) - \mathbf{E}_1 \cdot (\nabla \times \mathbf{H}_2)) + (\mathbf{E}_2 \cdot (\nabla \times \mathbf{H}_1) - \mathbf{H}_1 \cdot (\nabla \times \mathbf{E}_2)) \\ &= i\omega(\mathbf{B}_1 \cdot \mathbf{H}_2 - \mathbf{H}_1 \cdot \mathbf{B}_2) + i\omega(\mathbf{E}_1 \cdot \mathbf{D}_2 - \mathbf{D}_1 \cdot \mathbf{E}_2) + (\mathbf{J}_1 \cdot \mathbf{E}_2 - \mathbf{J}_2 \cdot \mathbf{E}_1)\end{aligned} \tag{3.3}$$

We notice that $\mathbf{B}_1 \cdot \mathbf{H}_2 = \mu_0 \mu_{ik} H_{1k} H_{2i} = \mathbf{H}_1 \cdot \mathbf{B}_2$ and $\mathbf{E}_1 \cdot \mathbf{D}_2 = \mathbf{D}_1 \cdot \mathbf{E}_2$. As the result, Equation (3.3) can be simplified to:

$$\nabla \cdot (\mathbf{E}_1 \times \mathbf{H}_2 - \mathbf{E}_2 \times \mathbf{H}_1) = (\mathbf{J}_1 \cdot \mathbf{E}_2 - \mathbf{J}_2 \cdot \mathbf{E}_1) \tag{3.4}$$

Next we integrate the Equation (3.4) over the whole space. Using the Ostrogradsky's theorem, the integral in the left part becomes the integral over an infinitely distant surface and vanishes. Finally, we arrive at the reciprocity principle:

$$\iiint \mathbf{J}_1(\mathbf{r}) \cdot \mathbf{E}_2(\mathbf{r}) d^3\mathbf{r} = \iiint \mathbf{J}_2(\mathbf{r}) \cdot \mathbf{E}_1(\mathbf{r}) d^3\mathbf{r} \tag{3.5}$$

where $\mathbf{E}_1(\mathbf{r})$ and $\mathbf{E}_2(\mathbf{r})$ are the electric fields produced by $\mathbf{J}_1(\mathbf{r})$ and $\mathbf{J}_2(\mathbf{r})$, correspondingly. If we consider two point electric dipole sources: $\mathbf{J}_m = -i\omega \mathbf{p}_m \delta(\mathbf{r} - \mathbf{r}_m)$, where $m = 1, 2$, Equation (3.5) will simplify into the common expression:

$$\mathbf{p}_2 \cdot \mathbf{E}_1(\mathbf{r}_2) = \mathbf{p}_1 \cdot \mathbf{E}_2(\mathbf{r}_1) \tag{3.6}$$

A formulation of the reciprocity principle for the two cases of magnetic dipole and electric quadrupole sources can be found in Landau et al. [2].

We place the first dipole $\mathbf{p}_1$ on the periodic metasurface, and locate the second dipole $\mathbf{p}_2$ far away along the direction (θ, ϕ). In this scenario, the electric $\mathbf{E}_1(\mathbf{r}_2)$ is the far-field emitted by the first dipole in the direction (θ, ϕ). On the contrary, $\mathbf{E}_2(\mathbf{r}_1)$ represents the electric field at the metasurface excited by a plane wave produced by the second dipole and incident along the same direction (θ, ϕ). The polarization of the incident plane wave is parallel to the orientation of the second dipole $\mathbf{p}_2$. Therefore, we are able to calculate the far-field emission from a point dipole source placed on the metasurface, by calculating the near-field excited by the incident plane wave at the position of the dipole. The simulations of the plane wave exciting the periodic metasurface can be performed for the unit cell with periodic boundary conditions.

Altogether, the far-field power $P(\theta, \phi; \mathbf{r}_1)$ emitted along the direction (θ, ϕ) by a point electric dipole $\mathbf{p}_1$ placed at $\mathbf{r}_1$ on the metasurface is calculated as [13, 127]:

$$P(\theta, \phi; \mathbf{r}_1) \propto \frac{\sqrt{\varepsilon_2}}{\mid \mathbf{p}_2 \mid^2} \int_0^{2\pi} \int_0^{\pi} \Big[\sum_{TE,TM} \mid \mathbf{E}_2(\mathbf{r}_1) \cdot \mathbf{p}_1 \mid^2 \Big] \sin\theta_p d\theta_p d\phi_p \tag{3.7}$$

where TE, TM denotes TE and TM polarisation of the plane wave incident along the direction (θ, ϕ), $\mathbf{E}_2(\mathbf{r}_1)$ is the exciting near-field and ε_2 is the dielectric permittivity of the medium surrounding $\mathbf{p}_2$. The integration is performed to average over all possible orientations of $\mathbf{p}_1 = (p_1 \sin\theta_p \cos\phi_p, p_1 \sin\theta_p \sin\phi_p, p_1 \cos\theta_p)$. For a randomly fluctuating point dipole source, which on average is isotropically oriented, the integration in Equation (3.7) is reduced to $p_1^2 \mid \mathbf{E}_2 \mid^2$.

Finally, we can add up the emission contributions from all emitters located in the metasur-

face via the following integration:

$$P(\theta,\phi) = \iiint_V P(\theta,\phi;\mathbf{r}_1)d^3\mathbf{r}_1 \tag{3.8}$$

where V is the volume within the unit cell that contains the emitters. Note that we assume that all emitters are excited with the same efficiency. Otherwise, one needs to introduce appropriate weight functions for the differently excited emitter regions. We also do not take into account the QY of the emitters.

We applied the reciprocity principle to calculate the emission pattern $P(\theta,\phi)$ from the periodic metasurface shown in Figure 3.1 (a). We simulated a unit cell with periodic boundary conditions and excited by a plane wave (see Figure 3.3 (a)). According to the Equation (3.7), the far-field power $P(\theta,\phi)$ is proportional to $\sum_{TE,TM} E_x^2$, where E_x is the $x-$component of the electric field excited by a TE or TM polarized plane wave incident along the direction (θ,ϕ) and evaluated in the center of the cylinder (where the hypothetical point dipole source is located). The results are shown in Figure 3.3 (a) and are in good agreement with calculations based on the finite array method (see Figure 3.1 (a-g)).

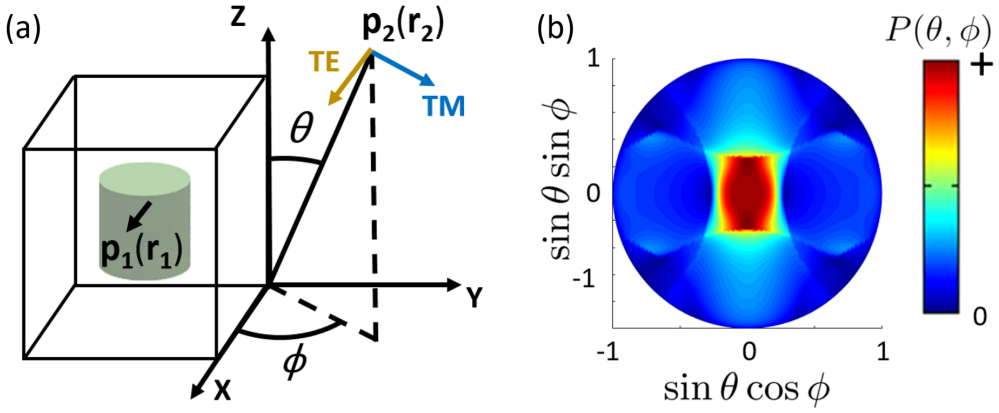

Figure 3.3: (a) Sketch of the unit cell with two hypothetical electric point dipole sources $\mathbf{p}_1$ and $\mathbf{p}_2$. (b) Calculated emission pattern $P(\theta,\phi)$ using the reciprocity principle. Reprinted with permission from [45]. Copyright (2019) Walter de Gruyter and Company.

Note that the reciprocity principle doesn't take into account the dark modes of the metasurfaces, since the incident plane wave cannot couple to such modes. For this reason, the total dissipated power, as well as quenching, cannot be estimated using this approach.

3.2 Multipole decomposition

The electric field scattered by a single nanoparticle in homogeneous medium can be decomposed into spherical harmonics in accordance with the Equation (2.36). For the scattered field $\mathbf{E}_s$, which has been numerically calculated on a spherical surface around the particle, the multipole coefficients are:

$$a_{lm} = \frac{\int_0^{2\pi}\int_0^{\pi}(\mathbf{N}_{lm}^{(3)})^* \cdot \mathbf{E}_s \sin\theta d\theta d\phi}{E_0 \int_0^{2\pi}\int_0^{\pi}|\mathbf{N}_{lm}^{(3)}|^2 \sin\theta d\theta d\phi} \tag{3.9}$$

$$b_{lm} = \frac{\int_0^{2\pi}\int_0^{\pi}(\mathbf{M}_{lm}^{(3)})^* \cdot \mathbf{E}_s \sin\theta d\theta d\phi}{E_0 \int_0^{2\pi}\int_0^{\pi}|\mathbf{M}_{lm}^{(3)}|^2 \sin\theta d\theta d\phi} \tag{3.10}$$

The multipole decomposition of the scattered field in case of a spherical particle was demonstrated in the Figure 2.2. The spectrum of the scattering contribution from a particular mode is well-correlated with the spectrum of the Mie-coefficient corresponding to the same mode excited inside the particle (see Figure 2.3). In this thesis we utilize the multipole decomposition to identify the Mie-modes responsible for certain far-field features of the investigated metasurface.

Classically, the multipole decomposition theory is formulated only for the case of an individual scatterer [1]. However, Grahn et al. [128] introduced a multipole theory which is also suitable for analysis of nanoresonators in arrays such as metasurfaces. To this end, they define the scattering current density:

$$\mathbf{J}_s(\mathbf{r}) = -i\omega\varepsilon_0[\varepsilon(\mathbf{r}) - \varepsilon_d]\mathbf{E}(\mathbf{r}) \tag{3.11}$$

where $\mathbf{E}(\mathbf{r})$ is the local electric field excited in the array, ε_d is the permittivity of the embedding dielectric medium and $\varepsilon(\mathbf{r})$ is the permittivity at any coordinate $\mathbf{r}$. A distinct scattering source current $\mathbf{J}_{s,j}$ is defined in each particle j, so that $\mathbf{J}_s = \sum_j \mathbf{J}_{s,j}$. Then Maxwell's equations with external current $\mathbf{J}_{s,j}$ can be solved for the electric field $\mathbf{E}_{s,j}$ scattered by each particle. The corresponding multipole coefficients are found by the substitution of this solution into Equations (3.9) and (3.10):

$$a_{lm} = \frac{(-i)^{l-1}k^2\eta O_{lm}}{E_0[\pi(2l+1)]^{1/2}} \int e^{-im\phi}\{[\Psi_l(kr) + \Psi_l''(kr)]P_l^m(\cos\theta)\hat{\mathbf{r}} \cdot \mathbf{J}_{s,j}(\mathbf{r}) + \frac{\Psi_l'(kr)}{kr}[\tau_{lm}(\theta)\hat{\boldsymbol{\theta}} \cdot \mathbf{J}_{s,j}(\mathbf{r}) - i\pi_{lm}(\theta)\hat{\boldsymbol{\phi}} \cdot \mathbf{J}_{s,j}(\mathbf{r})]\}d^3r \tag{3.12}$$

$$b_{lm} = \frac{(-i)^{l-1}k^2\eta O_{lm}}{E_0[\pi(2l+1)]^{1/2}} \int e^{-im\phi} j_l(kr)[i\pi_{lm}(\theta)\hat{\boldsymbol{\theta}} \cdot \mathbf{J}_{s,j}(\mathbf{r}) + \tau_{lm}(\theta)\hat{\boldsymbol{\phi}} \cdot \mathbf{J}_{s,j}(\mathbf{r})]d^3r \tag{3.13}$$

where $\hat{\mathbf{r}}$,$\hat{\boldsymbol{\theta}}$ and $\hat{\boldsymbol{\phi}}$ are the unit vectors in spherical coordinates and $\eta = \sqrt{\mu_0/\varepsilon_d}$ is the impedance. The functions $\Psi_l(kr)$, O_{lm}, $\tau_{lm}(\theta)$ and π_{lm} are defined as follows:

$$\Psi_l(kr) = krj_l(kr) \tag{3.14}$$

$$O_{lm} = \frac{1}{[l(l+1)]^{1/2}} \left[\frac{2l+1}{4\pi}\frac{(l-m)!}{(l+m)!}\right]^{1/2} \tag{3.15}$$

$$\tau_{lm}(\theta) = \frac{d}{d\theta}P_l^m(\cos\theta) \tag{3.16}$$

$$\pi_{lm}(\theta) = \frac{m}{\sin\theta}P_l^m(\cos\theta) \tag{3.17}$$

The integration in Equations (3.12) and (3.13) is performed over the whole space. However, the scattering current density $\mathbf{J}_{s,j}(\mathbf{r})$ and so the integrals are equal to zero everywhere outside the nanoresonators. Thereby, the calculations of multipole coefficients only require the knowledge of the total electric field inside the nanoresonators.

3.3 COMSOL implementation for emission calculations

We used the commercially available package COMSOL Multiphysics for most of the simulations performed in the current study. COMSOL utilizes the finite element method to solve partial differential equations, in particular the wave equation 2.11.

First, we discuss a COMSOL model, which utilizes point dipole excitation. The sketch of the model is shown in Figure 3.4 (a). In the example, we simulate a single nanocylinder (grey) driven by an x-polarized point electric dipole located in the center of the nanocylinder (red arrow). The nanocylinder is surrounded by an optical medium (blue) and the green domain is the PML which absorbs the outgoing light.

We exploit the electromagnetic symmetry of the model configuration to reduce the computational domain size. The $z-y$ plane is the mirror symmetry plane for the magnetic field. This means that the magnetic field is zero in the normal direction to the boundary and the magnetic field must be tangential to this boundary. As a consequence, the boundary along the $z-y$ plane can be modelled as a perfect electric conductor (PEC) boundary condition. Similarly, the $z-x$ plane is the mirror symmetry plane for the electric field and can be represented by a perfect magnetic conductor (PMC) boundary condition.

Hereby, the simulation domain can be reduced to a quarter of its original size. Figure 3.4 (b) illustrates the resulting numerical model when exploiting these symmetries. The nanocylinder (grey) is placed on substrate (yellow) and embedded into a dielectric medium (blue). The refractive index of each PML (green and pink domains) coincides with the refractive index of the adjusted medium. The $z-x$ and $z-y$ faces are assigned to the PMC and PEC boundary conditions, respectively.

The point electric dipole can be modelled as a tiny ($\ll \lambda$) sphere with induced external current density, or as an actual point electric dipole source implemented in COMSOL. However, in the latter case, COMSOL requires the point electric dipole to be slightly displaced from PEC and PMC. This displacement doesn't break the symmetry and represents 4 identical closely positioned in-phase dipoles driving the nanocylinder. Note that these 4 dipoles effectively act as a single point dipole with 4 times increased dipole moment.

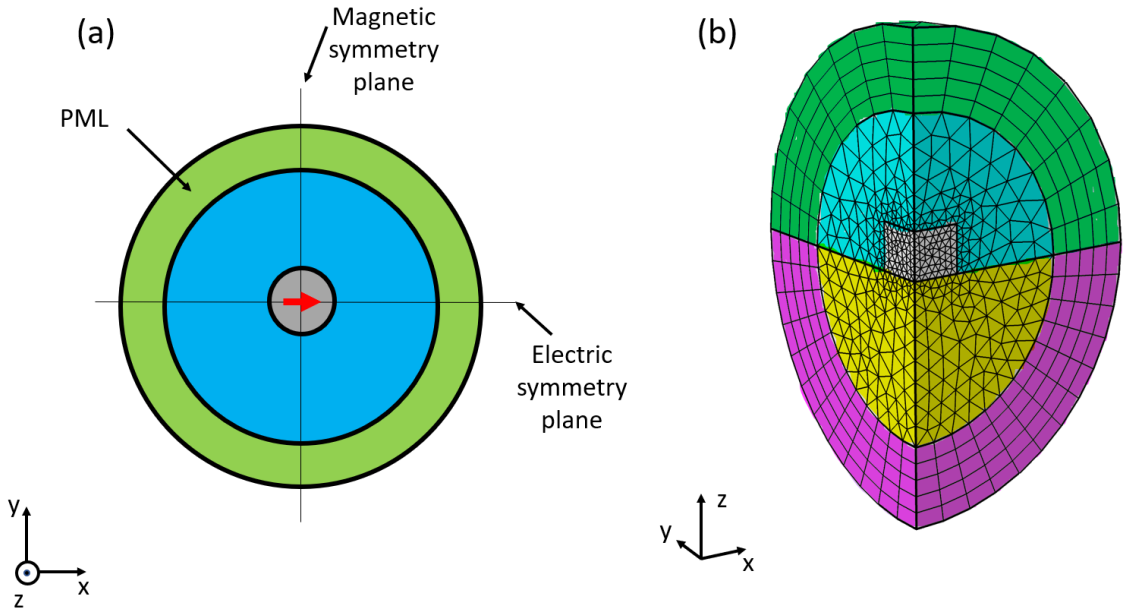

Figure 3.4: (a) A sketch of the simulation domain considered in the example. The nanocylinder (grey) is placed in an optical medium (blue) and is excited by an x-polarized point electric dipole. (b) The sketch of the numerical model after exploiting the symmetries: a single dielectric nanocylinder (grey), excited by an electric point dipole (not shown) located above the center of the cylinder. The green and purple domains are PMLs. The blue domain is the embedding medium and the yellow domain is the substrate. The boundary conditions on the $x-z$ and $y-z$ faces are either PEC or PMC, depending on the point dipole orientation. The domains composing the model were meshed.

For linear spectrum and emission pattern simulations, as well as for multipole decomposition calculations a different numerical model was used. Figure 3.5 depicts the unit cell of a periodic metasurface consisting of dielectric nanocylinders. The dielectric nanocylinder (grey) is located on a substrate (yellow) and embedded in a dielectric medium (blue).

An important step of creating a COMSOL model is to set up the boundary conditions. The top $x-y$ face Port 1 is assigned as a periodic port and launches a plane wave incident on the metasurface at polar angle θ and azimuthal angle ϕ. This port also absorbs the reflected light (including all existing diffraction orders). The bottom $x-y$ face Port 2 is another periodic port that absorbs the transmitted light. Periodic ports automatically calculate the reflection and transmission among with other S-parameters by decomposing the out-coming light into the diffraction orders. In contrast, the $x-z$ and $y-z$ faces implement the Floquet periodic boundaries. The phase shift on the opposite boundaries is defined by the corresponding projection of the wavevector of the incident plane wave onto the metasurface plane.

The width and depth of the unit cell match with the period of the metasurface P. To ensure no near-fields are reaching the ports, the height of the unit cell is chosen in the way that the distance between the scatterer (nanocylinder) and any of the ports exceeds $\lambda = \lambda_0/n$, where λ_0 is a free-space wavelength and n the refractive index of a medium. The maximum mesh element size was set up to $\lambda/5$.

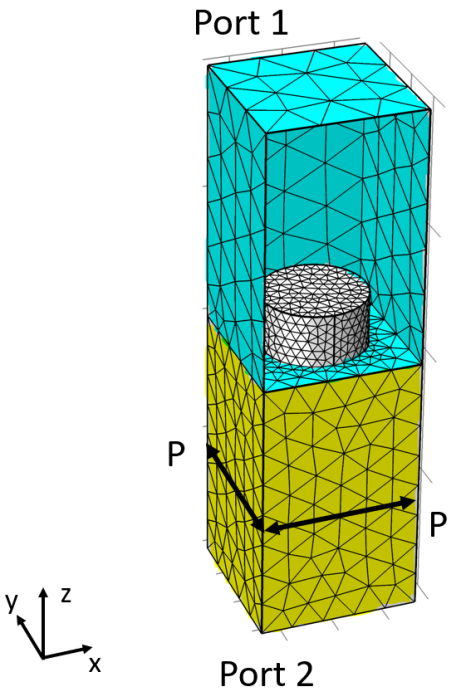

Figure 3.5: The unit cell of a periodic metasurface consisting of dielectric nanocylinders (grey). The embedding medium is shown in blue, the substrate is shown in yellow. Port 1 is used for excitation. Both Port 1 and Port 2 absorb all the diffraction orders. Periodic boundary conditions were applied to the sides of the domain. The domains composing the model were meshed.

Alternatively, we utilized the Fourier Modal Method [129, 130] for angular-resolved absorption calculations which, as described in Section 3.1.2, allow for the reconstruction of the angular emission patterns via the reciprocity principle. In this method, the computational domain is divided into layers that are uniform along the z-axis. The periodic permittivity distribution in each of these layers is represented in the form of a Fourier series, leading to an eigenvalue equation. Once the electromagnetic fields in each layer are obtained by solving this equation numerically, the overall problem is solved by matching the electromagnetic boundary conditions at each of the interfaces between the layers. The increase in the number of spatial harmonics used in the decomposition into a Fourier series improves the accuracy but complicates the calculations. Therefore, the convergence tests are required before proceeding to the simulations of a new system. In our models for dielectric metasurfaces, a satisfactory accuracy (within 2 nm of resonant wavelength) was typically reached by 12 spatial harmonics.

The main motivation to use FMM instead of COMSOL, lies in the fact that the scripts developed by a member of our group Matthias Zilk can run on the freeware Octave. Therefore there are no limitations in the number of licenses and the parametric sweep can be effectively distributed over multiple parallel computations. This is crucial for the angular emission pattern calculations as they require many independent calculations for different angles of incidence and polarization of the excitation plane wave.

Chapter 4

Experimental techniques

4.1 Fabrication of dielectric nanostructures

In this manuscript we investigate two different types of metasurfaces. The first type is arrays of nanocylinders made of hydrogenated amorphous silicon (a-Si:H) on low-index substrate [131]. The fabrication of such metasurfaces was done at Australian National University by Katie E. Chong in accordance with the following steps: First, a thin film of a-Si:H was deposited on standard microscope coverslips using plasma-enhanced chemical vapor deposition at a temperature of 250 $°C$. In Figure 4.1 we depict the refractive index of a-Si:H measured from the thin film using ellipsometry. Then, the negative-tone electron-beam resist maN-2403 was spin-coated on the substrates, and certain areas of it were exposed to electron irradiation. The silicon nanocylinders were then formed by inductively coupled plasma (ICP) etching of the silicon thin film, where the exposed electron-beam resist is used as an etch mask. The etch gases were SF_6 (1.8 sccm) and CHF_3 (50 sccm). The etching was performed at 20$°C$ with 10 mTorr at 500 W induction power and 15 W bias power. Finally, the residual resist and organic solvent residue were removed from the sample using an oxygen plasma.

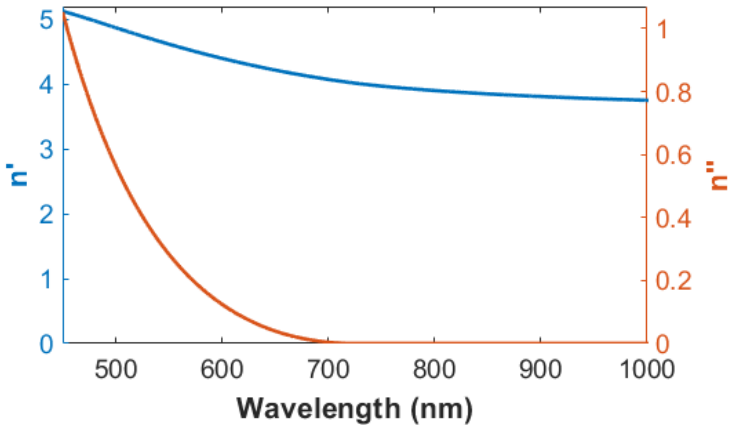

Figure 4.1: Complex refractive index $n = n' + in''$ of the a-Si:H films obtained by ellipsometry measurements. Courtesy of Katie E. Chong.

The second type of metasurfaces studied in this thesis are arrays of GaAs nanocylinders incorporating one or more layers of InAs QDs [111]. The fabrication was done at the Sandia

National Laboratories by Sheng Liu. First, the layered wafer was prepared via molecular beam epitaxy (MBE) in a VG V80 reactor on a (001) GaAs wafer. Prior to growth, the native oxide on the GaAs substrate was thermally desorbed at 630°C for 20 min. Next, a 200 nm thick smoothing layer of GaAs and a 500 nm thick $Al_{0.85}Ga_{0.15}As$ layer were consequently grown at 580°C. The substrate temperature was then brought down to 475°C for the growth of the active medium. The QDs were formed by growing 2.5 monolayers (ML) of InAs on a 1 nm $In_{0.15}Ga_{0.85}As$ bottom quantum well and are around 30 nm wide by 5 nm high and have an areal density of around 2×1010 cm^{-2}. They were later capped by a 4 nm thick $In_{0.15}Ga_{0.85}As$ top quantum well followed by a 1.5 nm cold GaAs cap. The substrate temperature was then brought back up to 580°C where the rest of the GaAs cap is grown. This process was repeated for each stack of QDs in a quantum well. The In and Ga growth rates were kept constant at 0.05 and 0.3 ML/sec, and a constant As:Ga ratio of 13 was maintained. The internal QY of QDs is around 0.53.

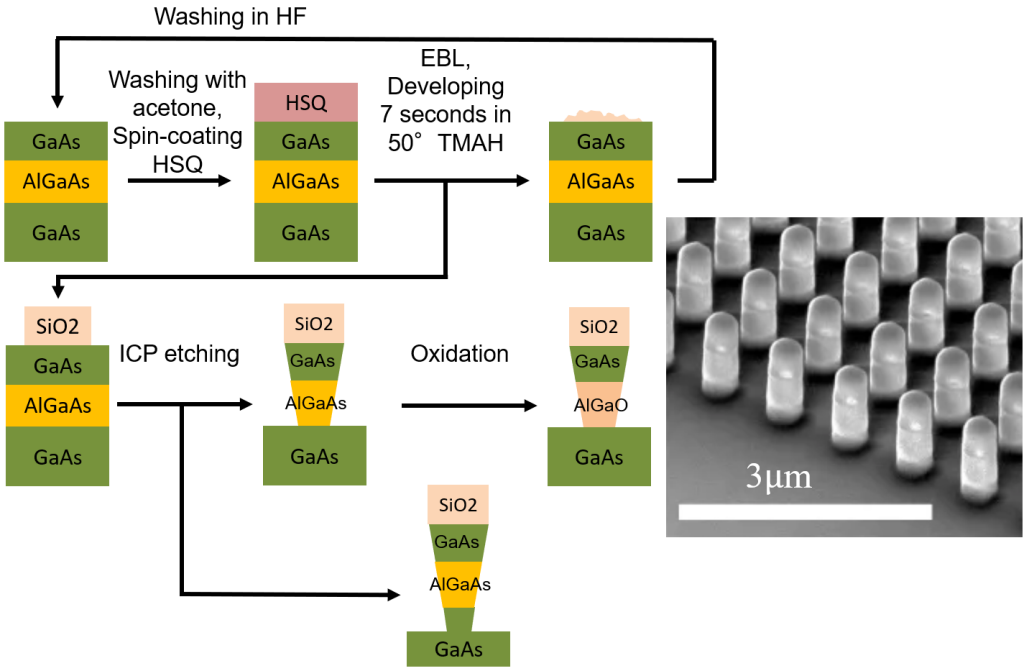

Figure 4.2: Fabrication process and a typical SEM of metasurfaces composed of GaAs nanocylinders incorporating layers of InAs QDs. The process was developed by Sheng Liu.

To fabricate the GaAs metasurfaces we followed the steps illustrated in Figure 4.2. First, the grown wafers were spin-coated with hexamethyldisilazane (HMDS) to provide the adhesion with the negative-tone hydrogen silsesquioxane (HSQ) resist spin-coated next. We prepared a gds mask file and calculated the proximity effect correction for a particular wafer structure. The original gds mask was copied and translated 4 times over the sample, each copy had different assigned initial values of the dose varying from 0.8 to 1.2 of the target dose. After the electron-beam lithography exposure, we developed the resist in 20% TMAH at 50°C for 7 seconds. The result of the electron beam exposure, during which the HSQ resist is transformed into the mixture if different silicon oxides, was then checked for quality in optical microscopy and if the quality of the mask was unsatisfactory, we dissolved it in HF and the process was started over. If the quality was good, we performed ICP etching of the layered wafer structure as a

next step. Since it was not feasible to introduce an etch stop layer below the AlGaAs layer due to problematic adhesion, the ICP etching duration could not be well-controlled and sometimes resulted in undesirable penetration through the bottom GaAs wafer. The etched structures were evaluated using scanning electron microscopy and then selectively wet oxidized. The final step turned the $Al_{0.85}Ga_{0.15}As$ layer into an oxide (AlGaO). Altogether, the fabrication process resulted in high-index GaAs nanocylinders situated on low-index AlGaO pedestal and covered by low-index silicon oxide cap.

4.2 Linear spectroscopy

Mie-resonances of a metasurface affect the scattering and can result in zero transmission (or unity reflection) of the incident plane wave at the resonant wavelength. The workhorse tool for characterizing the resonant behavior of the metasurfaces is near-normal incidence linear zero-order reflection/transmission spectroscopy.

For optical characterization of silicon metasurfaces we utilized the transmission spectroscopy setup shown in Figure 4.3. A broadband source, in our case a halogen lamp, forms the excitation beam (yellow). A system of lenses 1-3 and apertures 1-2 constructs the Köhler illumination [132], which provides an even illumination of the sample. In addition, reducing the size of aperture 2 allows one to limit the NA of the beam incident onto the metasurface. The light transmitted by the metasurface is collected by lens 4 and coupled to a fiber attached to a visible spectrometer. The spectrum measured by the spectrometer is normalized to the signal transmitted through the unstructured area of the sample between the metasurfaces.

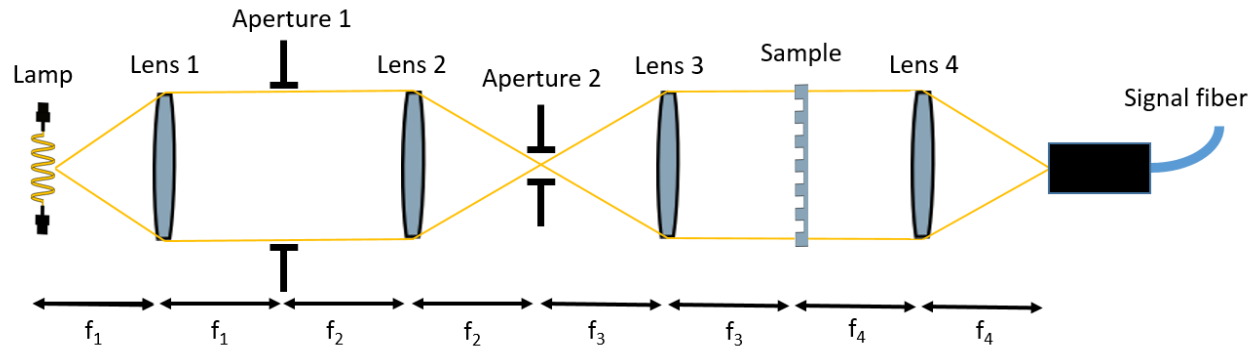

Figure 4.3: Schematic of experimental setup used for near-normal incidence linear zero-order transmission spectroscopy for characterization of the silicon metasurfaces. f_i is a focal distance of i-th lens.

The GaAs nanocylinders metasurfaces transmission measurements could not be performed, since the backside of the GaAs handle wafer is unpolished. Therefore, for these samples, we measure the reflection instead, using a setup shown in Figure 4.4. The emission from a broadband source, in our case a halogen lamp, was coupled to a multimode fiber. The other end of this "illumination fiber" was attached to the setup and a focusing lens was used to collimate the emission. The collimated beam propagated through a system of beamsplitters to a low-NA objective focused on the sample. We used a small aperture at the entrance pupil of the objective to further reduce the NA of the focused beam. The reflected light was collected by the same objective and coupled to the "signal fiber" attached to a NIR spectrometer. As a reference, we used the signal reflected from a gold mirror put replacing the sample.

In both experimental setups for transmittance and reflectance measurements, we were able to achieve about 0.04NA of the beam incident onto the metasurface, corresponding to near-normal incidence and, thus, facilitating comparison of the measured spectra with the calculated ones. The beam spot on the sample had a size of around 100 μm in diameter, which is much bigger than the unit cell size while fitting completely within a metasurface footprint.

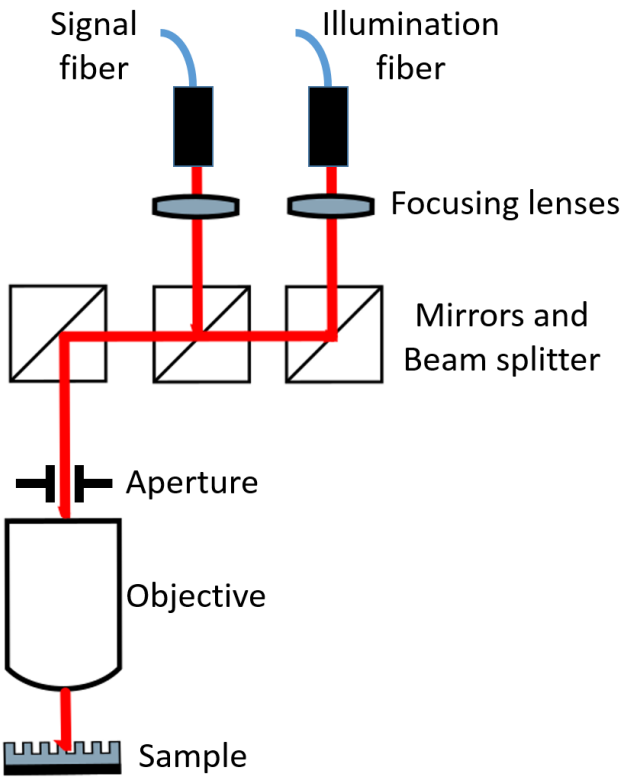

Figure 4.4: Schematic of experimental setup used for near-normal incidence linear zero-order reflectance spectroscopy of the GaAs metasurfaces.

4.3 Back focal plane imaging

BFP imaging is an experimental method that allows for quantitative mapping of angular emission patterns. This technique is based on the property of a lens to create a Fourier transform of the optical field in its front-focal plane (FFP) at the BFP of the lens [133, 134]. A primitive illustration of this principle is shown in Figure 4.5. Three sources are placed in the FFP of a lens. Each source emits 5 light rays in different directions. Each color of the lines is assigned to an angle which a ray makes to the optical axis. The light rays originating from different sources, but propagating along the same directions, converge at the same point at the BFP of the lens.

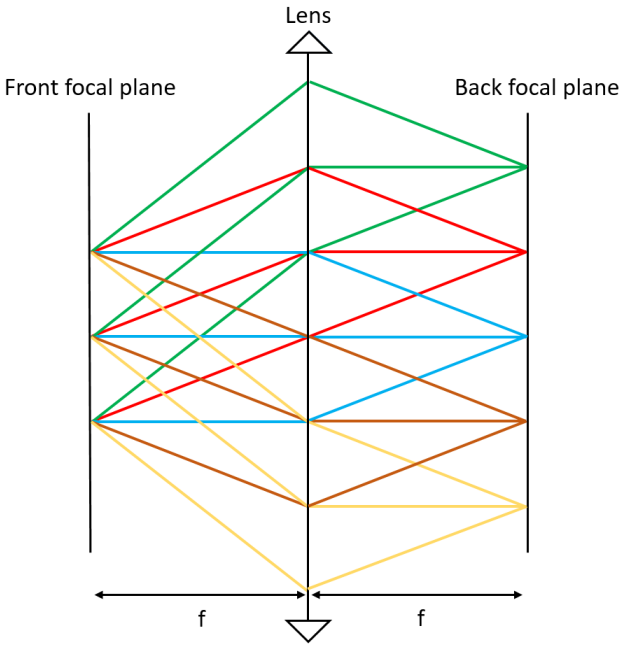

Figure 4.5: Illustration of the BFP imaging principle. The light rays emitted from the FFP along the same direction converge at the same spot in the BFP. f denotes the focal length of the lens.

Generally, the intensity distribution $P(k_x, k_y)$ within the BFP of the objective is related to the angular distribution of the emission $P(\theta, \phi)$ from the sample placed in the FFP as [134, 135]:

$$P(k_x, k_y) = P(\theta, \phi) \cos^{-1} \theta \tag{4.1}$$

$$k_x = (2\pi/\lambda) \sin\theta \cos\phi \tag{4.2}$$

$$k_y = (2\pi/\lambda) \sin\theta \sin\phi \tag{4.3}$$

where λ is the wavelength of the emission and $\cos^{-1}\theta$ is the apodization factor which originating from the fact the energy emitted in an angle increment $d\theta$ is projected onto the area $dk = \cos\theta \mathrm{d}\theta$ in the BFP [134]. The NA of the objective corresponds to the highest angle θ at which the emission can be collected. Therefore, a typical BFP image is a circle with a radius of NA$\cdot k_0$.

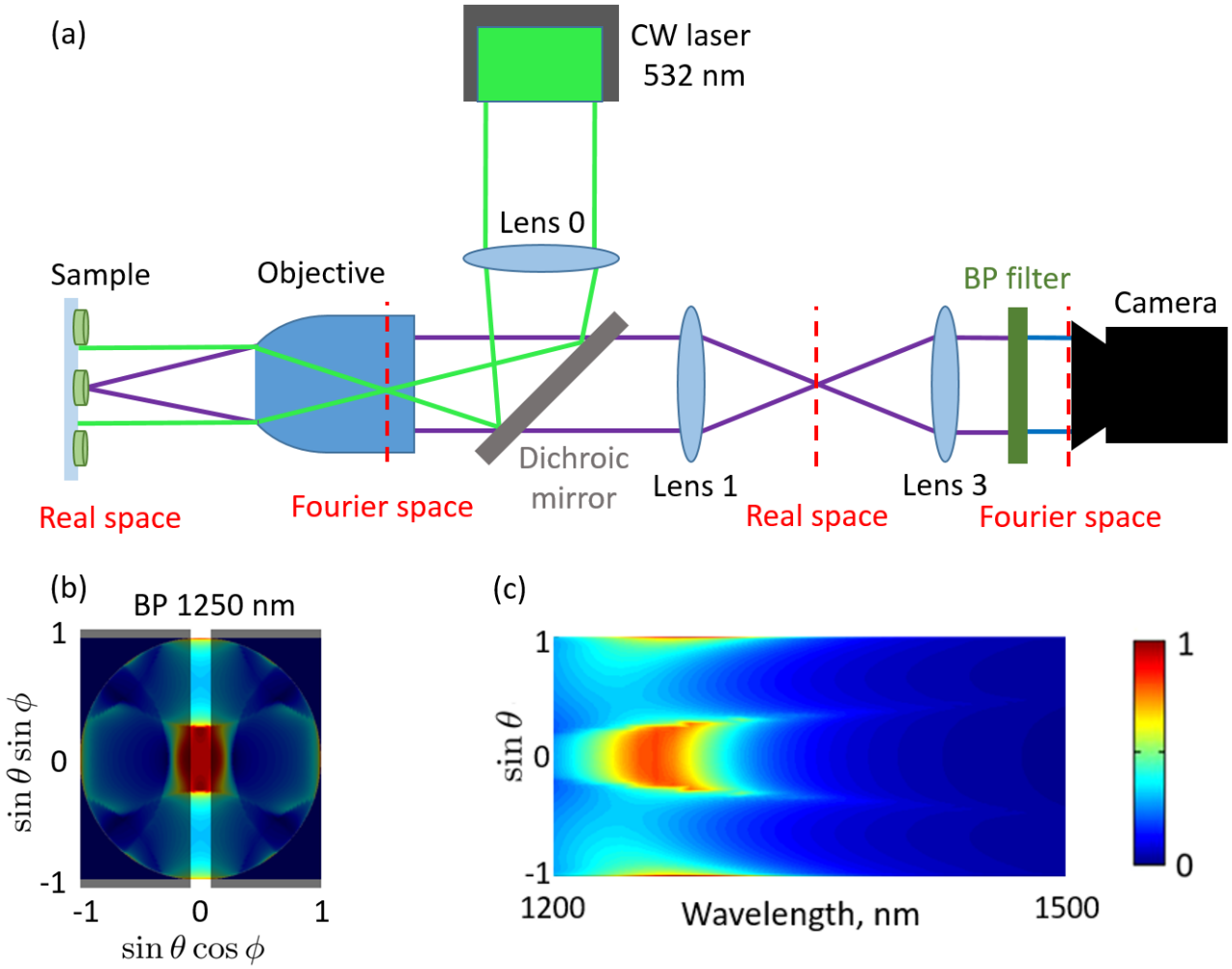

Figure 4.6: (a) Scheme of the experimental setup for BFP imaging of emission (not to scale). The colored rays illustrate the path of the excitation laser (green), PL emission (purple) and filtered PL (blue). (b) The BFP of the objective is imaged onto the entrance slit of the spectrometer. The angular emission distribution is taken from Figure 3.3 and corresponds to a single wavelength of 1250 nm (ED resonance of the nanocylinders in the array). (c) Resulting momentum-resolved spectroscopy image (no BP filter was present in the PL beam path).

The scheme of our setup for BFP imaging is shown in Figure 4.6 (a). A continuous wave (CW) laser producing a collimated beam at a wavelength of 532 nm is used for the excitation. A longpass dichroic mirror (Thorlabs DMLP650R) directs the laser beam to the sample, which is mounted on a 3-axis translational stage and positioned in the FFP of a high-NA objective (either 0.85NA Nikon Plan LWD IMSI 100x or 0.6NA Olympus LUCPlanFL N 40x). Lens 0 focuses the laser beam at the BFP of the objective, so that the excitation hits the sample as a collimated beam, with an approximate diameter of $30 - 50$ μm. The PL emission from the sample is collected by the objective and propagates through a dedicated lens system (lens 1,3) to the visible (Andor EMCCD iXon 897) or NIR (Xenics Xeva-1.7-320) camera. Residual laser light is filtered out by a longpass dichroic mirror. The lens system consists of two 200 mm achromatic doublets (Thorlabs AC254-200-B) arranged in a 4f setup forming the image of the BFP of the objective at the sensor of the camera. Kurvits et al. [136] describe alternative lens system configurations for BFP imaging. We introduce a Thorlabs bandpass filter with FWHM of around 10 nm in front of the camera to selectively map the pattern of the emission

within a narrow spectral region. From the obtained camera images, we can now derive the angular emission characteristics of arbitrary metasurface samples at the wavelength defined by the BP filter. Note that the 4f lens system should have rather low NA, since the interferometric bandpass filters are sensitive to the angle of incidence.

The investigated metasurfaces exhibit resonant behavior leading to the strong wavelength dependence of the emission patterns. In order to study this wavelength dependence, we apply the momentum-resolved spectroscopy technique. We image the BFP of the objective at the entrance slit of the imaging spectrometer (see Figure 4.6 (b)) to measure the momentum-resolved spectra [137, 138] shown in Figure 4.6 (c). The slit selects a thin line of the BFP image, which is then projected onto the camera sensor through a dispersive element of the spectrometer (Andor Kymera 328i). This technique allows us to analyze the emission patterns in one k-space direction at different wavelengths. In other words, momentum-resolved spectroscopy yields cross-sections of the photonic band structure, while the BFP imaging yields the isofrequency slices of the photonic band structure.

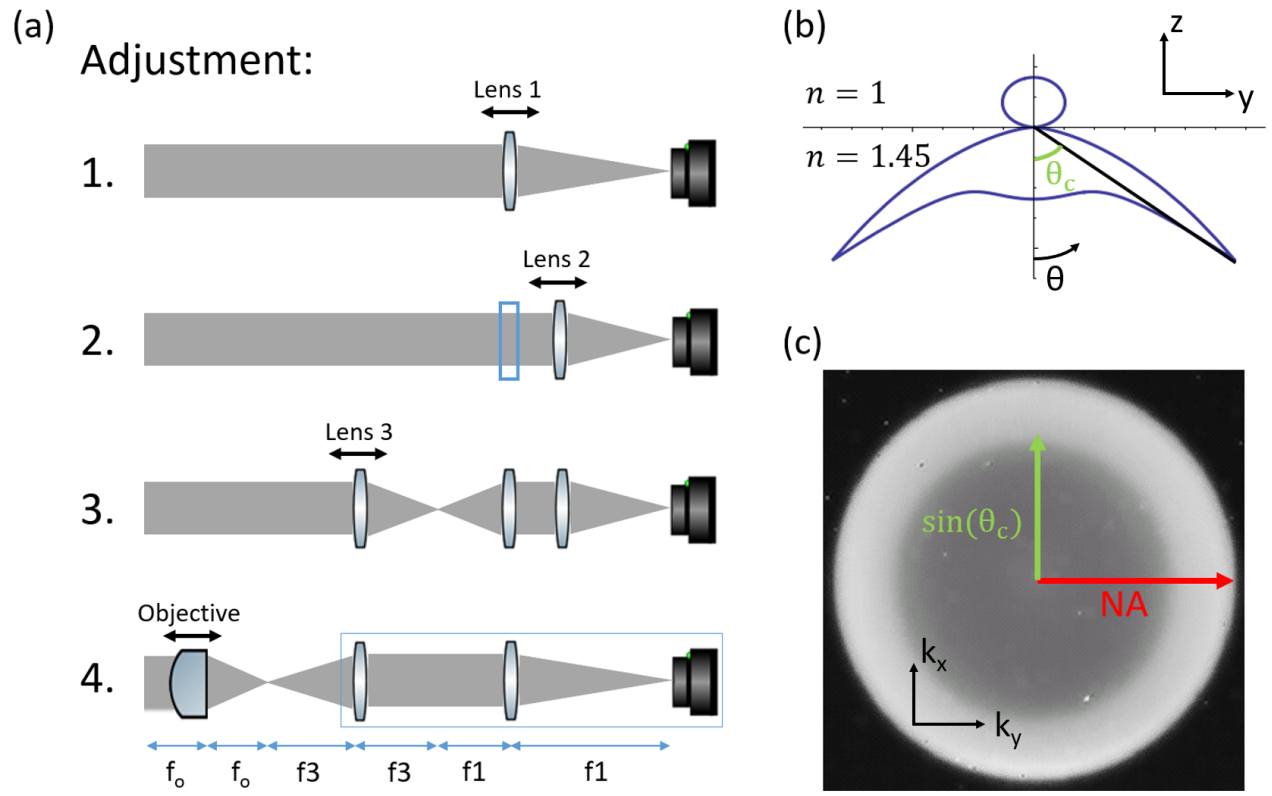

Figure 4.7: (a) The adjustment procedure for the lens system imaging the BFP of the objective at the sensor of the camera. (b) Calculated emission pattern of a point electric dipole placed at the interface between two different dielectric media. (c) The BFP image of the emission from QDs placed onto the glass substrate. Color from black (low) to white (high) indicates the emission intensity.

Figure 4.7 (a) shows the adjustment procedure of the 4f system, which images the BFP of the objective at the camera sensor. The steps are following: 1) We use a collimated laser beam (grey) incident onto the camera as a light source and place the first lens 1 in the optical path. We move the lens 1 until the image from the camera shows the smallest focused laser spot. This means that the distance between the lens 1 and the camera sensor is matched with the focal distance $f1$ of the lens 1. 2) We remember the position of the lens 1 and take it out. We place

the lens 2 with a lower focal distance $f2$ and repeat the first step with it. 3) We return the lens 1 to its' initial position and put the third lens in the optical path. We vary the position of the lens 3 until we observe the smallest laser spot in the image. Now the distance between the lens 3 and lens 1 is equal to the sum of the focal distances $f1 + f3$ and the laser beam passing these two lenses stays collimated. 4) We take out the lens 2 and introduce the objective. Now we move the objective to minimize the laser spot again. This smallest laser spot is in fact a BFP image of the collimated laser beam. Note that the wavelength of the laser used for the adjustment procedure should be spectrally close to the probed emission from the metasurface sample to reduce possible chromatic aberrations.

To check the proper functioning of the constructed setup, we performed test measurements with QDs placed on a glass substrate. The emission was collected through the other side of the substrate with an oil-immersion objective (Nikon). When a QD is placed at the interface between two dielectric media with different refractive indices, its emission preferably couples to the dark modes propagating above the critical angle $\theta_c = \text{asin}(1/1.45)$ in the media with a higher value of the refractive index [113, 135] (see Figure 4.7 (b)). The measured BFP image of the emission is shown in Figure 4.7 (c). We observe a bright ring (higher emission intensity) with an inner radius corresponding to the $sin(\theta_c)$ and outer radius limited by the NA of the objective [135]. The ring is rotationally symmetric since the emission is averaged over the randomly oriented emitting dipole moments of the QDs ensembles.

To calibrate the BFP image, i.e. to assign each pixel with a corresponding wavevector, in principle, one can use an objective with known NA (see Figure 4.7 (c)). Alternatively, the dichroic mirror can be replaced by a regular beamsplitter, allowing to record the BFP of the diffraction of the short-wavelength excitation laser light by the periodic metasurface sample. In this case, the BFP image will appear as a number of bright spots forming the reciprocal lattice. The distances between the spots (diffraction orders) can be easily estimated from the laser light wavelength and the period of the metasurface.

Chapter 5

Shaping emission pattern and spectrum by dielectric metasurfaces

5.1 Mie-resonant silicon nanocylinder arrays for enhancing the photoluminescence emission

5.1.1 Motivation

Owing to their unique ability to enhance and direct spontaneous emission from nanoscale sources, optical nanoantennas remain an important research topic in nanophotonics [13–15, 32]. Apart from the well studied concept of plasmonic nanoantennas, dielectric nanoantennas have started to gain increasing attention during the last few years [56] due to their low-losses and associated high QY of coupled emitter systems. At the same time they allow for enhancement of the LDOS through the excitation of Mie resonances [45, 139].

Researchers are usually considering two alternative design concepts for directional nanoantennas. The first concept assumes engineering of a single resonant nanoparticle [59, 89, 92, 93, 140, 141]. In this case, both the radiative decay rate enhancement and the directionality rely on the excitation of resonant modes in the nanoparticle. Indeed, for the specific case of low-loss dielectric nanoantennas, the LDOS enhancement was first demonstrated theoretically [140] and then experimentally [142]. Furthermore, an experimental work by Cihan et al. [94] demonstrates that a directional emission pattern can be achieved by tailoring the strengths and phases of different Mie-type modes excited in the single nanoparticle. The second common approach to designing a nanoantenna is to arrange several nanoparticles in a way that the light scattered by the different nanoparticles will interfere constructively along the desired direction and destructively along all other directions (see Section 2.2.2). This method was employed to demonstrate directional scattering and emission in various nanoantenna architectures, ranging from rather simple systems consisting of two nanoparticles [143, 144] to more complex Yagi-Uda type nanoantennas [16, 17, 21, 139], periodic nanoparticle arrangements [26, 36, 145, 146] and Bullseye antennas [147, 148].

Optical metasurfaces, which are composed of planar arrangements of designed nanoresonators, allow for combining both of these nanoantenna design concepts. Indeed, plasmonic

metasurfaces were already demonstrated to provide many degrees of freedom for manipulating spontaneous emission from nanoscale emitters integrated in the metasurface architecture [26, 27, 145]. Here we experimentally demonstrate spectral reshaping and out-of-plane directional emission enhancement by coupling of the intrinsic fluorescence from a glass substrate in the $600-900\,\mathrm{nm}$ spectral range to square arrays of Mie-resonant a-Si:H nanocylinders. To achieve the desired emission spectrum and pattern, we combine, emission enhancement by the Mie-resonant dielectric nanoantennas with a coherent scattering in a tailored periodic arrangement. By choosing the lattice period to match the wavelength of the magnetic dipolar Mie-type resonance of the nanocylinders, we shape the air semi-space emission into a single lobe out of the substrate plane. A sketch of the system under investigation is shown in Figure 5.1. A CW laser emitting at a wavelength of $532\,\mathrm{nm}$ is exciting the color centers in the glass substrate. These color centers originate from various types of point defects and impurities, whose exact composition is influenced by the fabrication process of the glass substrate [149–152]. The fluorescence emission from the substrate covers a broad spectral range of $600-900\,\mathrm{nm}$, and is significantly stronger than the fluorescence originating from the material of the nanocylinders. To clarify the latter we measured the fluorescence signal from layers of the same a-Si:H material deposited on the high-quality low-fluorescent quartz coverslips.

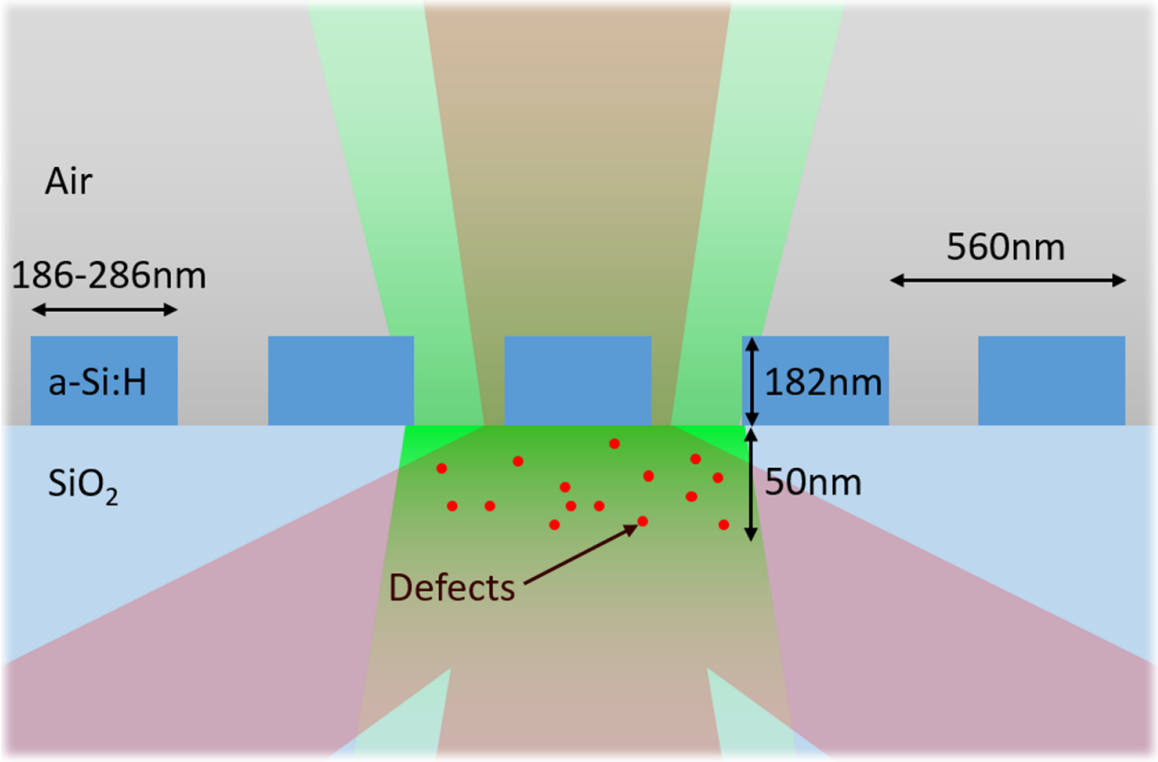

Figure 5.1: Artist's impression of a metasurface composed of Mie-resonant a-Si:H nanocylinders and placed on a fluorescent glass substrate. The laser emission (green) excites the color centers in the glass substrate (red dots), which in turn reemit in the $600-900\,\mathrm{nm}$ spectral range (red).

5.1.2 Experimental characterization

Following the steps described in Section 4.1, we fabricated seven different metasurfaces with nanocylinder diameters varying between $186\,\mathrm{nm}$ and $286\,\mathrm{nm}$ (measured by SEM). The lattice

constant and the nanocylinder height were identical in all the metasurfaces and equal to 560 nm and 182 nm, respectively. SEM images of a typical sample are shown in Figure 5.2. Note that we covered the samples with a 15 nm layer of indium tin oxide (ITO) providing surface conductance and preventing charge accumulation during SEM imaging.

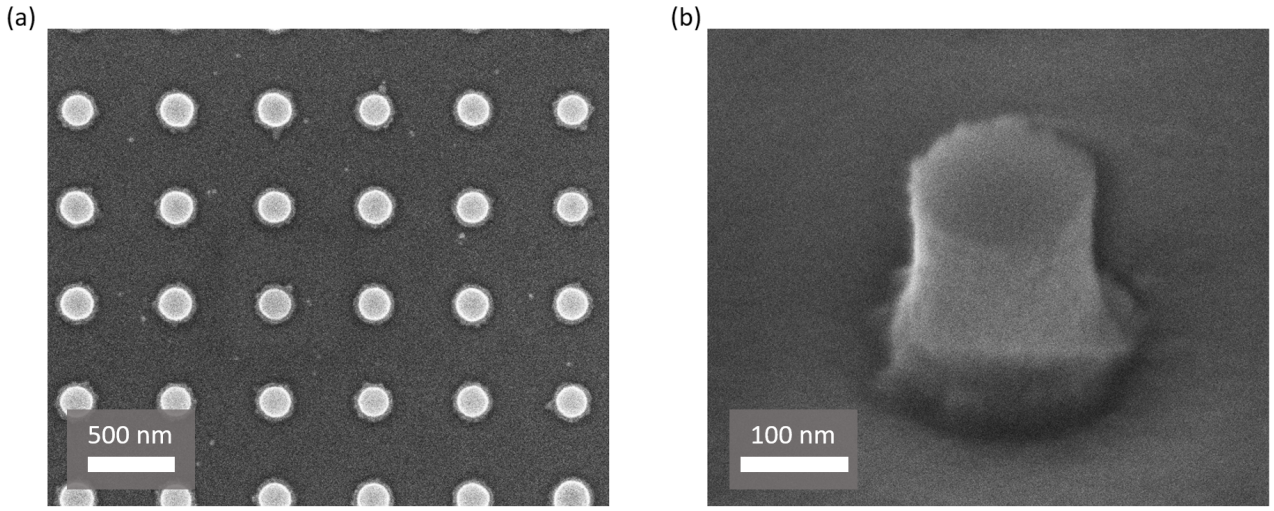

Figure 5.2: SEM images of a typical metasurface sample. (a) Top view. (b) Oblique view close up of a single a-Si:H nanocylinder. The sample is fabricated and data is obtained by Katie E. Chong.

First, we characterized the resonant properties of the metasurfaces in the visible spectral range by measuring the near-normal-incidence transmittance spectra of the fabricated samples using the spectroscopy setup described in Section 4.2. Figure 5.3 (a) shows a measured transmittance spectrum for the metasurface composed of nanocylinders with a diameter of 286 nm. To identify the Mie-resonances responsible for the shape of the transmittance spectrum, we numerically calculated the normal-incidence transmittance spectra of the metasurface using the COMSOL multiphysics (see Section 3.3 for details on the calculations). The material of the coverslip substrate was SiO_2 glass and the refractive index data was taken from a work by Malitson [153]. For the refractive index of a-Si:H we used experimental data obtained from ellipsometry measurements on unstructured a-Si:H films (see Figure 4.1). The geometrical parameters of the unit cell were following: the lattice constant was fixed to 560 and the nanocylinder diameter and height were allowed to vary within the accuracy limits of SEM imaging to optimize the agreement between the experimental and measured data. A diameter of 210 nm and a height of 160 nm were found to provide the best agreement. The corresponding calculated spectrum is shown alongside the experimental spectrum in Figure 5.3 (a). Note that the dimensions of the nanocylinders used in simulations are around 20% smaller as compared to those measured via SEM imaging. This discrepancy is likely due to deviations of the a-Si:H refractive index in the structured sample from the unstructured film and imperfections of the fabricated nanocylinder shape [154, 155].

Both experimental and calculated spectra exhibit three pronounced minima appearing at wavelengths of 620 nm, 730 nm and 844 nm. In Figure 5.3 (b) we depict the calculated electric field profiles in the vertical cross-section through the center of one of the nanocylinders for the resonant wavelengths of 730 nm and 844 nm. We compare the calculated field profiles with

those associated with different Mie-modes shown in Figure 2.4 and identify the resonance of the nanocylinder excited at 730 nm as the ED resonance and the resonance occurring at 844 nm as the MD resonances. The minimum at 620 nm is likely associated to a quadrupolar Mie-mode and was not further considered in the present section.

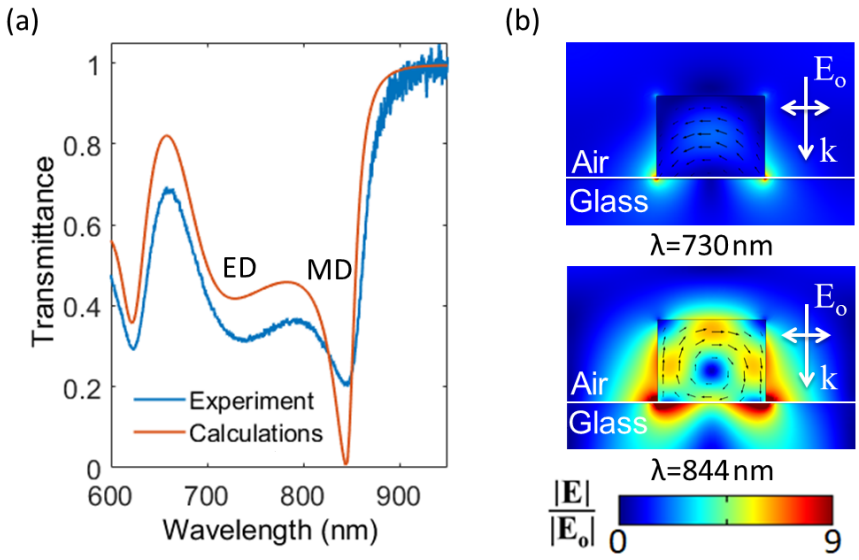

Figure 5.3: (a) Experimental and calculated normal-incidence transmittance spectra of the a-Si:H metasurface with a nanocylinder diameter of 286 nm. (b) Calculated electric field distribution of the ED and MD resonances excited by a normally incident plane wave at the wavelengths of 730 nm and 844 nm, respectively. Reprinted with permission from [131]. Copyright (2018) American Chemical Society. The normal-incidence transmittance was measured by Katie E. Chong.

Next, we measure the emission spectra of our samples using a confocal microscope system (Picoquant MicroTime-200) with a 532 nm laser excitation. The emission was collected by an 0.25 NA objective (Olympus, Plan N) and coupled to a visible spectrometer (Horiba iHR320). The measured fluorescence spectra are depicted in Figure 5.4 (solid lines). The dashed lines show the transmittance spectra of the respective metasurfaces. As a reference, the fluorescence spectrum measured from the bare glass substrate next to the metasurfaces is also shown (grey areas). We observe reshaping of the fluorescence spectra by the metasurfaces. This reshaping shows a systematic dependence on the nanocylinder diameter. In particular, the fluorescence signal from the metasurfaces peaks near the spectral position of the ED and MD resonances of the nanocylinders as observed in the transmittance spectra. This effect can be explained by an increase of the QY of the system at resonance. Typically, the QY values of such impurities are low due to the dominant intrinsic decay processes. This, in turn, leads to a significant effect of the radiative decay rate enhancement on the overall fluorescence signal. The room-temperature lifetime of the excited state of the impurities was out of the measurement range of the MicroTime-200 system. We notice, that the MD resonance provides higher fluorescence signal enhancement compared to the ED resonance. This is in accordance with the literature, where the MD resonance was also demonstrated to lead to more pronounced enhancement effects in other platforms [35, 156]. Partly, this effect may be due to the fact that in current and other mentioned works, the MD resonance appears at higher wavelengths compared to other Mie-resonances, and thus experiences lower dissipate losses in a-Si:H or other materials.

In addition, according to the mode profiles in Figure 5.3 (b), the MD mode concentrates the light much more efficiently in the fluorescent substrate.

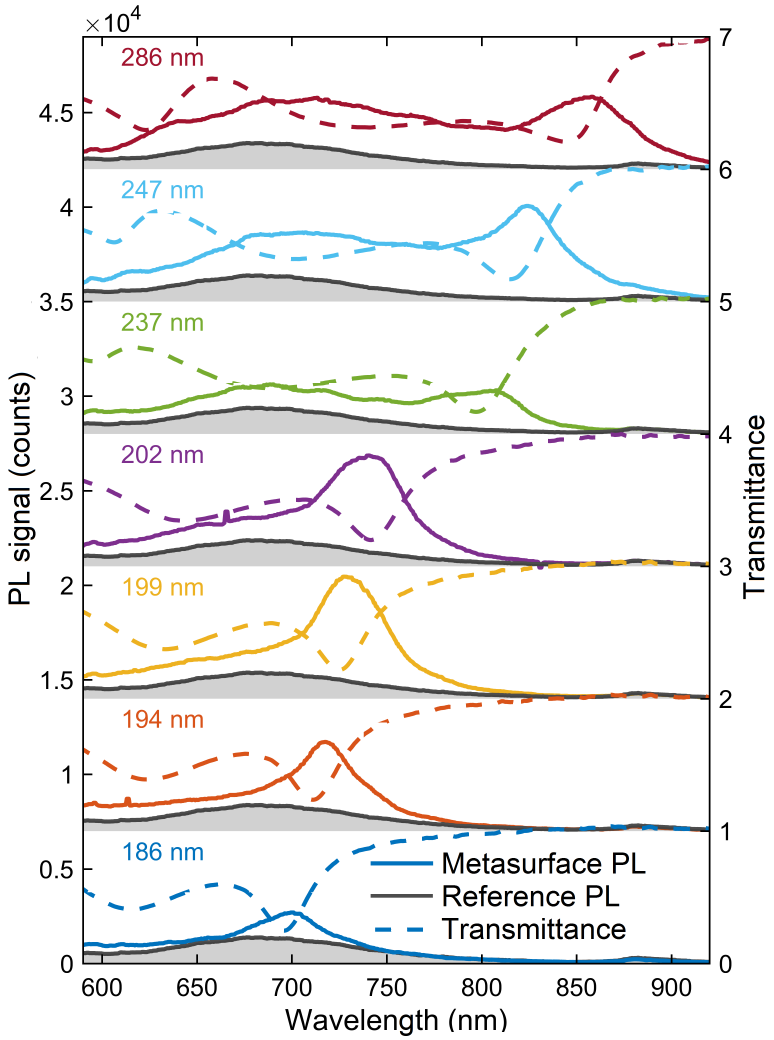

Figure 5.4: Experimentally measured fluorescence spectra (solid lines) of the metasurfaces for a systematic variation of the nanocylinder diameter (colored label). The grey area represents the reference fluorescence spectrum of the bare glass substrate. The dashed lines show the transmittance spectra of the corresponding metasurface. Reprinted with permission from [131]. Copyright (2018) American Chemical Society. The normal-incidence transmittance was measured by Katie E. Chong. The fLorescence spectra were measured by Justus Bohn.

As a next step, we focus our study on the metasurface with the nanocylinder diameter of 286 nm. For this sample, the fluorescence signal is enhanced by a factor of 28 at wavelength of 850 nm corresponding to the MD resonance of the nanocylinders in the arrays. We performed BFP imaging of the emission from the metasurface using a 0.85 NA objective (see Chapter 4 for details on the BFP measurements) to study the directionality of the emission at the resonance. To selectively probe the emission at the MD resonance, we introduced a bandpass filter with center wavelength of 850 nm and a passband width of 10 nm in the experimental setup. The BFP image recorded through the filter is depicted in Figure 5.5 (a). We observe the fourfold symmetry in the emission pattern, which corresponds to the lattice geometry. Furthermore, the BFP image exhibits a bright spot at the center, which means the preferable out-of-plane emission. We further explore this emission pattern in Figure 5.5 (b), which shows the $k_y = 0$

cross section of the angular emission in the air semi-space. The emission is squeezed into a narrow lobe directed perpendicular to the metasurfacee plane.

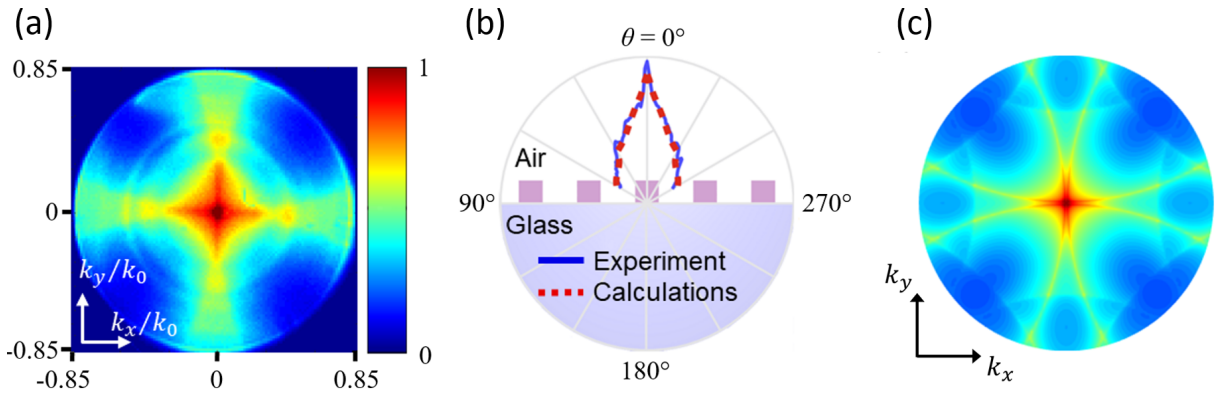

Figure 5.5: (a) Experimentally measured BFP image of the emission from the metasurface with nanocylinder diameter of 286 nm passed through 850 nm bandpass filter, $k_0 = (2\pi/\lambda)$. (b) Corresponding experimental (blue solid line) and calculated (red dashed line) air semi-space emission pattern cross-section for $k_y = 0$. (c) Calculated BFP image. Reprinted with permission from [131]. Copyright (2018) American Chemical Society.

5.1.3 Far-field emission pattern simulations

In order to verify the experimental data and the physics behind the spatial emission reshaping, we perform numerical simulations of the emission patterns. This simulations require us to take into account the periodicity of the metasurface and inhomogeneous background: the upper semi-space is air and the lower semi-space is glass. Therefore, we utilize the reciprocity principle described in Section 3.1.2.

We consider the emitting color centers in the glass substrate as homogeneously distributed point electric dipoles. The emitting dipole moments on average are isotropically oriented. Therefore, the integral in Equation (3.7) simplifies to the intensity of the electric field evaluated at the position of the emitting electric dipole. Next, in accordance with the Equation (3.8), the far-field emission intensity $P(\theta, \phi)$ along the direction (θ, ϕ) is proportional to $\iiint_V |\mathbf{E}(\theta, \phi, \mathbf{r})|^2 d^3r$, where $\mathbf{E}(\theta, \phi, \mathbf{r})$ is the electric field excited in the metasurface by a plane wave incident onto the structure along the same direction and evaluated at the position $\mathbf{r}$. The integration is done over the volume V containing the emitters. In our simulations, we restrict the volume V to the 50 nm thick layer of glass laying just below the nanocylinders. The thickness of 50 nm is chosen to limit the consideration to the emitters with effective near-field coupling to the resonances of the nanocylinders, which are thus dominantly contributing the far-field emission. In Figure 5.6 we depict the intensity of the electric near-field excited in the metasurface at the wavelength of 850 nm averaged over a hypothetical plane parallel to the interface and displaced by the distance h from it towards the substrate semi-space, as schematically shown in the inset. The electric near-field is enhanced by the MD resonance of the nanocylinders and decays with increasing separation distance. The most significant enhancement is within the thickness of 50 nm, which we chose for our simulations.

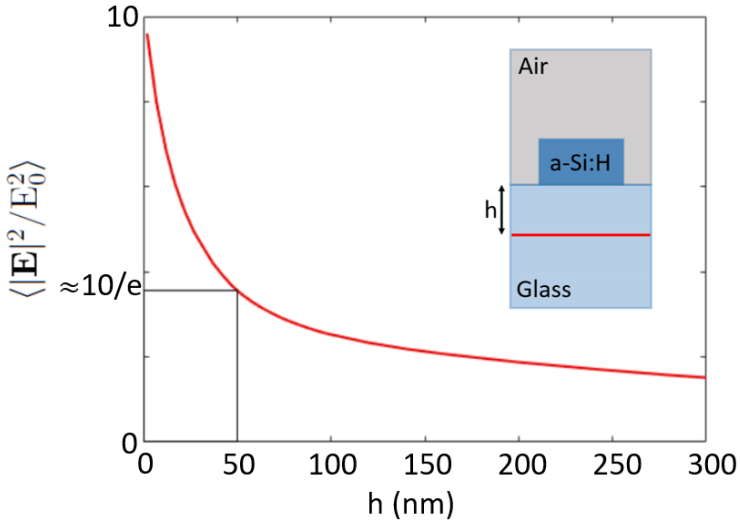

Figure 5.6: Calculated normalized electric field intensity inside the substrate excited by a normally incident plane wave at the wavelength of 850 nm and averaged over a plane parallel to the interface and displaced by a distance h from it, as schematically shown in the inset. Reprinted with permission from [131]. Copyright (2018) American Chemical Society.

The absorption $A(\theta, \phi)$ of a plane wave incident on the metasurface along the direction (θ, ϕ) is proportional to $\iiint \varepsilon''(\mathbf{r})|\mathbf{E}(\theta, \phi, \mathbf{r})|^2 d^3r$, where ε'' is the imaginary part of the dielectric permittivity and integration is taken over the whole space (see Section 2.4.2). The materials of the metasurface and glass substrate are nearly lossless at the wavelength of 850 nm. Therefore, if we add a low artificial loss factor to the 50 nm thick layer of glass substrate, the absorption becomes proportional to the integral of the electric field intensity over the layer containing emitters. Therefore, $A(\theta, \phi)$ can be used as a measure for $P(\theta, \phi)$.

We utilize the FMM method (see Section 3.3) to calculate the angular-resolved absorption $A(\theta, \phi)$ by the metasurface. In our FMM model, we used the same geometrical parameters as for the calculations in Figure 5.3. The refractive index distribution within the unit cell was as well the same, except for additional loss factor of $0.001i$ assigned to the refractive index of the 50 nm thick layer of glass substrate located just below the nanocylinder. Note that the value of 0.001 is low enough that it doesn't influence the electric field distribution. A plane wave with a wavelength of 850 nm was incident from the air semi-space. The angles of incidence were varied within the following ranges: ϕ was ranged from 0° to 45° making use of the fourfold and mirror symmetries of the metasurface geometry and θ was ranged from 0° to 58°. The upper limit for the polar angle θ corresponds to the NA of 0.85 of the collection objective used in experiments.

To reconstruct the experimental BFP image shown in Figure 5.5 (a), we calculated the angular-resolved emission intensity by summing up the angular-resolved absorption for TE and TM polarized incident plane waves and performing the transformations according to Equations (4.1) to (4.3). The calculated BFP image is depicted in Figure 5.5 (c). The red dashed lines in Figure 5.5 (b) demonstrate the $k_y = 0$ cross-section of the calculated air semi-space emission pattern. We observe a good overall agreement between the measured and calculated data. The discrepancy in the fine features is likely due to the imperfections of the fabricated sample and the optical measurement setup.

5.1.4 Analytical model

The analytical model suggested by Lutz Langguth and Femius Koenderink [25, 26, 45] allows to shed light onto the origin of the emission pattern shape. The model considers the active metasurface as a phased array and the emission pattern is formed in accordance with Equation (2.47). At the operating wavelength of 850 nm, the emission of a single emitter located close to a nanocylinder weakly couples to its MD mode. Next, the oscillating magnetic dipole moment of the nanocylinder launches a cylindrical wave (E_{drive}) driving the neighboring nanocylinders with a retarded phase. The interference of the emission scattered by different nanocylinders results in a narrow lobe directed in perpendicularly to the metasurface plane.

Since the nanocylinders in the metasurface are identical, we put the form factor $S_j(\mathbf{k})$ and the polarizability α_j in Equation (2.47) out of the summation. Then the expression for the angular far-field emission $\mathbf{E}(\mathbf{k})$ simplifies to:

$$\mathbf{E}(\mathbf{k}) \propto \sum_j E_{drive} e^{i\mathbf{k}\cdot\mathbf{r}_j} \tag{5.1}$$

where the summation is performed over the nanocylinders composing 2D periodic array. We can further transform [45] the Equation (5.1) to:

$$\mathbf{E}(\mathbf{k}) \propto \mathfrak{F}[E_{drive}] * \mathfrak{F}[\sum_j \delta(\mathbf{r} - \mathbf{r}_j)] \tag{5.2}$$

where $\mathfrak{F}$ denotes Fourier transform and $*$ denotes convolution. The Fourier transform of the driving cylindrical wave results in the circle in the reciprocal space. The radius of the circle is equal to the wavevector of the cylindrical wave. The second term in Equation (5.2) is the Fourier transform of the array factor, which assembles the reciprocal lattice. Finally, the convolution of both terms results in an array of such circles located at the reciprocal lattice points.

The driving cylindrical wave propagating along the array is in fact the lattice mode associated with the Rayleigh anomaly (not to be confused confuse it with the Wood's anomalies only attributed to the surface plasmon polaritons [157]), where the light scattered by the nanocylinders interferes constructively along the array plane. The excitation conditions for the lattice modes, when the in-plane component of the wavevector of the incident plane wave coincides with the wavevector of the lattice mode, are represented by the following equations for air and substrate semi-space:

$$\frac{2\pi}{\lambda} = \sqrt{\left(\frac{2\pi}{\lambda}\sin\theta\cos\phi + p\frac{2\pi}{P}\right)^2 + \left(\frac{2\pi}{\lambda}\sin\theta\sin\phi + j\frac{2\pi}{P}\right)^2} \tag{5.3}$$

$$n\frac{2\pi}{\lambda} = \sqrt{\left(\frac{2\pi}{\lambda}\sin\theta\cos\phi + l\frac{2\pi}{P}\right)^2 + \left(\frac{2\pi}{\lambda}\sin\theta\sin\phi + m\frac{2\pi}{P}\right)^2} \tag{5.4}$$

where p,j,l and m are integers defining the diffraction orders and $n = 1.51$ is the refractive index of the glass substrate.

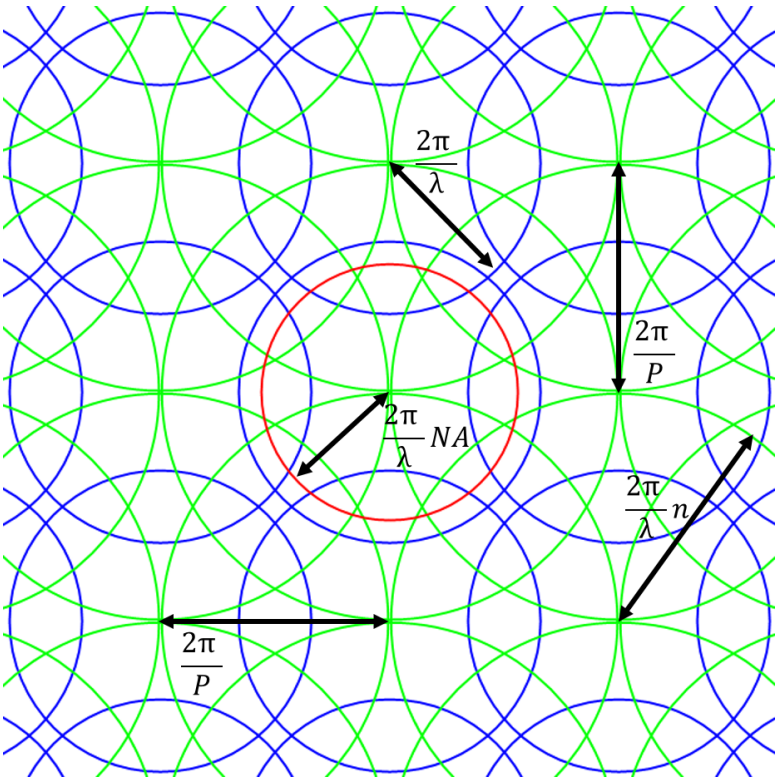

Figure 5.7: Solutions of the Equation (5.3) (blue) and Equation (5.4) (green). The red circle has a radius of $(2\pi/\lambda)$NA, where $\lambda = 850\,\text{nm}$ and NA$= 0.85$. The radii of the blue and green circles are equal to $(2\pi/\lambda)$ and $(2\pi/\lambda)n$, respectively, where $n = 1.51$ is the refractive index of the substrate at the wavelength of 850 nm. The centers of the blue and green circles are located at the reciprocal lattice points, i.e. forming a square lattice of period $(2\pi/P)$, where $P = 560\,\text{nm}$ is the period of the metasurface in real space.

Figure 5.7 shows the solutions of the Equation (5.3) (blue) and Equation (5.4) (green) for the wavelength of 850 nm. The coordinate system is the same as in the Figure 5.5 (c). Indeed, they form an array of the circles located at the reciprocal lattice points. Blue and green circles represent the dispersion of the lattice mode in air and in the glass substrate, respectively. The red circle demonstrates the part of the reciprocal space captured by the collection optics and has a radius of $(2\pi/\lambda)$NA, where $\lambda = 850\,\text{nm}$ and NA$= 0.85$ is the NA of the objective used in the BFP imaging. Clearly, the underlying patterns in Figure 5.5 (a,c) and Figure 5.7 show a good agreement.

5.1.5 Collection efficiency

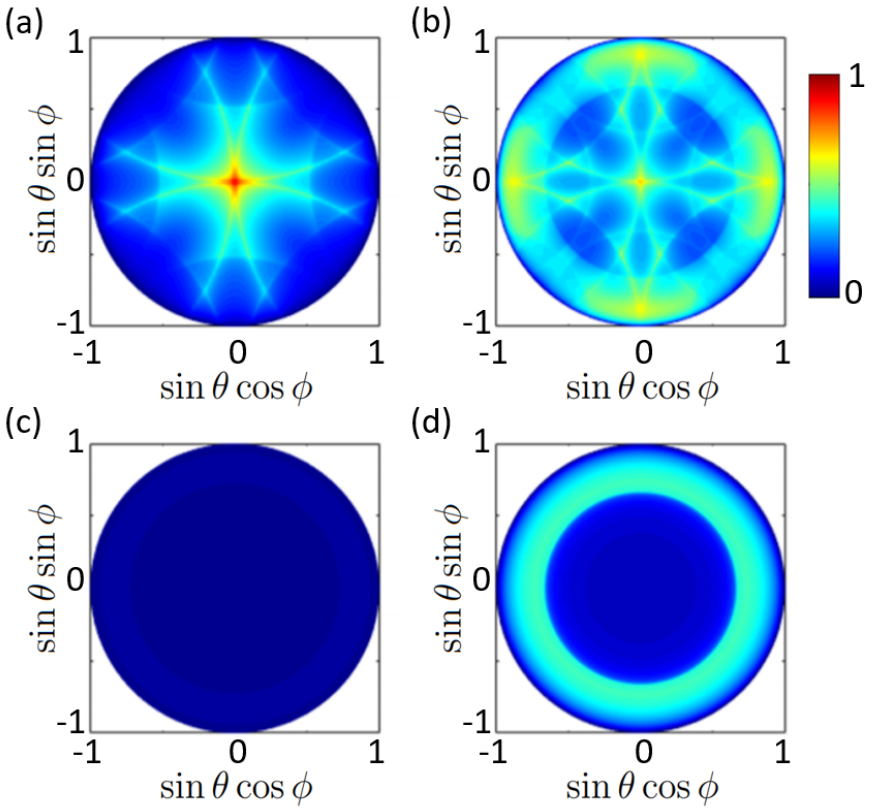

Figure 5.8: Intensity of the angle-resolved far-field emission from the 50 nm emitting layer below the nanocylinders (a) into the air semi-space and (b) into the substrate semi-space. Intensity of the angle-resolved emission from a 50 nm layer at a glass-air interface without nanocylinder array (c) into the air semi-space and (d) into the substrate semi-space. All intensities are normalized to the same global maximum. Reprinted with permission from [131]. Copyright (2018) American Chemical Society.

We experimentally observed that the metasurfaces induce a reshaping of the resonantly enhanced emission in the air semi-space into a narrow lobe directed out of the metasurface plane towards the collection objective. Therefore we expect the collection efficiency enhancement. Here we evaluate the role of the collection efficiency enhancement in the fluorescence signal enhancement (see Section 2.4.2) and analyse the limitations of further improvement of the collection efficiency.

We calculated the angular distribution of the emission of our metasurface into the air and substrate semi-spaces. For reference, we also calculated the angle-resolved emission intensity for the case without the metasurface, i.e. for an air-glass interface. In both cases, we assumed a 50 nm emitting layer of glass located just below the nanocylinders or at the air-substrate interface, respectively. The parameters of the metasurface are the same as in the calculations for Figure 5.5 (c) and the wavelength is 850 nm. The results are presented in Figure 5.8. Based on this data, we can estimate that the 0.85 NA objective positioned in the air semi-space collects about 10% of the light emitted from the metasurface and only 6% of light from the layer of emitters at the substrate without nanocylinders. A larger enhancement in the collection efficiency is observed for a 0.25 NA objective used in PL spectroscopy. It collects 0.3% of the light emitted from the metasurface and only 0.082% for the case without the metasurface. In

all these cases, however, the collection efficiency stays low due to the preferable emission into the dark modes of the substrate.

We can estimate a collection efficiency enhancement factor of 3.65 for the 0.25NA objective at the wavelength of 850 nm. The calculated plane wave excitation enhancement at 532 nm gives a factor of 1.2. Taking into account the total experimentally measured fluorescence signal enhancement of 28, we conclude that the enhancement of the QY over all emitters additionally provides a factor of around 6. Note, however, that, as mentioned before, such factorization is only valid for case of a single emitter, and thus can only be contributed a rough estimation for the experimental system under investigation.

5.2 Manipulation of photoluminescence emission with semiconductor metasurfaces exhibiting magnetic quadrupole resonances.

5.2.1 Motivation

In the previous section we experimentally observed that the a-Si:H nanocylinder metasurfaces induced a reshaping of the resonantly enhanced emission in the air semi-space into a narrow lobe directed out of the substrate plane. The reshaping was explained by coherent scattering of the emitted light in the nanocylinder array. Apart from this "array factor", metasurfaces offer an additional degree of freedom for manipulating the emission directionality. For example, Langguth et al. [26] reported a plasmonic metasurface imparting an asymmetric directional pattern on the spontaneous emission. While the plasmonic lattice enables directional out-coupling of light along a set of preferential directions, the predominance along a specific predefined (non-normal) direction can be introduced by tailoring the scattering properties of the individual elements (see Figure 1.1 (b)).

The design of a single directional element usually requires the excitation of higher order resonances [89]. High-refractive-index dielectric nanoparticles, such as cubes or cylinders, are a convenient platform, since they support higher order Mie-type modes and are easy to fabricate [158]. However, most works, including the work described in the previous section, investigating directional emission from light-emitting dielectric metasurfaces so far merely utilized the dipolar modes of their constituent resonators [36, 131], thus providing only low directivity from the single nanoparticle. Here we investigate dielectric metasurfaces supporting the MQ resonances. Importantly, the quadrupole resonances are associated with higher quality factors and allow for squeezing the emission into narrower lobes, compared to the dipole resonances of previously demonstrated light-emitting metasurfaces [131, 142]. These properties of the quadrupole resonances make them especially suited for light-emission applications.

Our metasurfaces are made from epitaxial III-V direct bandgap semiconductors with high efficiency InAs QDs incorporated during growth. The InAs QDs emission bandwidth covers a wavelength range from approximately 1100 nm to 1300 nm. The GaAs nanocylinders have a height of 400 nm and incorporate five layers of InAs QDs in accordance with Figure 5.9 (a). They are positioned on low-index oxide pedestals with a height of 500 nm and covered by 200 nm of silica. The entire structure is supported by a bulk GaAs substrate. Since the standard dielectric Mie-resonators, such as nanocylinders, preferably enhance the internal fields, the full potential for emission control via the Mie modes is realized when the emitters are embedded inside the nanocylinders. Therefore, our architecture provides an optimal spatial overlap of the near-fields enhanced by the MQ resonance and the emitters. Previous attempts at integrating emitters into the dielectric nanoresonators were limited to inefficient emitters [159].

We fabricated three metasurfaces with different periods P allowing to probe the influence of the periodicity. We demonstrate that both the "array factor" and the resonant properties of individual dielectric nanocylinders composing the metasurface provide a comprehensive control

over the emission pattern.

The projects presented in the current and the next sections were a collaboration with Sandia National Laboratories. GaAs metasurface samples were fabricated and characterized (SEM imaging, reflectance and PL spectroscopy) by Sheng Liu. The broken-symmetry metasurface introduced later was designed by Sheng Liu. The role of the author was to study experimentally the spectra and directionality of emission, analyse the experimental data and simulate the linear spectra and emission patterns of the metasurfaces. For a sake of completeness we present the contributions of other people in this manuscript.

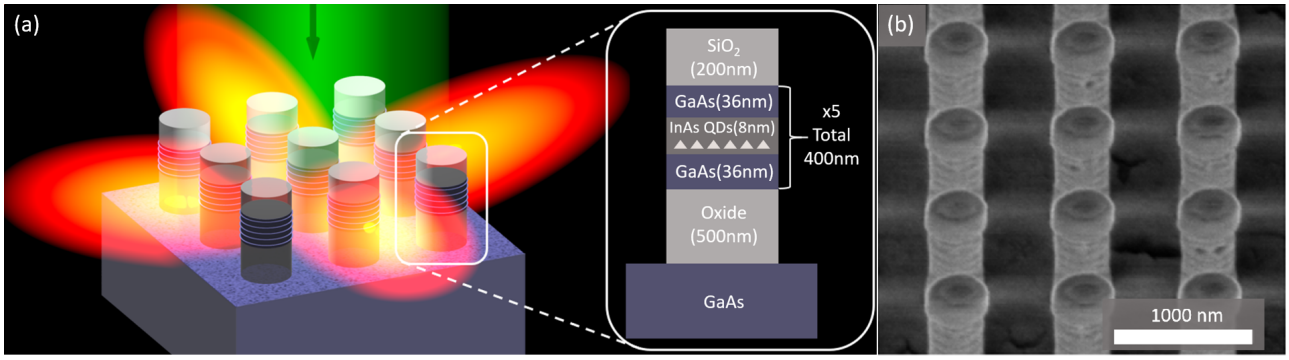

Figure 5.9: (a) Artist's impression of Mie-resonant GaAs nanocylinders incorporating layers of InAs QDs. The inset shows the structure of a single GaAs resonator situated on a GaAs substrate and a low-index oxide pedestal. Each nanoresonator incorporates 5 layers of InAs QDs. The resonator is covered by a low-index cap. (b) Oblique-view SEM of a typical symmetrical GaAs metasurface sample incorporating 5 layers of QDs. The scale bar corresponds to 1000 nm. The samples were fabricated and SEM images were obtained by Sheng Liu. Reprinted with permission from [111]. Copyright (2018) American Chemical Society.

5.2.2 Experimental characterization

Following the steps described in Section 4.1, we fabricated three metasurfaces with the nanocylinder diameter of $D = 440$ nm (measured by SEM) and different periods. The variant periods P are 800 nm, 880 nm and 980 nm. A typical scanning electron microscopy (SEM) image of a fabricated GaAs nanocylinder metasurface is presented in Figure 5.9 (b). First, we focus our study on a metasurface a period $P = 880$ nm. For this metasurface sample, the different features in the emission characteristics (as discussed below) were most pronounced. As a first step, in order to characterize the modal structure of the fabricated nanocylinder metasurface, we measure the near-normal-incidence linear optical reflectance spectrum using the setup described in Section 4.2. The results are shown in Figure 5.10 (a). We observe two pronounced peaks at 1300 nm and 1550 nm wavelength corresponding to the in-plane MD and ED resonances [158], respectively. Furthermore, we notice other small features (narrow dips) in the reflectance spectra at smaller wavelengths.

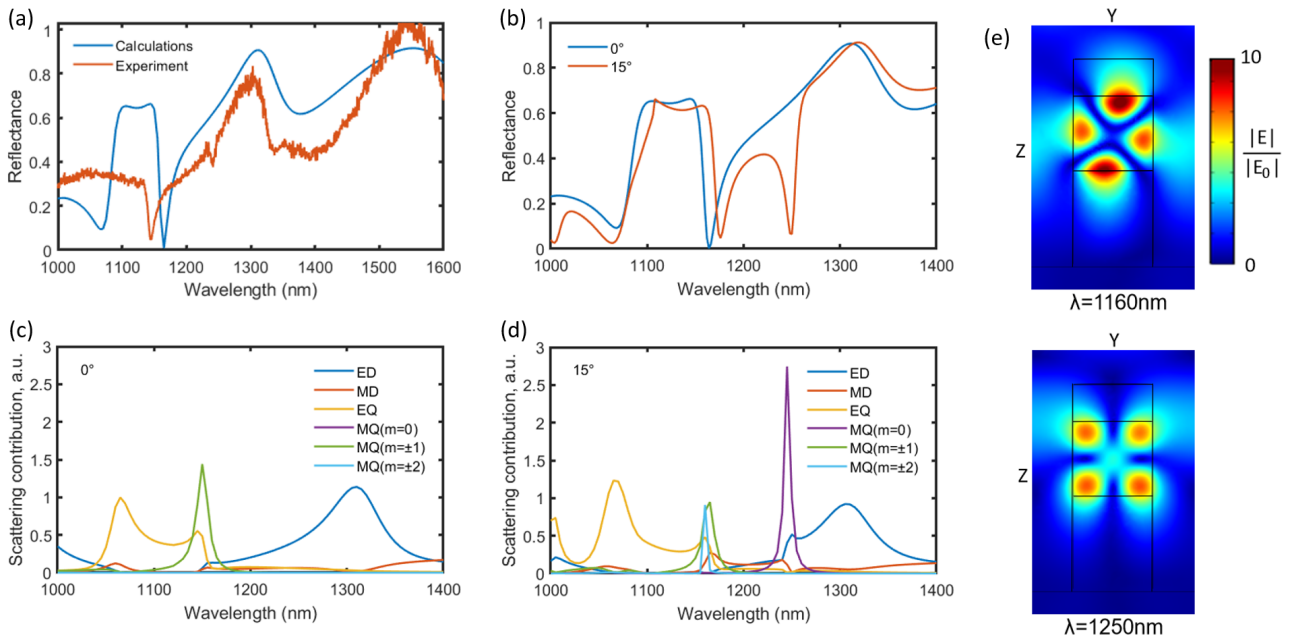

Figure 5.10: (a) Calculated and experimental normal-incidence reflectance spectra from a sample with measured nanocylinder diameter of 440 nm and period of 880 nm. (b) Calculated reflectance spectra for plane wave incidence at 0° or 15°. (c,d) Multipole decomposition of the modes excited in the GaAs nanocylinders by a TE-polarized plane wave incident (c) at 0° and (d) at 15°. The plane of the incidence is the $y-z$-plane. (e) Calculated electric field distribution at an $x-y$-plane through the center of the GaAs nanocylinder at the wavelengths of 1160 nm (top) and 1250 nm (bottom) wavelength for excitation by a TE-polarized plane wave incident at 15°.

In order to explain the observed narrow dips, we numerically investigate the modes excited in the GaAs nanocylinders. In the numerical calculations, the refractive index of GaAs was taken from [160], the refractive index of the pedestal was 1.6 and the refractive index of the cap was 1.45. The design values were used for all geometrical structure parameters, merely the nanocylinder diameter was allowed to vary within the accuracy limits of the nanofabrication procedure in order to globally optimize the agreement between experimental and numerical data over all resonances and all the different measurement configurations considered in this work. The best overall agreement was reached for a nanocylinder diameter of 425 nm, slightly smaller than the value observed in SEM images. A comparison of numerically calculated and experimentally measured near-normal-incidence reflectance spectra is shown in Figure 5.10 (a). A good overall agreement is obtained, however, one narrow dip appears slightly red-shifted in the calculated reflectance spectrum. Furthermore, the second small dip observed in the experimental spectra at around 1242 nm wavelength is not reproduced in the calculated spectra, which we attribute to the deviations from normal incidence excitation in the experiment. In order to study the effect of the finite numerical aperture used in the experiment on the reflectance spectra, we calculate the reflectance spectrum of the structure for a TE-polarized plane wave incident at 15°. We limit the spectral range to the wavelengths, where the dips are expected. These results are depicted in Figure 5.10 (b). For comparison, the corresponding normal-incidence spectrum is also included in the figure. Clearly, an additional narrow dip occurs at around 1250 nm for the oblique-incidence case. Next, to analyze the multipolar order of the observed resonance features, we performed a multipole decomposition. Note

that in the multipole decomposition calculations we took the integrals in Equation (3.12) and Equation (3.13) only over the GaAs nanocylinder. The results are shown in Figure 5.10 (c,d) for normal-incidence and 15°-incidence excitation, respectively. Figure Figure 5.10 (d) allows us to identify both resonances appearing as the narrow dips in the experimentally measured reflectance shown in Figure 5.10 (a) as MQ resonances. These modes correspond to associated Legendre polynomials $P_l^m(x)$ of the same ($l = 2$) degree, but having different order of $m = \pm 1$ at 1150 nm and $m = 0$ at 1250 nm (see Chapter 2). At normal incidence (see Figure 5.10 (c)), in contrast, we can only excite one resonance at around 1150 nm, while the other resonance is symmetry-forbidden (see Figure 5.10 (d)). Figure 5.10 (e) furthermore shows the calculated electric field distribution of the two modes excited in nanocylinders by a TE-polarized plane wave incident onto the structure at 15°. As expected, the modes show electric field profiles characteristic for quadrupolar Mie-type resonances (see Figure 2.4).

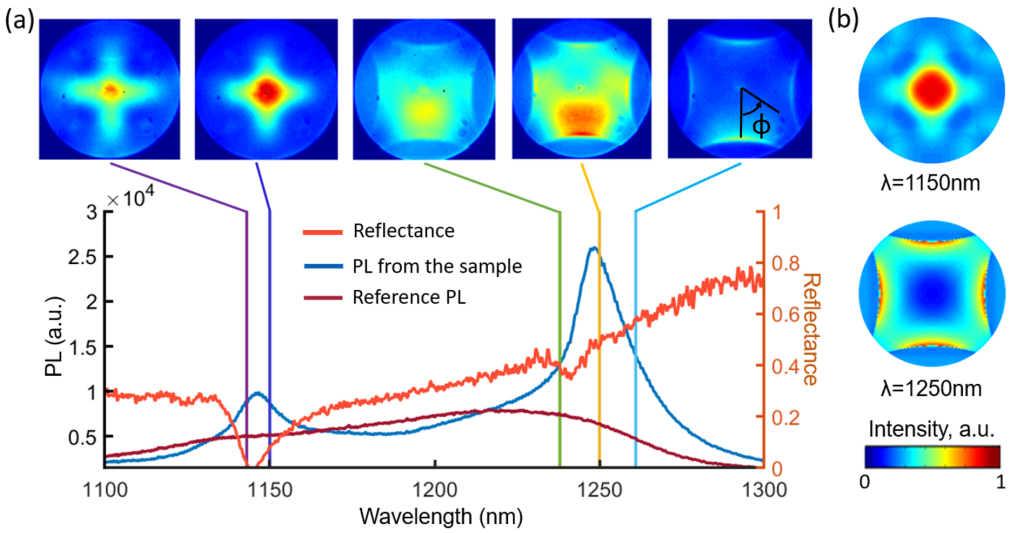

Figure 5.11: (a) Experimentally measured PL spectra for the metasurface sample with nanocylinder diameter of $D = 440$ nm and unpatterned area for the reference. The images on top of the figure show the experimentally measured BFP images measured through the bandpass filters with FWHM of 10 nm and the center wavelength corresponding to the vertical color lines. The NA of the collection objective is 0.6. (b) Calculated BFP images for the wavelengths of 1150 nm and 1250 nm.

Next, we measure the PL spectrum and BFP images of the current metasurface with a 0.6NA collection objective. These results are presented in Figure 5.11 (a). As a reference, we measured the PL spectrum from the unpatterned area of the wafer. The unpatterned areas of the wafer are hundreds of microns in transverse dimensions and were protected from the ICP etch by a resist mask. Most prominently, the PL spectrum from the metasurface shows two pronounced peaks appearing at 1150 nm and 1250 nm, which coincide with the spectral positions of the magnetic quadrupole resonances of the structure. To show this correspondence directly, we have included the experimental reflectance spectrum of the sample in the figure, showing that the peaks in the PL spectrum and the minima in the reflectance spectrum occur at approximately the same spectral positions. Taking into account the reduction of the amount of active material (filling factor: 20%) for the nanocylinder metasurface with respect to the unstructured wafer, we calculate a brightness enhancement of 19 at a wavelength of 1250 nm.

We refrain from estimating the quality factor of the quadrupolar resonances based on the PL spectrum, since, as it will be shown below by momentum-resolved spectroscopy, the width of the peaks in the PL spectrum is dependent on the NA of the collection objective.

The upper part of the Figure 5.11 (a) illustrates the experimental BFP images. The center wavelength (1143 nm, 1150 nm, 1237 nm, 1250 nm, or 1260 nm) of the BP filter used to take each of these images is indicated by a vertical colored line. We can clearly see the reshaping of the angular distribution of the emission. The emission patterns exhibit fourfold symmetry as a direct consequence of the metasurface symmetry. The BFP images corresponding to the low-wavelength $m = \pm 1$ MQ resonance exhibit the intensity maximum at the center, corresponding to QD emission with a small angular spread at normal direction out of the sample plane. Such reshaping can be useful for the optical systems with low-NA collection optics, since 25% of the photons are emitted within the solid angle of 0.1 NA, compared to less than 1% photons that are collected for the case of a homogeneous emission pattern. In contrast, the BFP images of the emission at the high-wavelength $m = 0$ MQ resonance show the minimum in the center. As it was mention above, the high-wavelength resonance cannot be excited by a plane wave incident normally, by reciprocity, which means no emission along the same direction which agrees well with the experiment. We also note that the BFP images show an obvious asymmetry, which is likely due to sample imperfections such as a slight tilt of the nanocylinders as discussed in Löchner et al. [161] for nonlinear emission from similar samples.

To compare our experimental results with theory, we numerically calculated the angle-resolved emission using the FMM in combination with the reciprocity principle (see Section 3.1.2). A TE or TM plane wave was incident from the air semi-space onto the metasurface. The polar angle of incidence θ was varied from 0° to 37° corresponding to the NA of the collection optics and the azimuthal angle of incidence ϕ was varied from 0° to 45° due to the four-fold and mirror symmetries of the metasurfaces. We added a small imaginary part to the refractive index of the nanocylinder material (GaAs), while other materials of the metasurface were lossless within a considered wavelength range. This allowed us to match the calculated angle-resolved absorption (summed up for both TE and TM polarization of the excitation plane wave) with far-field emission from the QDs integrated into the nanocylinder. Note that rigorous simulation of 5 layers of QDs inside the nanocylinders shows almost identical results for exemplary test cases while being more computational-intensive. The calculated BFP images at 1150 nm and 1250 nm wavelength are shown in Figure 5.11 (b), showing a good overall agreement with the experimentally measured images apart from the already discussed asymmetry of the experimental images for the $m = 0$ MQ resonance. In particular, the maximum/minimum of emission in (near) normal direction for the $m = \pm 1/m = 0$ MQ modes, respectively, is well reproduced.

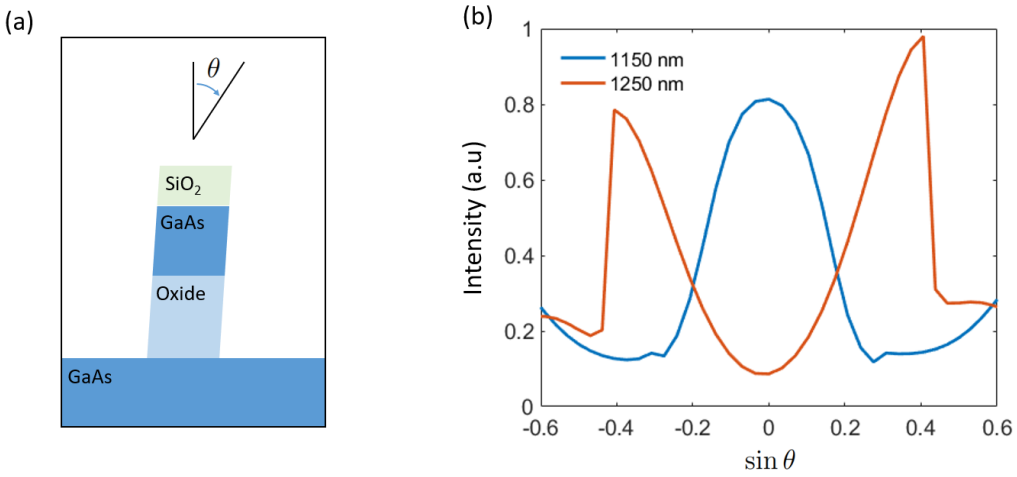

Figure 5.12: (a) Illustration of the unit cell used in calculations. The axis of the nanocylinder is tilted by 2°. (b) Calculated cross-section of the BFP image at 1150 nm and 1250 nm wavelength for the metasurface consisting of tilted nanocylinedr.

To confirm that the asymmetry in the experimental BFP images is caused by the sample imperfections, we simulated a metasurface composed of nanocylinders that are tilted by 2° [161]. Since the computational domain can no longer be effectively divided into layers that are uniform along the z-axis, as needed for efficient FMM calculations, we used the COMSOL package in combination with the reciprocity principle for these simulations. Figure 5.12 (a) shows a sketch of the unit cell used in our simulations. The axis of the cylinder was tilted by $\theta = 2°$. A TE or TM plane wave was incident from the air semi-space onto the metasurface. The polar angle of incidence θ was varied from 0° to 37° corresponding to the NA of the collection optics and the azimuthal angle of incidence ϕ was fixed to 0°. Therefore, the wavevector of the incident plane wave stays in the plane of the Figure 5.12 (a). Figure 5.12 (b) shows the calculated intensity distribution over the vertical cross-section through the center of BFP images at 1150 nm and 1250 nm wavelength (see Figure 5.11). We observe a pronounced asymmetry of the BFP image of $m = \pm 1$ MQ mode at 1250 nm, while the $m = \pm 1$ MQ mode at 1150 nm appears fairly symmetric as in the experiment.

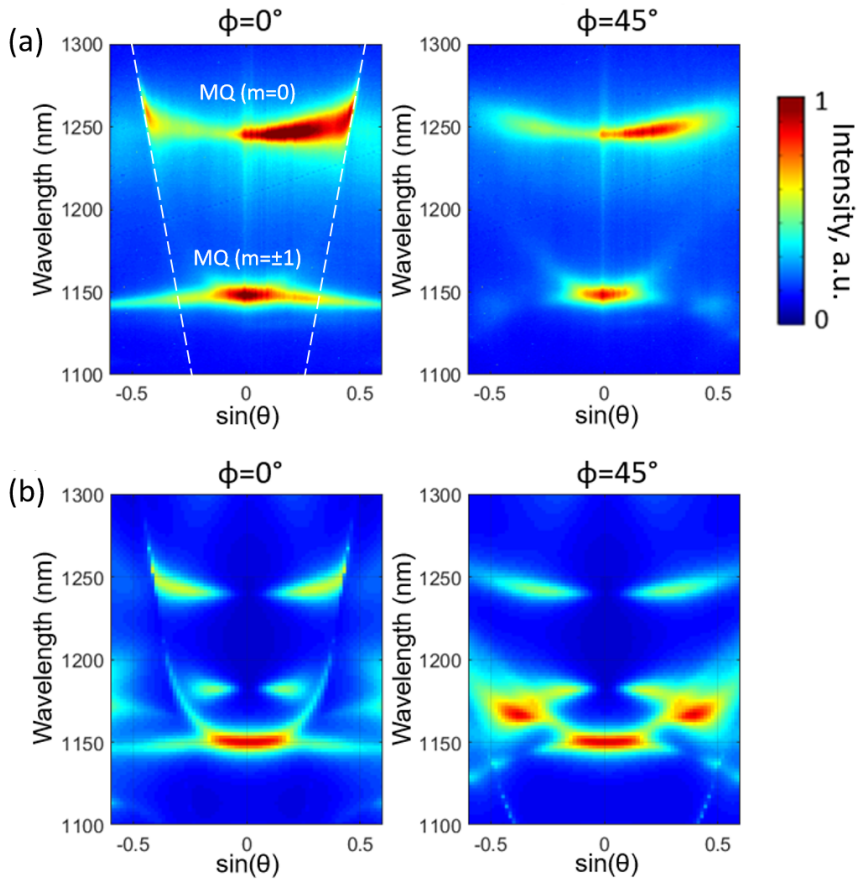

Figure 5.13: (a) Momentum-resolved emission spectra of the GaAs metasurface sample with nanocylinder diameter of $D = 440\,\text{nm}$ and period of $P = 880\,\text{nm}$. The spectrometer slit is oriented along one of the lattice vectors ($\phi = 0°$) of the nanocylinder array and along the diagonal of the unit cell ($\phi = 45°$), respectively. (b) Corresponding numerically calculated momentum-resolved spectra.

In order to investigate how the angular emission distribution is affected by the periodic arrangement of the resonators at different wavelengths, we furthermore performed momentum-resolved spectroscopy measurements for two experimental configurations. In the first case, one of the lattice vectors of the nanocylinder array is oriented parallel to the entrance slit of the imaging spectrograph ($\phi = 0°$). In the second case, the sample is rotated around its normal by $\phi = 45°$. The experimental data is presented in Figure 5.13 (a) and yields two different cross-sections of the GaAs metasurface band structure in $(\sin(\theta), \text{wavelength})$ coordinates, where θ is the polar angle at which the emission is propagating with respect to the metasurface normal. The BFP images shown in Figure 5.11, in contrast, represent isofrequency slices of the band structure. For both configurations we observe the emission signatures of the two MQ resonances of the GaAs nanocylinders at 1150 nm and 1250 nm wavelength. The Mie-resonances show a flat dispersion, i.e. their spectral position is only weakly dependent on the angle of emission. In addition, for the case of the $\phi = 0°$, we notice the highly dispersive modes shown by the dashed lines. These modes are the lattice modes, when the light scattered by the GaAs nanocylinders interferes constructively along the metasurface plane. Interestingly, the MQ resonance at around 1250 nm is strongly suppressed at angles θ beyond these lattice resonances, which can be explained by the interaction between the scatterers in the 2D periodic array (see Section 2.3).

To allow for comparison of our experimental results with theoretical predictions, we numerically calculated the momentum-resolved emission spectra of the GaAs nanocylinder arrays using the same method as for the calculation of the BFP images of Figure 5.11 (b). Specifically, we calculated the absorption spectra of a plane wave for a systematic variation of the angle of incidence within the angular range from $\theta = 0°$ to $\theta = 37°$, corresponding to the collection NA used in the experiment and azimuthal angle took values of $\phi = 0°$ or $\phi = 45°$. The results are shown in Figure 5.13 (b). One can note a good overall agreement with experimental data. Indeed, we can identify all the essential features observed also in the experimental momentum-resolved emission spectra, including the MQ resonance positions at 1150 nm and 1250 nm wavelength, the features associated with the lattice modes, and the hybridization between the particle resonances and the lattice modes.

However, some deviations between the experimental and numerical results are also apparent. On the one hand, additional modes appear in the calculations between 1150 nm and 1250 nm, which are not observed experimentally. The fact that they are not detected in the experiment may be attributed to a high sensitivity of these modes to sample imperfections as well as to the limited dynamic range of the employed InGaAs camera. On the other hand, the experimental momentum-resolved emission spectra exhibit clear deviations from perfect symmetry. As already discussed in the context of the experimental BFP images, the observed asymmetries can be explained by a slight tilt of the nanocylinders.

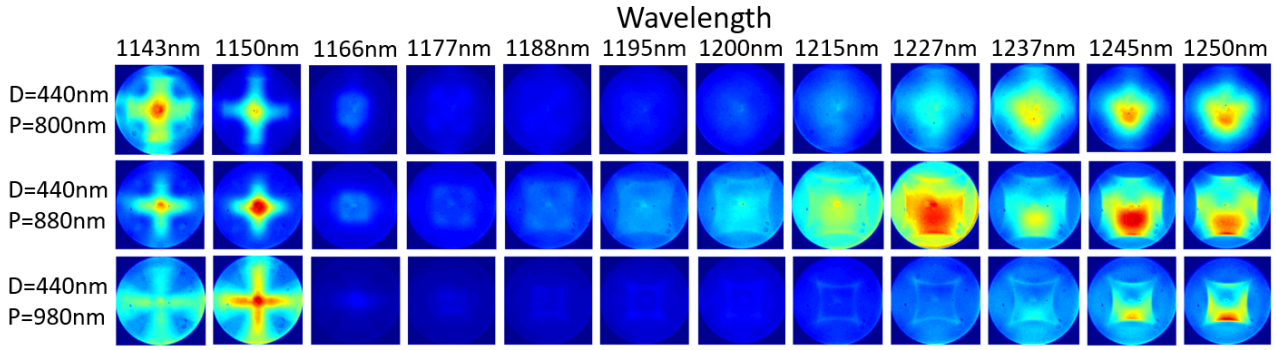

Figure 5.14: BFP images of the emission from the metasurfaces with specified diameter D and period P, measured by 0.6NA objective through a BP filter with 10 nm FWHM and specified center wavelength.

Finally, to investigate the influence of the lattice period on the spatial emission characteristics for both MQ modes, we recorded the experimental BFP images of the GaAs nanocylinders metasurfaces for three different lattice periods ($P = 800$ nm, $P = 880$ nm and $P = 980$ nm). The results are shown in Figure 5.14. Each row of images corresponds to the sample dimensions specified in the title column. Each column corresponds to a particular central wavelength of the passband specified on the top. Specifically, we used three different BP filters form Thorlabs: FB1150-10, FB1200-10 and FB1250-10. The numbers in the filters' model names stand for the central wavelength of the passband and the FWHM. Since the filters are interferometric, the central wavelength of the passband can be reduced by tilting the filter with respect to the optical axis. We made use of this effect to shift the central wavelength by gradually tilting the filters in 5° steps within the 0° to 25° range. Clearly the patterns of light emitted into the out-of-plane MD mode are reshaped as a function of wavelength. As mentioned above,

the BFP images are determined by the respective Mie- and lattice modes as well as their interplay. While the properties of the Mie-resonances are mainly governed by the dimensions of the nanoresonators, the lattice modes can be independently tailored by the lattice period. To illustrate this effect, we plot the selected BFP images at 1150 nm and 1250 nm wavelength with the corresponding isofrequency contours of the dispersion of the lattice modes in 2D array of scatterers with a surrounding refractive index of 1 and observe a strong dependence on the period in Figure 5.15. Clearly, the underlying features apparent in the BFP images are well reproduced by the isofrequency contours. The details on the calculations of the isofrequency contours can be found in the Section 5.1. The manipulation of the lattice modes allows for squeezing the emission into a narrow single lobe: for example, we observe the clear reduction in the solid angle into which the PL is emitted for the case of the MQ resonance excited at the wavelength of 1250 nm for an increase of the period from 880 nm to 980 nm.

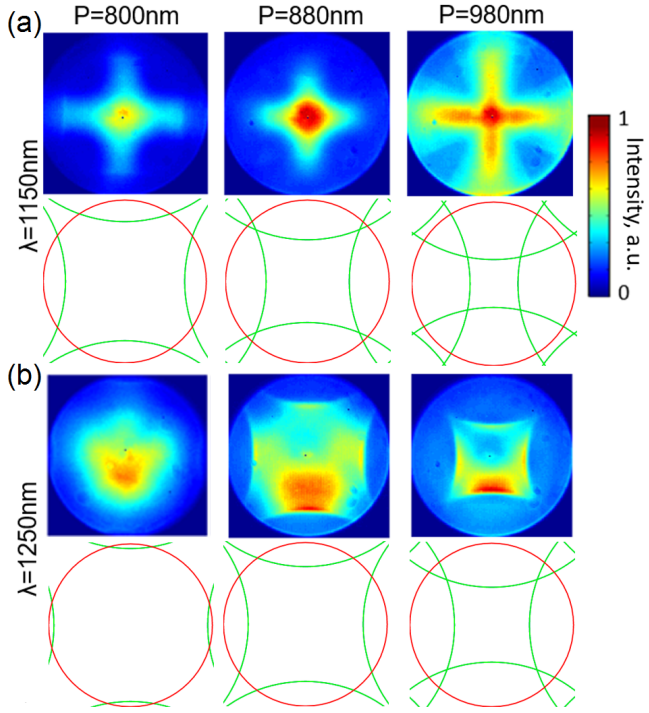

Figure 5.15: Top row: BFP images of the PL emission from the GaAs metasurface samples with nanocylinder diameter of $D = 440$ nm and different periods varied from $P = 800$ nm to $P = 980$ nm, measured through bandpass filters with FWHM of 10 nm and center wavelengths of 1250 nm. Bottom row: corresponding lattice mode dispersion in the reciprocal space (green). The radius of the red circle defined by the NA of the collection objective and equals to k_0NA, where NA=0.6. (b) Top row: BFP images of the PL emission from the same metasurfaces measured through the bandpass filters with FWHM of 10 nm and center wavelengths of 1150 nm. Bottom row: corresponding lattice mode dispersion in the reciprocal space (green). The radius of the red circle defined by the NA of the collection objective and equals to NAk_0, where NA=0.6.

5.3 Strong photoluminescence signal enhancement by broken-symmetry metasurface

5.3.1 Motivation

In the previous sections, we demonstrated the directional and spectral shaping of the PL emission by Mie-resonant dielectric metasurfaces. We achieved a comprehensive control over the emission pattern via tailoring the "array factor" and scattering properties of the individual elements. However, the enhancement of the PL signal from the investigated metasurfaces showed moderate values, that are consistent with the low Q-factor of the Mie-modes of the nanocylinders composing the metasurface. In order to reach higher values of the PL signal enhancement, we need to engineer a metasurface that supports more complex high-Q modes offering important opportunities for stronger enhancement.

The arrays of plasmonic nanoparticles supporting collective resonances have been extensively studied in recent years due to their significant field enhancements [100]. These resonances originate from the hybridization between the lattice and localized resonances in the individual nanoparticles and feature high Q-factors and low radiative losses. The high Q-factor of collective resonances has been the reason for proposing them in applications, such as sensing [162], solid state lighting [76], and lasing [112, 141, 163–165]. Similar to single nanoparticles, hybrid modes in the arrays of dielectric nanoresonators represent a promising alternative to the plasmonic arrays [166].

Here we demonstrate the high-Q hybrid modes in the metasurfaces composed of Mie-resonant broken-symmetry dielectric nanoparticles with monolithically integrated self-assembled InAs QDs. The coupling of the QD emission into these modes results in PL signal enhancement by 2 orders and directional reshaping of the far-field emission. Our all-dielectric approach offers a low-loss platform that does not cause an unnecessary loss in total QY.

5.3.2 Experimental characterization

In the Section 2.3.2 we discussed the hybridization of the localized out-of-plane dipole Mie-modes with collective lattice oscillations leading to the appearance of a high-Q mode. The free-space coupling of this hybrid mode can be manipulated by reducing the symmetry of the resonators. In order to exploit this mode for PL enhancement, we integrated InAs QDs into broken-symmetry dielectric metasurfaces composed of GaAs resonators where one of the corners was removed. An SEM image of the broken-symmetry metasurfaces is shown in Figure 5.16 (a). The fabrication was done in accordance with the steps described in Section 4.1. Such resonators allow for coupling to the out-of-plane dipole mode by normal incidence and by any polarization of the incident light field. Therefore, by reciprocity, we expect emission in the direction perpendicular to the metasurface plane, allowing for an enhanced collection efficiency in standard microscopic setups. The scheme of the broken-symmetry metasurfaces is illustrated in the inset of Figure 5.16 (b). The GaAs resonators incorporate a single layer of InAs QDs and are situated on a GaAs substrate and a low-index pedestal. The corresponding calculated normal-incidence

reflectance spectrum is shown in Figure 5.16 (b). We observe two sharp dips appearing due to the excitation of the high-Q resonances. Figure 5.16 (c) shows the electric field distributions at the resonant wavelengths in the $x - y$ cross-section through the center of a resonator excited by a plane wave incident along z-axis. Additionally, we show the electric field vector directions by white arrows in the same figure. The circulation of the electric field at the higher resonance wavelength allows us to identify the mode as the out-of-plane ($m = 0$) MD mode, while the electric field maximum in the center with a dominant z-component indicates the excitation of the out-of-plane ED mode at the lower resonance wavelength.

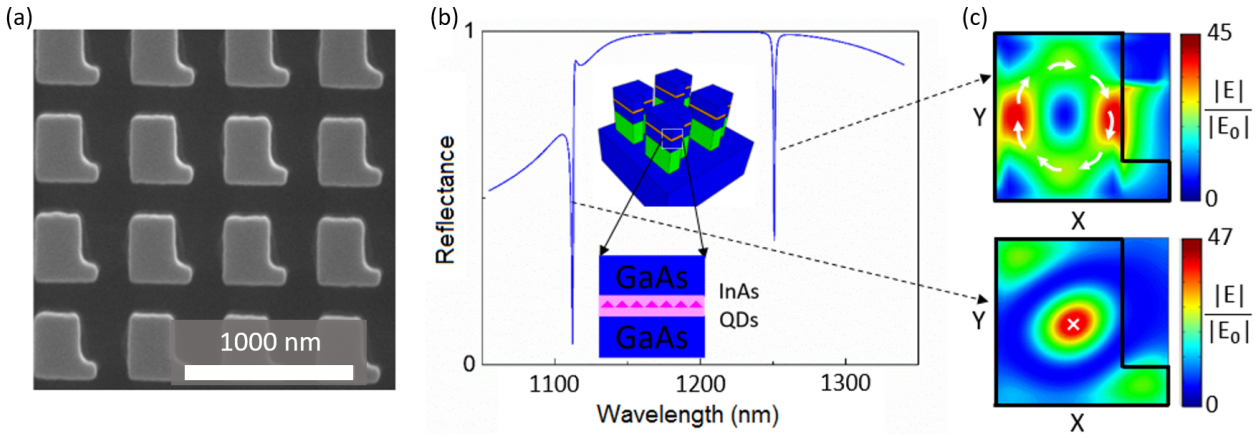

Figure 5.16: (a) Top-view SEM of a broken-symmetry GaAs metasurface sample incorporating 1 layer of InAs QDs. The scale bar corresponds to 1000 nm. (b) Numerically calculated normal-incidence reflectance spectrum of the symmetry-broken metasurface. The inset shows a sketch of the metasurface geometry: the period is 610 nm, the GaAs resonator height is 400 nm, the side length of the nanoresonator is 345 nm, the notch dimensions are 90 nm by 240 nm. (c) Calculated electric field profiles corresponding to the two high-Q resonant modes responsible for the sharp dips observed in (b). The solid black lines show the boundaries of the resonators. Reprinted with permission from [111]. Copyright (2018) American Chemical Society. The calculations were performed by Sheng Liu.

The PL spectra of the broken-symmetry metasurfaces were measured using a home-built PL spectroscopy setup. A pulsed laser with a temporal width of 120 fs, a wavelength of 750 nm and a repetition rate of 80 MHz was used for excitation. The laser beam was focused onto the sample and the PL emission was collected by an 0.4NA objective (Mitutoyo M Plan Apo 20×). The PL emission was subsequently coupled to a NIR spectrometer with liquid nitrogen cooled InGaAs detector. An example of a PL spectrum measured from one of the metasurfaces is shown in Figure 5.17 (a), alongside with the reference PL spectrum measured from an unpatterned area of the QD containing wafer. Taking the reduction of the luminescent material due to the 0.38 filling fraction of the resonators into account, the PL spectrum from the metasurface shows a 290-fold enhancement of the PL peak signal. In Figure 5.17 (b) we depict the measured PL and normal-incidence reflectance spectra (see Section 4.2 for detail on reflectance measurements) for three different broken-symmetry metasurfaces with gradually scaled transverse dimensions of the resonators. Scaling factor S_1 corresponds to side length of the nanoresonator of 320 nm, S_2 to 330 nm and S_3 to 340 nm. The period, height and notch dimensions are the same for all three metasurfaces. The scaling allows to spectrally shift the resonances. The peaks in the PL spectra coincide with the higher-wavelength dips in the reflectance spectra associated with

the out-of-plane MD resonances. Interestingly, the measured and calculated reflectance spectra show additional out-of-plane ED resonance at shorter wavelengths. However, the PL signal enhancement at this resonance is not enhanced significantly. Likely, the sample imperfections suppress this type of resonance. Note that the mentioned parameters of the broken-symmetry metasurfaces were identified as follows: the height of the nanoresonators and the period were taken from the fabrication parameters. The other dimensions of the nanoresonators were varied to optimize the agreement between the experimental and measured reflectance data for each metasurface.

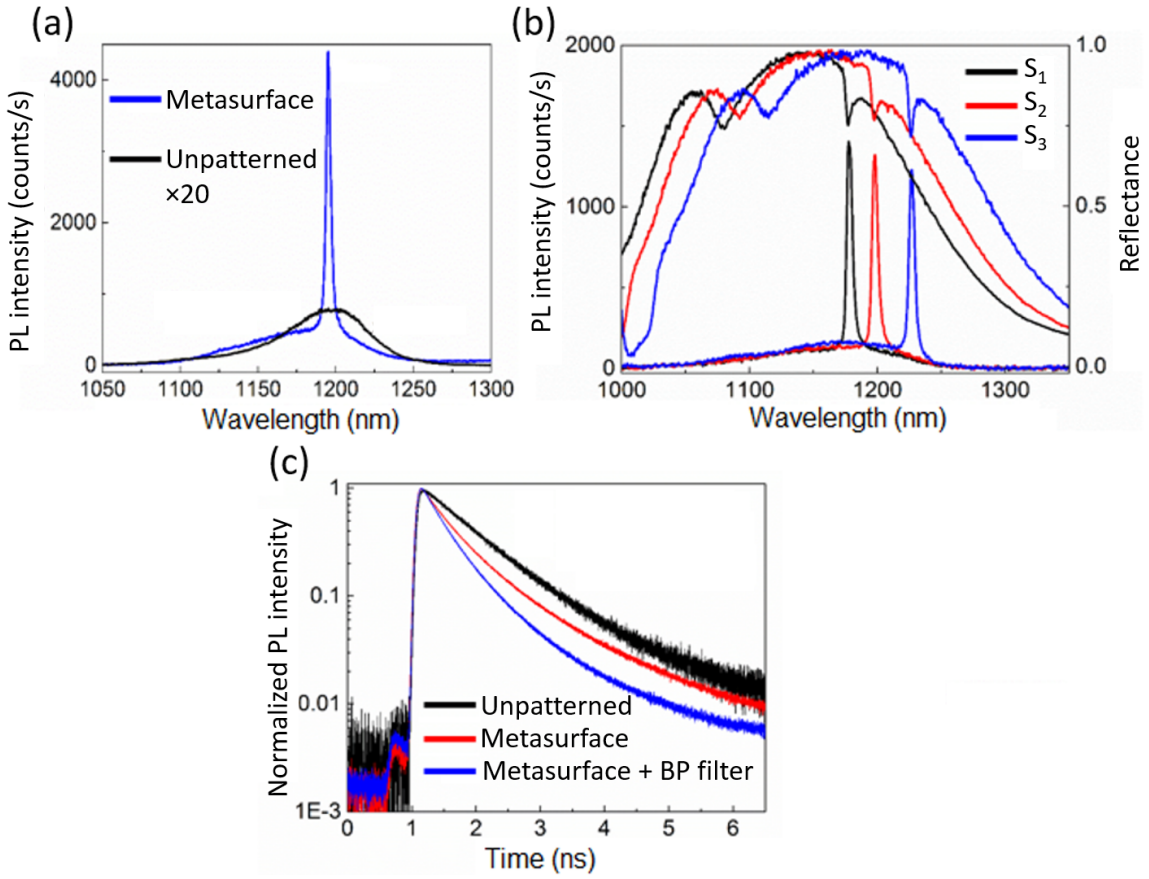

Figure 5.17: (a) Experimentally measured PL spectra for the symmetry-broken metasurface (blue) and for the unpatterned area (Black). The dimensions of the symmetry-broken metasurface are following: the period is 610 nm, the GaAs resonator height is 400 nm, the side length of the nanoresonator is 330 nm, the notch dimensions are 90 nm by 235 nm. (b) Experimentally measured normal-incidence reflectance and corresponding PL spectra for three symmetry-broken metasurface samples with gradually increasing scaling factors (S). Scaling factor S_1 corresponds to side length of the nanoresonator of 320 nm, S_2 to 330 nm and S_3 to 340 nm. The period, height and notch dimensions are the same for all three metasurfaces. (c) Experimentally measured time-resolved low-temperature PL of a sample exhibiting the out-of-plane dipole resonance at 1100 nm. The dimensions of the symmetry-broken metasurface sample are following: the period is 580 nm, the GaAs resonator height is 400 nm, the side length of the nanoresonator is 305 nm, the notch dimensions are 90 nm by 210 nm. This metasurface is chosen, because the InAs PL peak blue shifts to 1110 nm at the temperature of 4 K. The red curve corresponds to the signal integrated over the whole spectral range of emission from the metasurface, the blue curve shows data collected using a BP filter (10 nm FWHM, 1100 nm center wavelength), the black curve shows data from the unpatterned area for reference. Reprinted with permission from [111]. Copyright (2018) American Chemical Society. (a,b) Measurements performed by Sheng Liu. (c) Measurements performed by Xiaowei He and Younghee Kim.

High-Q modes provide an enhanced LDOS increasing the radiative decay rate (see Section 2.4.2). To investigate this effect, we measured time-resolved PL from the symmetry-broken metasurface cooled down to 4 K. The low-temperature measurements were required to extend the intrinsic lifetime of the QD PL to 1 ns, such that a liquid Helium cooled superconducting nanowire detector was able to resolve it. In Figure 5.17 (c) we show the decay curves of the PL from the broken-symmetry metasurface and unpatterned area. The peak of the InAs QDs PL was blue-shifted from 1200 nm at room temperature to 1110 nm at 4 K. Therefore, we chose a metasurface with smaller scaling factor, exhibiting the out-of-plane MD resonance at the wavelength of 1100 nm. The dimensions of this symmetry-broken metasurface are following: the period is 580 nm, the GaAs resonator height is 400 nm, the side length of the nanoresonator is 305 nm, the notch dimensions are 90 nm by 210 nm. We observe a pronounced lifetime reduction of the PL collected from the metasurface. Even further reduction by a factor of 2 in lifetime was observed when the PL was probed thought a BP filter with a 10 nm-wide passband centered at the wavelength of the out-of-plane MD resonance of the metasurface.

Even though we observe a significant PL lifetime reduction, this effect is not sufficiently high to explain the PL signal enhancement factor of 290. Likely, the extraction and collection efficiency enhancement also have a strong contribution to the Pl signal enhancement. We performed the simulations with point electric dipole as a source (see Sections 3.1.1 and 3.3) to estimate the percentage of photons emitted in the air semi-space from the unpatterned wafer used as a reference. Since the QDs were embedded into a high-index slab, only around 3% of photons were emitted in the air semi-space. In contrast, similar simulations for the finite array of broken-symmetry resonators showed that almost 50% of the photons can be emitted into the air semi-space. Due to the 500 nm low-index pedestal the emission from QDs does not effectively couple to the guided modes of the GaAs substrate and the emission into the air semi-space is not suppressed.

5.3.3 Directionality of the emission from broken-symmetry metasurfaces

We now focus our attention on the far-field directionality of the PL emission from the broken-symmetry metasurfaces. We used the BFP setup described in Section 4.3 with an 0.6NA objective to map the angle-resolved far-field PL emission. In Figure 5.18 (a)-(c) we depict the recorded BFP images of the PL emission from the broken-symmetry metasurface corresponding to the spectrum shown in Figure 5.17 (a). To probe the emission directionality at three different wavelengths, we used an interferometric BP filter (Thorlabs FB1200-10) with an FWHM of 10 nm. We tilted the filter by 0°, 5° and 10° to vary the center wavelength of the passband. Clearly the pattern of light emitted into the out-of-plane MD mode is reshaped as a function of wavelength. At a wavelength of 1177 nm, the PL emission is squeezed into a narrow lobe perpendicular to the metasurface plane. At 1188 nm wavelength, the emission pattern forms a rhombus in the momentum space, which becomes larger at a wavelength of 1200 nm.

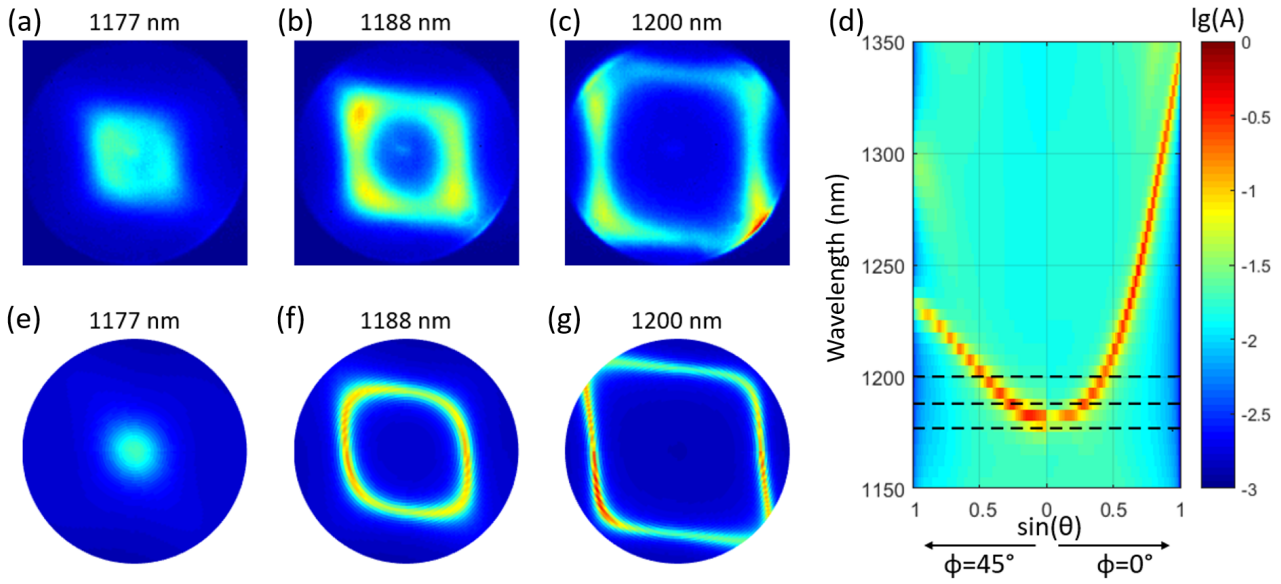

Figure 5.18: (a)-(c) Experimentally measured BFP images of the PL emission from the symmetry-broken metasurface S_2 (see Figure 5.17 (a,b)) collected by an 0.6NA objective for three different 10 nm-wide passbands centered at 1177 nm, 1188 nm and 1200 nm. (d) Calculated angle-dependent absorption (A) spectra of the same symmetry-broken metasurface for a TE-polarized excitation plane wave. The dashed lines illustrate the isofrequency slices represented in the BFP images. (e)-(g) Calculated BFP images corresponding to the experimental images shown in (a)-(c). Reprinted with permission from [111]. Copyright (2018) American Chemical Society.

To understand the physics behind the observed behavior of the far-field PL emission, we performed numerical simulations of the absorption spectra for the broken-symmetry metasurface excited by a TE-polarized plane wave with variant incidence direction (θ, ϕ). The TE polarization is selected to effectively excite the out-of-plane MD mode (see Section 2.3.2). As discussed in the previous chapter, the absorption enhancement is reciprocal to the emission enhancement. The dimensions of the nanoresonators used in these calculations were the same as for the scaling factor S_2. The refractive index data of GaAs was taken from Skauli et al. [160]. The refractive index of the oxide pedestal was fixed to 1.6. Note that none of the materials shows significant absorption in the considered spectral range. Instead of simulating the actual InAs QDs layer inside the GaAs nanocylinder, we introduced a low artificial loss factor of $0.0031i$ to the refractive index of the entire GaAs nanocylinder. This allowed us to reduce the number of layers in the computation domain by 2 and significantly accelerate the FMM calculations. We verified that the results of such simulations show no notable difference as compared to the simulations of the rigorous layered structure. The calculated absorption spectra are shown in Figure 5.18 (d). The red region corresponds to the absorption enhanced by the out-of-plane MD mode. This mode shows a strong U-shaped dispersion. Furthermore, we performed single wavelength angular-resolved absorption calculations to reproduce the measured BFP images. To obtain the results comparable with the experiment, we considered both TE and TM polarizations of the incident plane wave. The polar angle of incidence θ was varied from 0° to 38° corresponding to the NA of the collection optics and the azimuthal angle of incidence ϕ was varied from 0° to 180°. Figure 5.18 (e)-(g) shows the calculated BFP images for the wavelengths of 1177 nm, 1188 nm and 1200 nm, respectively. We observe a good overall

agreement with the measured BFP images. Each of the calculated BFP images corresponds to one of the isofrequency slices depicted in Figure 5.18 (d) by the dashed lines.

The curvature of the out-of-plane MD mode dispersion can be controlled by adjusting the period of the broken-symmetry metasurface. To demonstrate this effect, we calculated the angular-dependent absorption spectra of three different symmetry-broken metasurfaces excited by a TE-polarized plane wave (see Figure 5.19). All three symmetry-broken metasurfaces are composed of identical nanoresonators, with dimensions corresponding to S_2, and only differed in their period, namely $P = 510\,\text{nm}$, $P = 710\,\text{nm}$ and $P = 910\,\text{nm}$. The variation in period allowed for tailoring the lattice modes, and therefore, affected the hybrid mode dispersion. For the period of 510 we achieved a relatively flat dispersion, whose curvature is gradually increasing with increasing period. The control over the directionality of the PL emission offered by this possibility to engineer the dispersion allows for adjusting the emission characteristics of the metasurface to a particular application. For example, the light from a typical light-emitting device (LED) with a 100 nm wide spectrum can be emitted in all directions for illumination purposes ($P = 510\,\text{nm}$) or squeezed into a narrow lobe with a beamwidth of around 60° ($P = 910\,\text{nm}$) for enhanced collection efficiency or beaming.

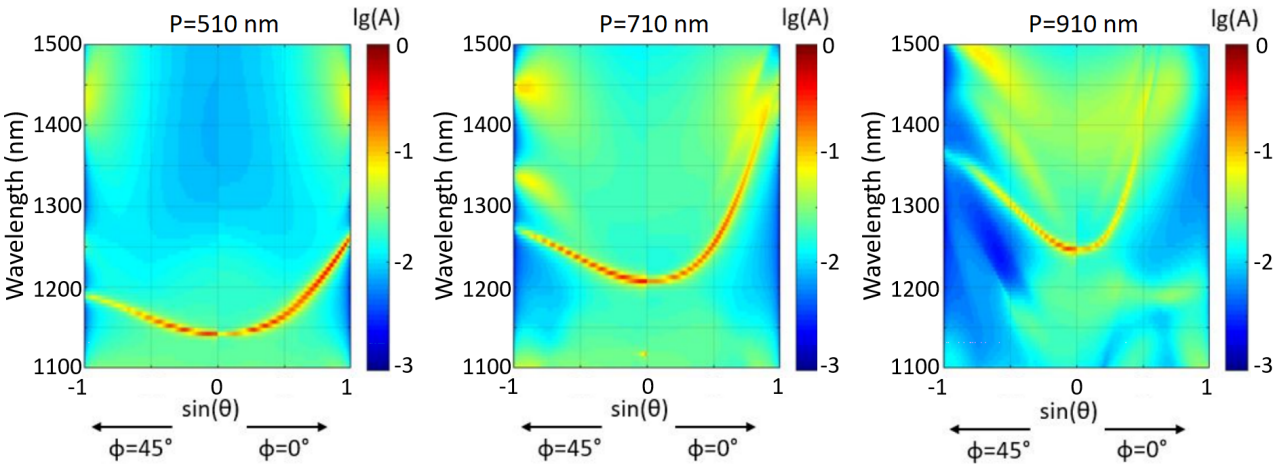

Figure 5.19: Calculated angle-resolved absorption spectra of symmetry-broken metasurfaces with different periods P. Reprinted with permission from [111]. Copyright (2018) American Chemical Society.

5.4 Manipulation of magnetic dipole emission from Eu^{3+} with silicon nanocylinder arrays

5.4.1 Motivation

So far, we investigated the light-emitting systems, in which the emission originates from the electronic transitions mediated by the electric dipole term of the interaction Hamiltonian (see Section 2.4.1). This is due to the fact that the interaction of matter with the electric field of light is usually several orders of magnitude stronger as compared to the interaction of matter with the magnetic field of light [113, 115]. An important exception, however, is exemplified by trivalent lanthanide ions, such as Eu^{3+}, which is well known to exhibit magnetic dipole transitions in the visible spectral region [115, 119, 137, 167, 168]. A sketch of the electronic energy-level structure of the Eu^{3+} is shown in Figure 5.20 (a) for the emission transitions between the states $^5D_0$ and ^7F_n. The absorption spectrum of the Eu^{3+} peaks in the ultraviolet range [169]. The emission spectrum of the polystyrene layer doped by Eu^{3+} containing complex $Eu(TTA)_3L18$, which we used in our work, is depicted in Figure 5.20 (b). It exhibits several emission lines in the visible range, all of them corresponding to electronic transition from the same excited state $^5D_0$ to one of the lower energy states ^7F_n. In particular, the emission line centered at wavelength of 590 nm is dominated by the magnetic dipole transition $^5D_0 \rightarrow ^7F_1$, while the other lines originate from the electric dipole transitions [137, 170].

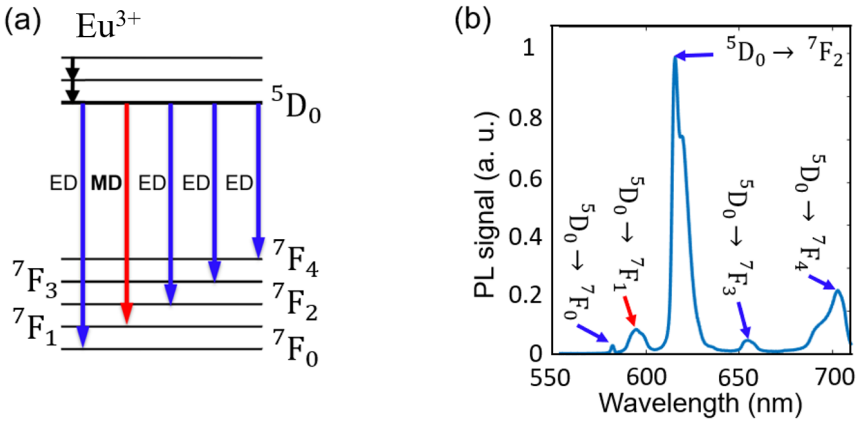

Figure 5.20: (a) Schematic of the electronic energy-level structure of Eu^{3+}. (b) Measured emission spectrum from a polystyrene layer doped by Eu^{3+} containing complex $Eu(TTA)_3L18$ and spin coated onto a bare glass substrate. Reprinted with permission from [171]. Copyright (2019) American Chemical Society.

As we discussed in the Section 2.4.1, the photonic environment, i.e. the LDOS, has a crucial influence on spontaneous emission via electric and magnetic dipole transitions. The proper engineering of the photonic environment can dramatically influence the selectivity between the electric and magnetic emission channels. In that respect, metasurfaces offer unique opportunities for the design of the electric and magnetic LDOS and hence for selectively enhancing the emission rates of electric or magnetic emitters. Indeed, the modification of the LDOS and the manipulation of magnetic dipole spontaneous emission have been studied in various pho-

tonic structures [119, 172–175], including metal films and plasmonic nanostructures. Resonant plasmonic metasurfaces consisting of an array of nanoholes in a bilayer gold film have shown a preferential enhancement only of the magnetic emission [169].

However, in the vicinity of plasmonic nanostructures, the intrinsic absorption losses of metals at optical frequencies can result in quenching of the emission. To overcome this limitation, high-index dielectric nanoparticles and metasurfaces [56, 176] have been suggested as an alternative platform to efficiently tailor the magnetic LDOS and selectively enhance magnetic radiative decay [140, 177]. The dielectric nanoparticles can support both electric and magnetic multipolar Mie-type resonances in the visible, which can be tailored by the nanoparticle geometry [56, 176]. In particular, it was shown theoretically that quadrupolar magnetic resonances in silicon particles can preferentially promote magnetic versus electric radiative channels in trivalent lanthanide ions [140]. The enhancement of the magnetic dipole emission was further studied, both analytically and numerically, for a variety of dielectric nanoparticles, including nanospheres [178] and hollow nanocylinders [179]. In the latter case, it was predicted that the emission can be significantly enhanced near the magnetic dipole resonance, while electric dipole emission will be suppressed when emitters are located in a hollow of the nanocylinder [179].

In this part, we systematically investigate the modification of magnetic and electric dipole emission from a thin layer of a polymer containing Eu^{3+} ions coated onto metasurfaces composed of a-Si:H nanocylinders arranged in a square array. We fabricated several metasurfaces with a variation of the nanocylinder diameter, which allows us to shift the spectral positions of the quadrupolar-dominated Mie-resonances over the emission range of the Eu^{3+}. Apart from the fact that our metasurface supports quadrupolar-dominated resonances, using metasurfaces is interesting by itself, as they offer many spatial degrees of freedom for tailoring and enhancing spontaneous emission [131, 180]. We experimentally probed the enhancement of the fluorescence signal from the Eu^{3+} at two different wavelengths, namely 590 nm and 610 nm, as a function of the nanocylinder diameter. The emission at the wavelength of 590 nm originates from the magnetic-dominated dipole transition and at the wavelength of 610 nm is due to the electric dipole transition $^5D_0 \rightarrow ^7 F_2$. We specifically consider the electric dipole transition at the wavelength of 610 nm, while keeping the other electric dipole transitions out of the scope, because it shows the strongest line in the emission spectrum and is spectrally closest to the magnetic dipole emission line.

This project was a collaboration with Norfolk State University. The a-Si:H nanocylinder metasurface samples were covered by Eu^{3+} containing polymer and PL microscopy images were taken by Soheila Mashhadi. The role of the author was to analyze the experimental data and simulate the linear spectra and the enhancement of emission from the metasurfaces. For the sake of completeness, we present the contributions of other people in this manuscript.

5.4.2 Experimental characterization

We fabricated twenty metasurfaces with different nanocylinder diameters ranging from 192 nm to 292 nm (measured with SEM). The period of 560 nm was the same for all metasurfaces. These metasurface samples are nominally identical to those investigated in Section 5.1. Typical SEM

images are depicted in Figure 5.3 (a) and (b) and details on the fabrication process can be found in Section 4.1.

First, we measured the normal-incidence transmittance spectra to characterize the resonant behavior of the metasurfaces. A selected experimental transmittance spectrum is shown in Figure 5.21 (a) and exhibits several pronounced dips. In order to investigate the origin of these dips, we performed numerical transmittance calculations described in Section 3.3. The results are included in Figure 5.21 (a) alongside the experimental data. The dispersion data of the materials composing the metasurface is identical to the one used in the simulations of the Section 5.1. In the calculations, to optimize the agreement with experimental spectra, we varied the nanocylinders height and diameter within the accuracy limits of the nanofabrication, yielding the values of 165 nm and 262 nm, respectively. Next, we performed the multipole decomposition of the modes excited in the nanocylinders. The results are plotted in Figure 5.21 (b) and show that the two dips at wavelengths of 920 nm and 850 nm are attributed to the MD and ED resonances, respectively. The other dips appearing at lower wavelength originate from the excitation of MQ and EQ modes. In Figure 5.22 we show the electric and magnetic field profiles in a vertical cross-section through the nanocylinder center for the modes excited at the wavelengths of the magnetic (590 nm) and electric (610 nm) dipole transitions of Eu^{3+}. We observe that the excitation of the MQ and EQ modes leads to the enhancement of the electric and magnetic fields.

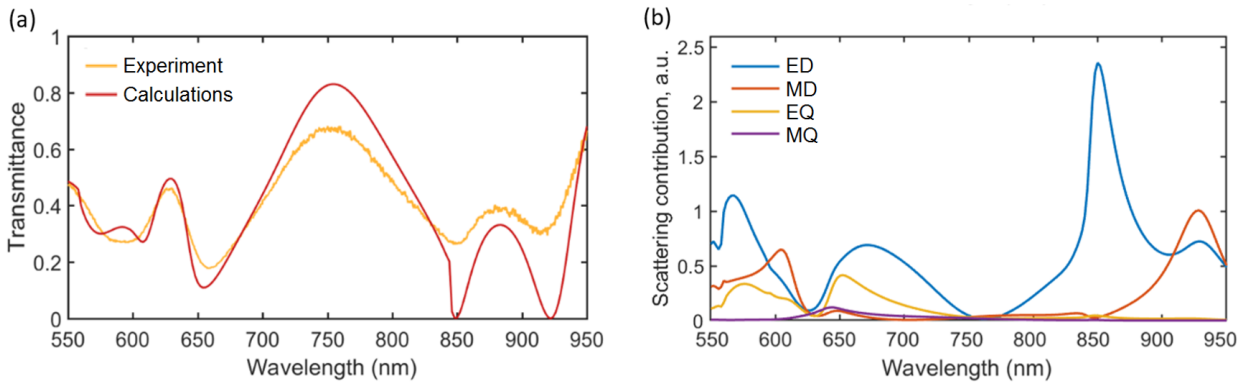

Figure 5.21: (a) Experimental and calculated normal-incidence transmittance of the metasurface with nanocylinder diameter of 262 nm and height of 165 nm. (b) Multipole decomposition of the modes excited in the metasurface by a normally incident plane wave. Reprinted with permission from [171]. Copyright (2019) American Chemical Society. The normal-incidence transmittance measurements performed by Katie E. Chong.

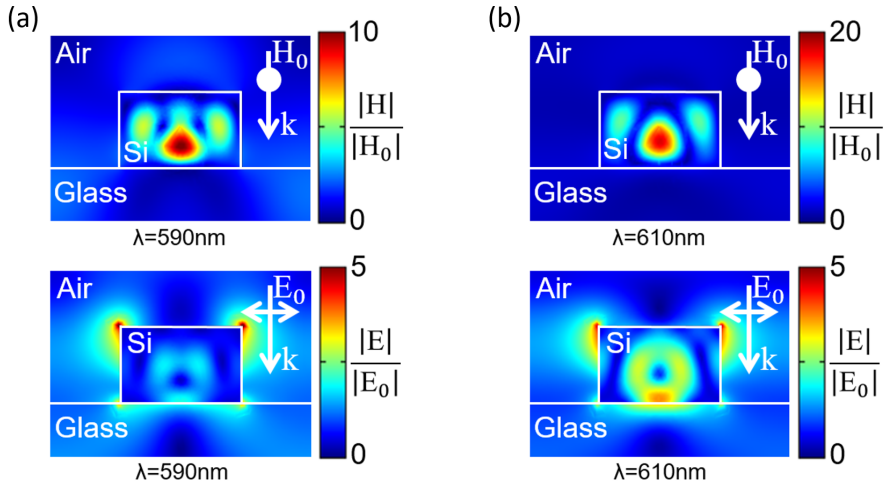

Figure 5.22: Electric and magnetic field distributions in the cross-section through the center of the nanocylinder, for a normally incident excitation plane wave with the wavelength λ of (a) 590 nm or (b) 610 nm. The nanocylinder diameter is 262 nm and height is 165 nm. Reprinted with permission from [171]. Copyright (2019) American Chemical Society.

In Figure 5.23 (a), we depict the measured transmittance spectra for all twenty metasurfaces. Each horizontal line illustrates a color plot of the transmittance spectrum for one of the metasurfaces ordered in accordance with a gradual increase in effective nanocylinder diameter. To identify the effective nanocylinder diameters and heights, we again optimized the agreement between the calculated and experimental spectra for each metasurface. The obtained effective metasurface parameters are listed in Table 5.1. In Figure 5.23 (b), we depict the corresponding calculated transmittance spectra. Even though the discrepancy in the absolute values of transmittance is present, the spectral positions of the dips can be matched very well.

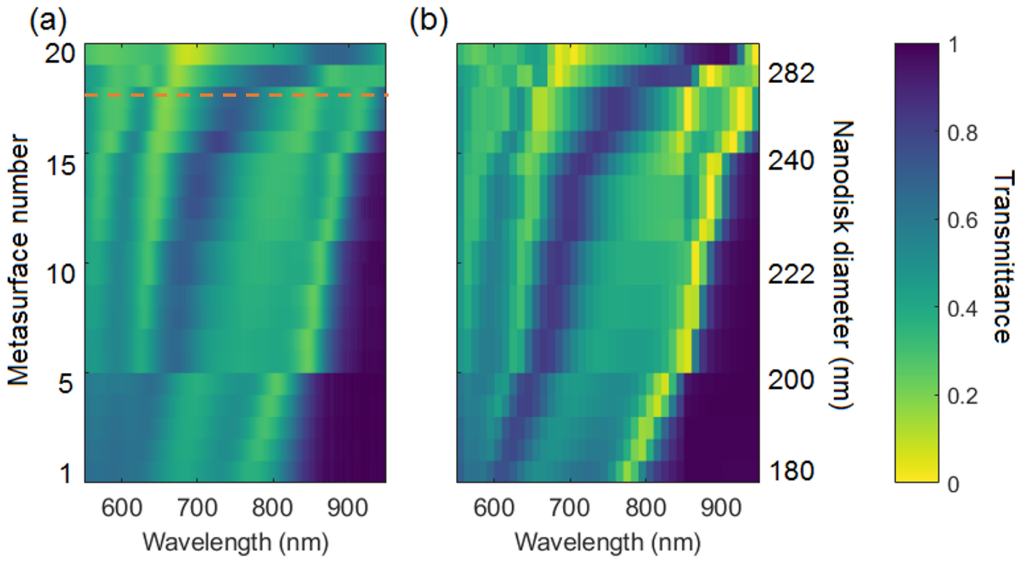

Figure 5.23: Experimental (a) and calculated (b) transmittance spectra for twenty metasurfaces, each having different effective nanocylinder diameter and height. The dashed horizontal line indicates the sample considered in Figure 5.21. Reprinted with permission from [171]. Copyright (2019) American Chemical Society. The normal-incidence transmittance measurements are performed by Katie E. Chong.

Metasurface number	diameter (nm)	height (nm)
1	180	150
2	188	150
3	192	150
4	200	150
5	200	155
6	212	160
7	212	160
8	218	160
9	218	160
10	222	161
11	222	161
12	230	165
13	230	165
14	236	160.6
15	240	160
16	250	165
17	262	165
18	262	165
19	282.8	171.7
20	320	170

Table 5.1: Effective geometrical parameters of the metasurfaces used in calculations. Reprinted with permission from [171]. Copyright (2019) American Chemical Society.

Since the Mie-resonances are red-shifting with increasing resonator dimensions, the set of the Mie-modes excited at a fixed wavelength varies for different metasurfaces. Therefore, we can investigate how the different Mie-modes are influencing both the electric and the magnetic-dominated dipole transitions in the Eu^{3+}.

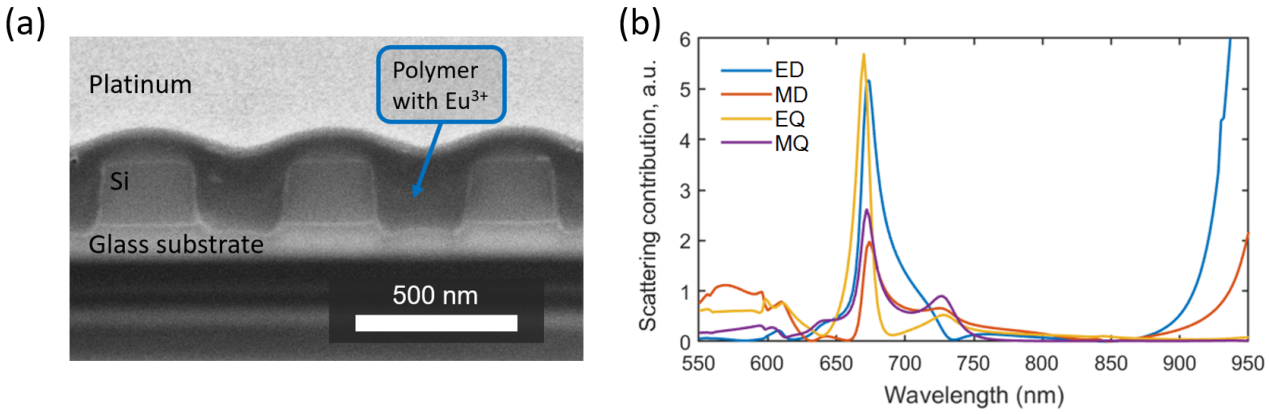

Figure 5.24: (a) SEM image of a FIB cross-section of one of the metasurfaces covered by the Eu^{3+} containing polymer. (b) Multipole decomposition of the modes in the metasurface covered by a polymer layer (refractive index of 1.6) excited by a normally incident plane wave. Reprinted with permission from [171]. Copyright (2019) American Chemical Society. The sample fabrication is done by Katie E. Chong. The sample was covered by Eu^{3+} containing polymer by Soheila Mashhadi. The FIB and SEM imaging are done by Michael Steinert.

To integrate the emitting Eu^{3+} with the metasurfaces, we prepared a solution of the Eu^{3+}

containing complex $Eu(TTA)_3L18$ and polystyrene in chloroform. Details of the preparation of the solution can be found in Wang et al. [181]. The solution was then spin-coated onto the metasurfaces to produce a thin film. In Figure 5.24 we show an SEM image of a FIB cross-section of one of the metasurfaces covered by the Eu^{3+} containing polymer layer. The introduction of the polymer, which has a refractive index of 1.6, changes the refractive index around the nanocylinders causing a red-shift of the Mie-resonances. In addition, it modifies the relative scattering contribution of the dipole and quadrupole Mie-modes (see Figure 5.24 (b)).

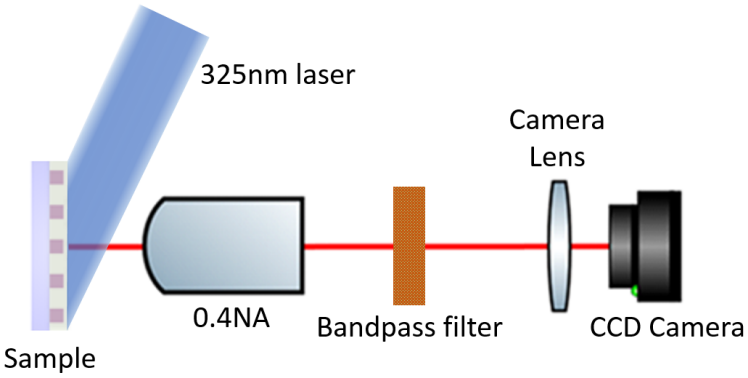

Figure 5.25: Schematics of the experimental setup used for PL microscopy. Reprinted with permission from [171]. Copyright (2019) American Chemical Society.

To probe the influence of the metasurfaces on the intensity of the emission at the wavelengths of 590 nm and 610 nm, we performed the PL microscopy measurements. A schematics of the experimental setup is illustrated in Figure 5.25. A He-Cd laser with a wavelength of 325 nm was illuminating the whole area of the sample and simultaneously exciting all coated metasurfaces and surrounding glass substrate regions. The emission from the sample was collected by an 0.4 NA objective (Olympus RMS20X) and focused on the sensor of a CCD camera (Thorlabs 1500 M GE-TE) in order to record the PL microscopy image. We introduced a BP filter with FWHM of 10 nm and center wavelength of 590 nm (Thorlabs FB590-10) or 610 nm (Thorlabs FB610-10) in the optical path to selectively probe the emission at the magnetic dipole or electric dipole transition, respectively. In Figure 5.26 (a,b), we show the PL microscopy images of the sample covered by the Eu^{3+} containing polymer layer, measured through the corresponding BP filter. Since the emission of Eu^{3+} at the wavelength of 590 nm is around 10 times weaker than at the wavelength of 610 nm (see Figure 5.20 (b)), we used different integration times to take these PL images. This results in approximately equal intensities of the emission at the wavelength of 590 nm and 610 nm in the areas in between the metasurface arrays, i.e., the bare glass substrate covered by the Eu^{3+} containing polymer layer.

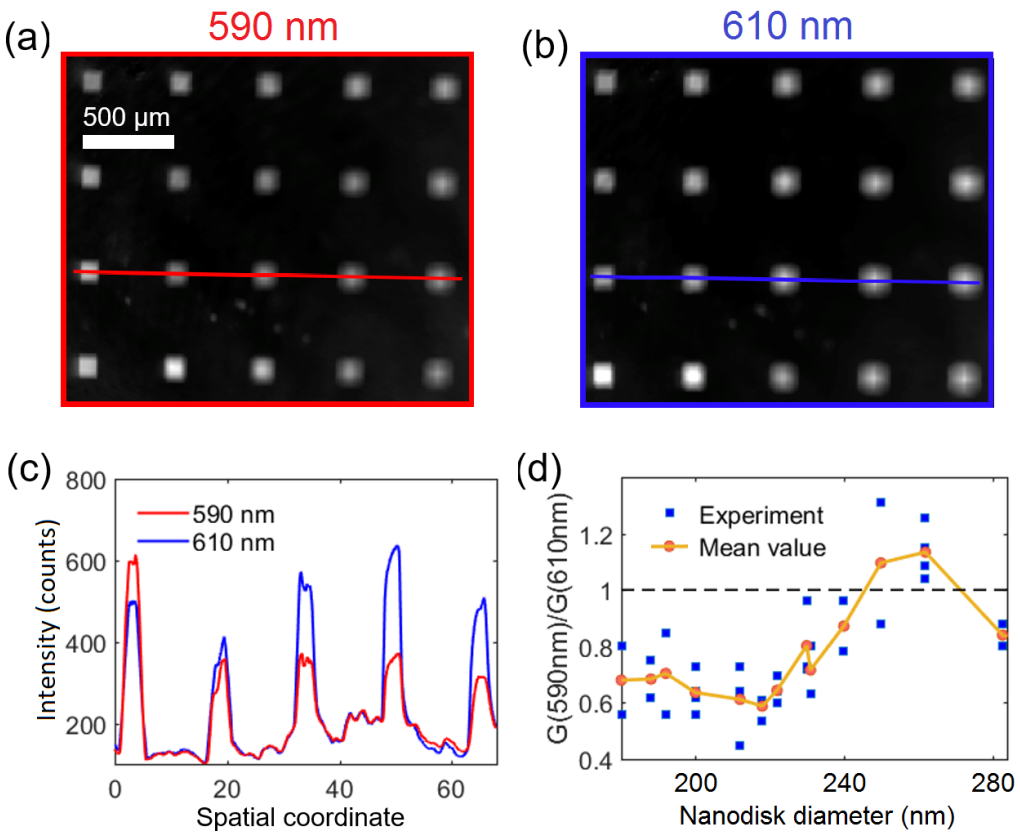

Figure 5.26: PL microscopy images of twenty metasurfaces (appear as bright squares with a footprint of 100 μm $\times$ 100 μm) with different nanocylinder diameters covered by a layer of Eu^{3+} containing polymer, recorded through BP filters with a center wavelength of (a) 590 nm and (b) 610 nm. Color from black (low) to white (high) indicates the count rate. The images were measured at different integration times of 4000 ms for the wavelength of 590 nm and 400 ms for the wavelength of 610 nm. (c) Emission intensity along the red and blue horizontal lines shown in (a,b). (d) Experimentally measured emission enhancement ratio G_{590}/G_{610} as a function of the nanocylinder diameter. Reprinted with permission from [171]. Copyright (2019) American Chemical Society. The PL microscopy measurements are done by Soheila Mashhadi.

Both images show the same 4×5 arrangement of the twenty metasurfaces, which appear as bright squares. The fluorescence signal collected from the metasurfaces is higher than the signal collected from the surrounding glass substrate regions at both considered wavelengths. In addition, we observe a variation of the fluorescence signal strength for metasurfaces having different nanocylinder parameters. To illustrate this difference, we depict in Figure 5.26 (c) the intensity over the cross-sections of the PL microscopy images indicated by the red line in Figure 5.26 (a) and the blue line in Figure 5.26 (b). Each peak appearing in Figure 5.26 (c) corresponds to one of the metasurfaces providing a multi-fold enhancement of the fluorescence signal at both wavelengths. Clearly, the enhancement factor depends on both the nanocylinder size and the emission wavelength. Possibly, the nature of the emission also plays a role. Note that in these experiments, the intensity of intrinsic fluorescence emission from the glass substrate or a-Si:H, was negligible compared to the intensity of the emission from the Eu^{3+} containing polymer covering the sample. This was confirmed by PL spectroscopy measurements.

Next, for each of the metasurfaces we define the enhancement of the fluorescence signal G_{590} (G_{610}) at the magnetic-dominated (electric) transition wavelength as the ratio of the flu-

orescence signal I_{590} (I_{610}) from the metasurface and the corresponding fluorescence signal I^0_{590} (I^0_{610}) from the bare glass substrate next to the metasurface. In Figure 5.26 (d) we plot the fluorescence signal enhancement ratio G_{590}/G_{610} as a function of the nanocylinder diameter. The experimentally measured values are depicted as blue squares. The orange circles represent the mean value for several nominally identical metasurfaces. Note, that the actual fabricated sample had two nominally identical fields, each consisting of twenty metasurfaces. The transmittance spectra measured from two corresponding metasurfaces from each of these two fields were almost identical. Only a slight (<5%) discrepancy in the absolute values was present. To provide a better statistics, we include the measurements from all forty metasurfaces in Figure 5.26 (d), except for two of them, which were overexposed according to the SEM images. The difference in the enhancement ratio values for the identical metasurfaces can be attributed to the imperfections of the fabrication, which also result in the discrepancy in transmittance spectra.

We observe that the mean value of the fluorescence signal enhancement ratio G_{590}/G_{610} depends on the nanocylinder diameter. In particular, the value of the G_{590}/G_{610} is lower than 1 for the metasurfaces with nanocylinder diameters below 240 nm. For larger nanocylinder diameters, the value of the G_{590}/G_{610} first increases and exceeds 1, but then becomes lower than 1 again. As it was expected, this systematic dependence is due to the modification of the spectral overlap of the Mie-resonances with the lines of the electric and magnetic-dominated transitions of the Eu^{3+}. The enhancement selectivity i.e. the deviation of the enhancement ratio from the level of 1 originates from the difference in emission wavelengths, affecting the spectral overlap with a particular Mie-resonance. However, the different nature of the emission also contributes to this deviation as analysed later.

5.4.3 Numerical simulations

In order to clarify if the nature of the emission influences the enhancement values, we numerically simulated the enhancement of the emission from the electric or magnetic point dipoles homogeneously distributed within a polymer layer covering the metasurfaces. For these simulations, we employed the reciprocity principle (see Section 3.1.2), which we formulated for point magnetic dipole sources [2]: $\mathbf{m}_1 \cdot \mathbf{H}_2(\mathbf{r}_1) = \mathbf{p}_2 \cdot \mathbf{E}_1(\mathbf{r}_2)$, where $\mathbf{m}_1$ is the magnetic dipole moment of the first dipole placed at position $\mathbf{r}_1$ and producing an electric field $\mathbf{E}_1(\mathbf{r})$ and $\mathbf{p}_2$ is the electric dipole moment of the second dipole placed at position $\mathbf{r}_2$ and producing a magnetic field $\mathbf{H}_2(\mathbf{r})$.

Figure 5.27 (a) shows a sketch of the unit cell used in our simulations. The a-Si:H nanocylinder (blue) was placed onto a glass substrate and covered by a polymer layer (green and red) with a refractive index of 1.6. In experiments, the Eu^{3+} containing polymer strongly absorbs the excitation laser light at the wavelength of 325 nm. Therefore, only the emitters within a thin layer at the surface of the polymer are effectively excited. We modeled this effect by dividing the polymer layer into two parts. The upper part with a thickness of 180 nm is shown by the red color and contains the excited emitters. Later in the text, we refer to this part as active layer. The bottom part (blue) has a thickness of 40 nm and is not emissive. The thickness of the active

layer is set to 180 nm based on the experimentally measured absorption and corresponds to a decay of the excitation wave intensity at the wavelength of 325 nm by a factor of 3. The unit cell was excited by a plane wave incident from the upper semi-space along the direction (θ,ϕ). Using the reciprocity principle, we can calculate the relative intensity of the angular emission from the metasurface in the upper semi-space along the same direction. The fluorescence signal measured in the experiment is proportional to the relative intensity of the angular emission integrated over the collection optics. Therefore, we estimate the enhancement $G_{\mathrm{MD}}(590\,\mathrm{nm})$ of the fluorescence signal from the point magnetic dipoles emitting at the wavelength of 590 nm, which are on average isotropically oriented and homogeneously distributed within the active layer, as:

$$G_{\mathrm{MD}}(590\ \mathrm{nm}) = \frac{P_{\mathrm{MD}}}{P^0_{\mathrm{MD}}}, \tag{5.5}$$

where

$$P_{\mathrm{MD}} = \sum_{\theta,\phi,\mathrm{TE,TM}} \left[\iiint_{active\ layer\ on\ the\ metasurface} |\mathbf{H}(\mathbf{r};\theta,\phi)|^2 d^3\mathbf{r} \right] \sin\theta, \tag{5.6}$$

and

$$P^0_{\mathrm{MD}} = \sum_{\theta,\phi,\mathrm{TE,TM}} \left[\iiint_{active\ layer\ on\ the\ glass} |\mathbf{H}(\mathbf{r};\theta,\phi)|^2 d^3\mathbf{r} \right] \sin\theta. \tag{5.7}$$

P_{MD} is the calculated relative fluorescence signal at the magnetic dipole transition from the metasurface covered by the Eu^{3+} containing polymer layer. $\mathbf{H}(\mathbf{r};\theta,\phi)$ is the magnetic field excited by either a TE- or a TM-polarized plane wave with the wavelength of 590 nm incident from the upper semi-space along the direction (θ,ϕ). The integration is taken over the active layer within a single unit cell. In order to take into account the 0.4NA of the collection optics and make use of the symmetries in the system, we varied the polar angle θ from 0° to 23° and azimuthal angle ϕ from 0° to 45°. P^0_{MD} is the calculated relative fluorescence signal at the magnetic dipole transition from a bare glass substrate covered by a Eu^{3+} containing polymer layer of a thickness of 180 nm (measured by SEM of an FIB cross-section through the unstructured area of the sample).

Similarly, the enhancement $G_{\mathrm{ED}}(610\mathrm{nm})$ of the fluorescence signal from the point electric dipoles emitting at the wavelength of 610 nm, which are also assumed to be isotropically oriented and homogeneously distributed within the active layer is estimated as:

$$G_{\mathrm{ED}}(610\ \mathrm{nm}) = \frac{P_{\mathrm{ED}}}{P^0_{\mathrm{ED}}}, \tag{5.8}$$

where

$$P_{\mathrm{ED}} = \sum_{\theta,\phi,\mathrm{TE,TM}} \left[\iiint_{active\ layer\ on\ the\ metasurface} |\mathbf{E}(\mathbf{r};\theta,\phi)|^2 d^3\mathbf{r} \right] \sin\theta, \tag{5.9}$$

and

$$P^0_{\mathrm{ED}} = \sum_{\theta,\phi,\mathrm{TE,TM}} \left[\iiint_{active\ layer\ on\ the\ glass} |\mathbf{E}(\mathbf{r};\theta,\phi)|^2 d^3\mathbf{r} \right] \sin\theta. \tag{5.10}$$

Here P_{ED} is the calculated relative fluorescence signal at the electric dipole transition from the metasurface covered by a Eu^{3+} containing polymer layer. $\mathbf{E}(\mathbf{r};\theta,\phi)$ is the electric field excited by either a TE- or a TM-polarized plane wave with the wavelength of 610 nm incident from the upper semi-space along the direction (θ,ϕ). P^0_{ED} is the relative fluorescence signal from a bare glass substrate covered by a polymer layer of thickness 180 nm at the electric dipole transition. The collection NA and normalization procedure are the same as for the case of the magnetic dipole emitters.

Note that our approach does not take into account the complex electronic level structure of the Eu^{3+}, and the calculated fluorescence signal enhancement only includes the radiative decay rate and collection efficiency enhancements. In the last section of this chapter Section 5.4.5 we discuss the limitations of this approach.

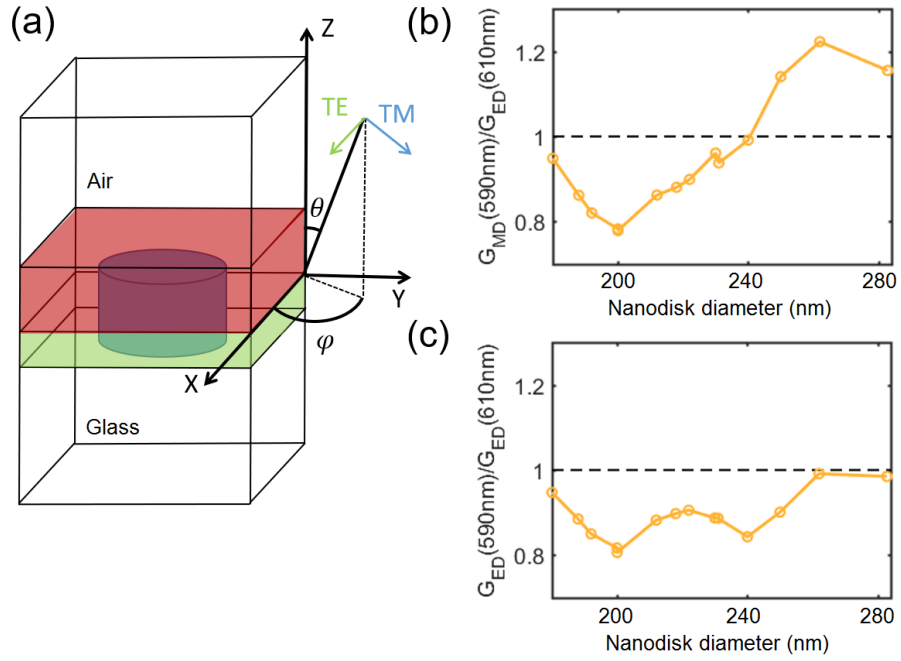

Figure 5.27: (a) Illustration of the unit cell used in calculations. The a-Si:H nanocylinder is embedded into a polymer later consisting of an active (red) and inactive (green) parts. The active layer is red and the inactive part of the polymer layer is green. (b) Calculated ratio of the fluorescence signal enhancement originating from the magnetic dipole emission at 590 nm wavelength and the fluorescence signal enhancement originating from the electric dipole emission at 610 nm wavelength as a function of nanocylinder diameter. (c) Calculated ratio of the fluorescence signal enhancement originating from the electric dipole emission at 590 nm wavelength and the fluorescence signal enhancement originating from the electric dipole emission at 610 nm wavelength as a function of nanocylinder diameter. Reprinted with permission from [171]. Copyright (2019) American Chemical Society.

In Figure 5.27 (b) we plot the calculated fluorescence signal enhancement ratio $G_{\mathrm{MD}}(590\,\mathrm{nm})/G_{\mathrm{ED}}(610\,\mathrm{nm})$ as a function of the nanocylinder diameter. In these calculations, we used the effective parameters of the nanocylinders listed in Section 5.4.2. Noticeably, we have a good qualitative agreement with the experimental data shown in Figure 5.26 (d). Indeed,

all the important trends observed in the experiment are well reproduced, with only slight discrepancies in the values.

To evaluate how the nature of the emission affects the fluorescence signal enhancement, we also calculated the fluorescence signal enhancement ratio $G_{\mathrm{ED}}(590\,\mathrm{nm})/G_{\mathrm{ED}}(610\,\mathrm{nm})$ assuming that the emission at the wavelength of 590 nm originates purely from electric dipole transition by evaluating Equations (5.8) to (5.10) for the wavelength of 590 nm. The results are plotted in Figure 5.27 (c). We observe a qualitative difference compared to the experimental data presented in Figure 5.26 (d). This difference is a strong sign of the importance of the emission nature.

5.4.4 Emission directionality

Taminiau et. al.[137] demonstrated that the light emission due to the magnetic dipole transition can be quantified by means of the BFP imaging and subsequent analysis of the emission patterns. Here we theoretically investigate if the angular emission from a metasurface depends on the nature of the corresponding transition. We performed the numerical simulations of the metasurface with a nanocylinder diameter of 262 nm, but not covered by the polymer. The metasurface was driven by a single point electric or magnetic dipole source located 10 nm above the center of one of the nanocylinders and oscillating at the frequency corresponding to the wavelength of 590 nm. Figure 5.28 shows the calculated emission patterns for both electric and magnetic dipole excitation. We observe a significant difference in two emission patterns originating due to the different nature of the emitter. Future research on Mie-resonant nanostructures tailoring the emission from Eu^{3+} can be dedicated to the design of the sample that increases this difference.

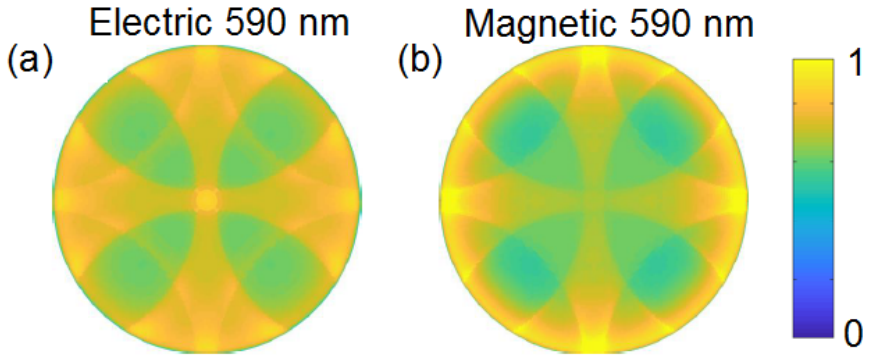

Figure 5.28: Calculated BFP images of the emission from the metasurface with nanocylinder diameter of 286 driven by a single point electric (a) or magnetic (b) dipole source located 10 nm above the center of one of the nanocylinders and oscillating at the frequency corresponding to the wavelength of 590 nm. The size of the BFP images corresponds to the objective with the NA of 1. Reprinted with permission from[171]. Copyright (2019) American Chemical Society.

5.4.5 Discussion

We have experimentally demonstrated the enhancement of the fluorescence signal from dielectric metasurfaces covered by a polymer containing the Eu^{3+}. The fabricated metasurfaces

feature different nanocylinder dimensions, thus implementing a sweep of the position of the Mie-resonances with a strong quadrupole contribution over the spectral range of the electric and magnetic-dominated dipole transitions of the Eu^{3+}. We observed a systematic change of the enhancement ratio G_{590}/G_{610} due to the variation of the metasurface parameters and were able to confirm our observations with numerical simulations. However, some discrepancies were observed. Especially, the absolute values for the fluorescence signal enhancement appear approximately four times higher in the experiment, independent of the nanocylinder diameter (see Figure 5.29). Here we discuss possible reasons behind this.

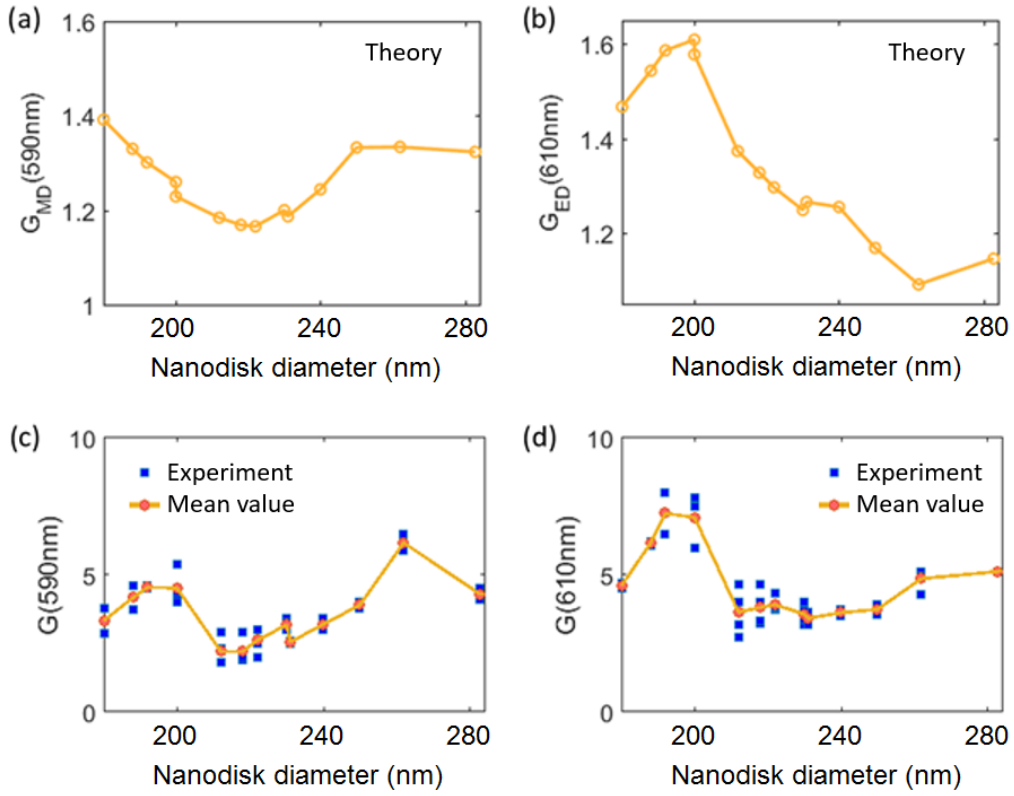

Figure 5.29: Calculated (a,b) and experimentally measured (c,d) absolute fluorescence signal enhancement for the magnetic (a,c) and electric (b,d) dipole transition as a function of nanocylinder diameter. In (c,d), the blue squares correspond to the experimentally measured values for individual metasurface arrays, the orange circles represent the mean value averaged over all nominally identical metasurfaces. Reprinted with permission from [171]. Copyright (2019) American Chemical Society.

The fluorescence signal from a single Eu^{3+} ion placed in a certain position $\mathbf{r}$ can be factorized in accordance with the Equation (2.58). Due to the high absorption of UV light by a-Si:H, our metasurfaces do not significantly enhance the excitation rate. The exact calculations of the excitation enhancement could not be performed due to the lack of the dispersion data at 325 nm. Therefore, we take this factor out of consideration. To account for coupling between transitions in the multilevel system shown Figure 5.24, we introduce the magnetic and electric quantum yields: $QY_m(\mathbf{r},\omega_m) = \Gamma_m(\mathbf{r},\omega_m)/\Gamma_{Total}(\mathbf{r})$ and $QY_e(\mathbf{r},\omega_e) = \Gamma_e(\mathbf{r},\omega_e)/\Gamma_{Total}(\mathbf{r})$, where $\Gamma_m(\mathbf{r})$ is the magnetic dipole transition rate at the frequency ω_m corresponding to the wavelength of 590 nm, $\Gamma_e(\mathbf{r})$ is the electric dipole transition rate at the frequency ω_e corresponding to the wavelength of 610 nm and $\Gamma_{total}(\mathbf{r})$ is the total transition rate including all radiative channels

and the intrinsic losses. Consequently, the QY enhancement is dependent on the transition rate enhancements of all channels. For instance, the quantum yield corresponding to a magnetic dipole transition at 590 nm can be increased by suppressing the electric dipole transition rate at 610 nm [119].

In the experiment, the ensembles of Eu^{3+} ions are distributed over the whole metasurface and contribute to the emission. Therefore, the measured intensity of the emission from the metasurface can be estimated as:

$$I_{590} \propto \iiint_{unit\ cell\ volume} \frac{\Gamma_m(\mathbf{r},\omega_m)}{\Gamma_{Total}(\mathbf{r})} \eta_{ext}(\mathbf{r},\omega_m)\eta_{coll}(\mathbf{r},\omega_m)\rho(\mathbf{r})d^3(\mathbf{r}) \tag{5.11}$$

$$I_{610} \propto \iiint_{unit\ cell\ volume} \frac{\Gamma_e(\mathbf{r},\omega_e)}{\Gamma_{Total}(\mathbf{r})} \eta_{ext}(\mathbf{r},\omega_e)\eta_{coll}(\mathbf{r},\omega_e)\rho(\mathbf{r})d^3(\mathbf{r}) \tag{5.12}$$

where $\rho(\mathbf{r})$ is the emitter density. Note that to obtain the total emission count rate, we need to take the efficiency of the detector system (i.e. coupling efficiencies, quantum efficiency) into account and perform a proper calibration of the experimental setup. However, since the considered electrical dipole and magnetic dipole transitions are spectrally close, the corresponding detection efficiencies will be almost the same.

On the other hand, the calculations based on the reciprocity principle do not take into account the total decay rate and only allow for estimation the contributions from the decay rate enhancement, extraction, and collection efficiencies:

$$G_{590} \propto \iiint_{unit\ cell\ volume} \Gamma_m(\mathbf{r},\omega_m)\eta_{ext}(\mathbf{r},\omega_m)\eta_{coll}(\mathbf{r},\omega_m)\rho(\mathbf{r})d^3(\mathbf{r}) \tag{5.13}$$

$$G_{610} \propto \iiint_{unit\ cell\ volume} \Gamma_e(\mathbf{r},\omega_e)\eta_{ext}(\mathbf{r},\omega_e)\eta_{coll}(\mathbf{r},\omega_e)\rho(\mathbf{r})d^3(\mathbf{r}) \tag{5.14}$$

Generally, in the previous sections, we compared the ratios between the experimentally measured intensities and calculated enhancement. Strictly speaking, such approach is invalid in case of a metasurface, since the total decay rate is depending on the position of the emitter and cannot be taken out of the integrals in Equations (5.11) and (5.12) and be reduced in the ratios. Thus, our calculations neglect possible effects of the metasurfaces on the decay rates of the other electric dipole transition channels, present in the Eu^{3+} (see Figure 5.20).

Another effect that we left out of consideration in the calculations is the out-coupling of guided waves by the metasurfaces. In the PL microscopy setup, the laser light is not focused on a particular metasurface. Instead, it illuminates the whole sample and simultaneously excites the Eu^{3+} on the metasurfaces and on the bare glass substrate (coverslip). The most of the emission from Eu^{3+} on the bare glass substrate is coupled to the modes propagating inside the coverslip above the critical angle (see Figure 4.7 (b)) and can only escape it at the edges of the coverslip. However, when these guided waves reach the periodic metasurface, they can be out-coupled due to the diffraction. This effect potentially leads to an additional signal from the metasurfaces and can explain the discrepancy in the absolute values of the measured fluorescence signal compared to the calculated enhancement values.

In a zeroth-order approach, the out-coupling efficiency is proportional to the scattering strength of the nanocylinders composing the metasurface and can be related to extinction defined as $1 - \mathrm{T}$, where T is the measured transmission. Figure 5.30 depicts the extinction ratio $(1-\mathrm{T}(590))/(1-\mathrm{T}(610))$, where T(590) and T(610) are experimentally measured normal-incidence transmission through the metasurfaces covered by the polymer, evaluated at the wavelength of 590 nm or 610 nm, respectively. We observe a curve similar to the measured enhancement ratio in Figure 5.26 (d), but blue-shifted.

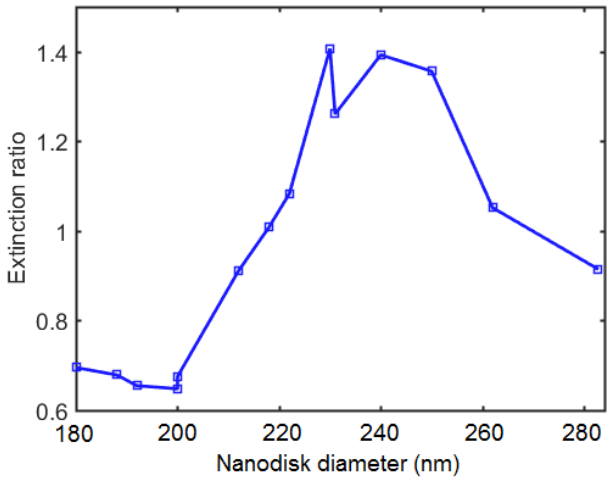

Figure 5.30: Extinction ratio $(1 - \mathrm{T}(590))/(1 - \mathrm{T}(610))$, where T(590) and T(610) are experimentally measured normal-incidence transmission through the metasurfaces covered by polymer, evaluated at the wavelength of 590 nm or 610 nm, respectively.

These effects should be addressed in future work on Mie-resonant nanostructures tailoring the emission from Eu^{3+}.

Chapter 6

Conclusion and Outlook

The aim of this thesis was to investigate how the modes of the dielectric metasurfaces influence the emission characteristics of emitters coupled to them. To achieve this, we investigated a range of different light-emitting metasurface architectures comprising different designs and emitter systems. The fabricated metasurfaces were characterized by the normal-incidence transmittance or reflectance spectroscopy. To model the electromagnetic behavior of the metasurface theoretically, we utilized the FEM method. Various different emitter systems were studied, including impurities in a glass substrate, InAs QDs integrated during the fabrication process and Eu^{3+} ions featuring the magnetic-dominated transition. The emission modified by the metasurfaces was examined experimentally by various different techniques ranging from PL spectroscopy over BFP imaging to momentum-resolved spectroscopy. For the latter two techniques, a dedicated optical setup was constructed in the course of this thesis. We also developed a numerical approach based on the reciprocity principle to simulate the measured BFP images, PL signal enhancement and momentum-resolved spectroscopy data.

First, we have experimentally demonstrated spectral reshaping of the broadband emission from color centers in a glass substrate by coupling to the ED and MD resonances of all-dielectric silicon nanocylinder metasurfaces. The PL spectra measured from different metasurfaces exhibit two peaks, which are spectrally coinciding with the dips in the corresponding transmittance spectra. Using numerical simulations we were able to link the dips in the transmittance spectra to the excitation of ED and MD resonances in the silicon nanocylinders. Furthermore, to achieve the desired directionality of the emission and enhance the collection efficiency we exploited the lattice modes and tailored coherent scattering in the periodic arrangement. The directionality of the emission was confirmed experimentally by BFP imaging and numerically using the reciprocity principle. By harnessing both Mie- and lattice resonances of the nanocylinder arrays we achieved a PL signal enhancement of 28 compared to the reference measurements from the bare glass substrate. We discussed the limitations of the sample architecture for further enhancement of the PL signal. In particular, the coupling of the emission into the guided modes of the glass substrate significantly reduces the collection efficiency.

Second, we studied GaAs nanocylinder metasurfaces with InAs QDs integrated directly inside the resonators. This new platform offers distinct advantages: it provides an effective spatial overlap of the resonantly enhanced near-fields with the emitters. Furthermore, this is

an efficient light-emitting platform. Additionally, due to the 500 nm low-index pedestal, the emission from QDs does not effectively couple to the guided modes of the GaAs substrate, which allows for harvesting more photons in the experiment. We show that the MQ modes excited in individual resonators provide a PL signal enhancement of up to 19 and have a significant effect on the emission pattern. Indeed, the emission can be squeezed into a narrow lobe directed normally out of the metasurface plane. Alternatively, by altering the metasurface design, the emission along this direction can be suppressed and directed into the side lobes. Furthermore, the presence of lattice modes leads to the hybridization with the Mie-modes and results in high-Q out-of-plane dipole resonances observed in a specifically designed broken-symmetry metasurface. Such resonances provide a lifetime reduction as well as large PL signal enhancement up to 290, which is also contributed by an extraction and collection efficiency enhancement.

Finally, we investigated the enhancement of PL emission from Eu^{3+} ions featuring both electric and magnetic-dominated dipole transitions, by all-dielectric silicon nanocylinder metasurfaces. We fabricated a series of metasurfaces with different nanocylinder diameters to sweep the position of Mie-resonances with strong quadrupole contribution over the spectral range of the electric and magnetic-dominated dipole transitions. We observed a systematic change of the ratio of the enhancements of the emission via the two different channels. Interestingly, some metasurfaces provide higher enhancement values for the PL signal from the magnetic dipole emission compared to the electric dipole emission. We confirmed the experimental observations with numerical simulations based on the reciprocity principle. Importantly, we demonstrated numerically that the nature of the emission significantly influences the PL enhancement by Mie-resonances and the resulting emission patterns.

The results of this thesis show that there are several possibilities to control the light emission by dielectric metasurfaces. The localized Mie-modes, as well as their hybrids with lattice modes allow for significant enhancement of the radiative decay rate, while the low dissipative losses of dielectric materials allow for a high QY of the coupled system. Additionally, we realized different strategies for controlling the emission pattern. Such control can be implemented by the excitation of a specific Mie-mode in single nanoresonators, as well as by tailoring the lattice modes and thereby the interference of the scattering contributions from different scatterers in the metasurface.

For all sample architectures we were able to achieve a good agreement between the measured and calculated data underpinning the accuracy and applicability of the experimental and numerical methods. These numerical methods can be later used for the design of new light-emitting metasurfaces to exploit the studied effects originating from the coupling to Mie- and lattice modes for lighting and other applications. In particular, the results of this thesis deepen understanding of how to use metasurfaces for directionality engineering and control over radiative decay rate enhancement in the new generation of LEDs. The power of current LEDs is limited by many-body quenching effects in the active region. Indeed, the increased carrier density at the high operating power of the LEDs gives rise to the nonradiative Auger recombination process, which causes a drop in the light-emission efficiency [45]. The integration of a

dielectric metasurface into the active region of the LEDs can increase the radiative LDOS and promote the radiative recombination processes over the nonradiative ones. Finally, numerous possibilities of engineering the light extraction and beaming in LEDs are offered by dielectric metasurfaces via tailoring the "array factor" and scattering properties of the individual elements, as was demonstrate in this thesis.

Deutschsprachige Zusammenfassung

Das Hauptziel dieser Arbeit ist es zu demonstrieren, wie dielektrische Metaoberflächen die Emission von mit ihnen gekoppelten nanoskaligen Lichtquellen verbessern und steuern können. Dies umfasst die experimentelle Realisierung gekoppelter photonischer Systeme aus Emittern und dielektrischen Metaoberflächen, die Entwicklung optischer Aufbauten zur Charakterisierung der Emissionseigenschaften und numerische Simulationen zur Unterstützung der experimentellen Daten und zur Analyse der zugrunde liegenden physikalischen Mechanismen.

Zunächst untersuchen wir eine dielektrische Metaoberfläche aus Silizium-Nanozylindern auf einem fluoreszierenden Glassubstrat. Wir demonstrieren experimentell die Emissionsverbesserung durch Mie-resonante dielektrische Nanozylinder in Kombination mit einer gerichteten Emission senkrecht zur Substratebene aufgrund kohärente Streuung einzelner Strahler durch die periodische Anordnung der Nanozylinder innerhalb der Metaoberfläche. Zweitens untersuchen wir die Lichtemission einer Metaoberfläche aus III-V-Halbleiter-Nanozylindern mit integrierten Quantenpunkten. In diesem System demonstrieren wir die Kontrolle über die Winkelemissionsverteilung nicht nur durch Anpassung der Anordnung der Nanozylinder, sondern auch durch die Konstruktion der Streueigenschaften eines einzelnen Nanozylinders. Als nächstes untersuchen wir eine Metaoberfläche mit gebrochener Symmetrie, die aus ähnlichen III-V-Halbleiter-Nanoresonator mit integrierten Quantenpunkten besteht. Die Metaoberfläche mit gebrochener Symmetrie zeigt eine hochwertige kollektive Mod, die aus der Hybridisierung einer lokalisierten Mie- und Gitterresonanz stammt. Die Fernfeldkopplung dieses Hybridmodus kann durch Verringern der Symmetrie der Nanoresonator manipuliert werden. Wir zeigen eine Verstärkung des Photolumineszenzsignals um zwei Größenordnungen und eine Umformung des Emissionsmusters aufgrund der Kopplung an diesen Modus. Schließlich konzentrieren wir uns auf dielektrische Metaoberflächen, die von einem Polymer bedeckt sind, das mit Lanthanidionen dotiert ist und einen sichtbaren magnetischen Dipolübergang aufweist. Wir demonstrieren die Verbesserung sowohl der elektrischen als auch der magnetischen lokalen Zustandsdichte durch Anregung von Mie-Resonanzen in den Metaoberflächen. Interessanterweise wird für ausgewählte Parameter der Metaoberfläche die magnetische Emission bevorzugt erhöht.

Für alle Beispielarchitekturen konnten wir eine gute Übereinstimmung zwischen den gemessenen und berechneten Daten erzielen, was die Genauigkeit und Anwendbarkeit der experimentellen und numerischen Methoden untermauert. Diese numerischen Methoden können später für das Design neuer lichtemittierender Metaoberflächen verwendet werden, um die untersuchten Effekte aus der Kopplung an Mie- und Gittermodi für Beleuchtung und andere Anwendungen zu nutzen. Insbesondere vertiefen die Ergebnisse dieser Arbeit das Verständnis

für die Verwendung von Metaoberflächen für die Richtungsentwicklung und die Steuerung der Verbesserung der Strahlungsabklingrate in der neuen Generation von LEDs. Insbesondere vertiefen die Ergebnisse dieser Arbeit das Verständnis für die Verwendung von Metaoberflächen zur Optimierung neuer Generationen von LEDs durch die gezielten Kontrolle der Abstrahlcharakteristik bzw. der Strahlungsabklingrate. Die Integration einer dielektrischen Metaoberfläche in den aktiven Bereich der LEDs kann das Strahlungs-LDOS erhöhen und die Strahlungsrekombinationsprozesse gegenüber den nicht strahlenden fördern. Darüber hinaus bieten dielektrische Metaoberflächen zahlreiche Möglichkeiten, die Lichtextraktion und das Strahlen in LEDs zu konstruieren, indem der "Array-Faktor" und die Streuungseigenschaften der einzelnen Elemente angepasst werden, wie in dieser Arbeit gezeigt wurde.

List of own publications

This thesis is based on the following publications:

- A. Vaskin, S. Liu, S. Addamane, B. Leung, M.-C. Tsai, Y. Yang, P. P. Vabishchevich, G. A. Keeler, G. Wang, X. He, Y. Kim, N. F. Hartmann, H. Htoon, S. K. Doorn, M. Zilk, T. Pertsch, G. Balakrishnan, M. B. Sinclair, I. Brener, and I. Staude, "Manipulation of quantum dot emission with semiconductor metasurfaces exhibiting magnetic quadrupole resonances.", To be submitted **x**, xxxx–xxxx (2020)

- A. Vaskin, R. Kolkowski, A. F. Koenderink, and I. Staude, "Light-emitting metasurfaces", Nanophotonics **8**, 1151–1198 (2019)

- A. Vaskin, S. Mashhadi, M. Steinert, K. E. Chong, D. Keene, S. Nanz, A. Abass, E. Rusak, D.-Y. Choi, I. Fernandez-Corbaton, T. Pertsch, C. Rockstuhl, M. A. Noginov, Y. S. Kivshar, D. N. Neshev, N. Noginova, and I. Staude, "Manipulation of Magnetic Dipole Emission from Eu3+ with Mie-Resonant Dielectric Metasurfaces", Nano Lett. **19**, 1015–1022 (2019)

- S. Liu, A. Vaskin, S. Addamane, B. Leung, M.-C. Tsai, Y. Yang, P. P. Vabishchevich, G. A. Keeler, G. Wang, X. He, Y. Kim, N. F. Hartmann, H. Htoon, S. K. Doorn, M. Zilk, T. Pertsch, G. Balakrishnan, M. B. Sinclair, I. Staude, and I. Brener, "Light-Emitting Metasurfaces: Simultaneous Control of Spontaneous Emission and Far-Field Radiation", Nano Lett. **18**, 6906–6914 (2018)

- A. Vaskin, J. Bohn, K. E. Chong, T. Bucher, M. Zilk, D.-Y. Choi, D. N. Neshev, Y. S. Kivshar, T. Pertsch, and I. Staude, "Directional and Spectral Shaping of Light Emission with Mie-Resonant Silicon Nanoantenna Arrays", ACS Photonics **5**, 1359–1364 (2018)

- S. Liu, A. Vaskin, S. Campione, O. Wolf, M. B. Sinclair, J. Reno, G. A. Keeler, I. Staude, and I. Brener, "Huygens' Metasurfaces Enabled by Magnetic Dipole Resonance Tuning in Split Dielectric Nanoresonators", Nano Letters **17**, 4297–4303 (2017)

Other works by the author published in the course of this thesis:

- T. Bucher, A. Vaskin, R. Mupparapu, F. J. F. Löchner, A. George, K. E. Chong, S. Fasold, C. Neumann, D.-Y. Choi, F. Eilenberger, F. Setzpfandt, Y. S. Kivshar, T. Pertsch, A. Turchanin, and I. Staude, "Tailoring Photoluminescence from MoS_2 Monolayers by Mie-Resonant Metasurfaces", ACS Photonics (2019)

- S. Liu, P. P. Vabishchevich, A. Vaskin, J. L. Reno, G. A. Keeler, M. B. Sinclair, I. Staude, and I. Brener, "An all-dielectric metasurface as a broadband optical frequency mixer", Nature Communications **9** (2018)

- M. R. Shcherbakov, S. Liu, V. V. Zubyuk, A. Vaskin, P. P. Vabishchevich, G. Keeler, T. Pertsch, T. V. Dolgova, I. Staude, I. Brener, and A. A. Fedyanin, "Ultrafast all-optical tuning of direct-gap semiconductor metasurfaces", Nature Communications **8** (2017)

Bibliography

[1] J. D. Jackson, *Classical Electrodynamics* (John Wiley & Sons Inc, July 27, 1998), 832 pp.

[2] L. D. Landau, L. P. Pitaevskii, and E. M. Lifshitz, *Electrodynamics of Continuous Media* (Elsevier, Oct. 15, 1984), 460 pp.

[3] M. Donya, M. Radford, A. ElGuindy, D. Firmin, and M. H. Yacoub, "Radiation in medicine: Origins, risks and aspirations", Global Cardiology Science and Practice **2014**, 57 (2014).

[4] *Radiation in Medicine* (National Academies Press, Mar. 1996).

[5] C. Mack, *Fundamental Principles of Optical Lithography* (John Wiley & Sons, Ltd, Nov. 2007).

[6] R. Doering and Y. Nishi, eds., *Handbook of Semiconductor Manufacturing Technology, Second Edition* (CRC Press, July 2007).

[7] S. W. Ellingson, *Radio Systems Engineering* (Cambridge University Press, Oct. 2016).

[8] H. Hertz, "Ueber Strahlen electrischer Kraft", Annalen der Physik **272**, 769–783 (1889).

[9] C. Balanis, "Antenna theory: a review", Proceedings of the IEEE **80**, 7–23 (1992).

[10] C. A. Balanis, "Antenna Theory: Analysis and Design", Wiley-Interscience (2005).

[11] T. A. Milligan, *Modern Antenna Design* (John Wiley & Sons, Inc., Jan. 2005).

[12] A. Pimpin and W. Srituravanich, "Review on Micro- and Nanolithography Techniques and their Applications", Engineering Journal **16**, 37–56 (2012).

[13] P. Bharadwaj, B. Deutsch, and L. Novotny, "Optical Antennas", Adv. Opt. Photonics **1**, 438–483 (2009).

[14] P. Biagioni, J.-S. Huang, and B. Hecht, "Nanoantennas for visible and infrared radiation", Rep. Prog. Phys. **75**, 024402 (2012).

[15] A. F. Koenderink, "Single-photon nanoantennas", ACS Photonics **4**, 710–722 (2017).

[16] T. H. Taminiau, F. D. Stefani, and N. F. van Hulst, "Enhanced directional excitation and emission of single emitters by a nano-optical Yagi-Uda antenna", Optics Express **16**, 10858 (2008).

[17] A. G. Curto, G. Volpe, T. H. Taminiau, M. P. Kreuzer, R. Quidant, and N. F. van Hulst, "Unidirectional Emission of a Quantum Dot Coupled to a Nanoantenna", Science **329**, 930–933 (2010).

[18] T. Kosako, Y. Kadoya, and H. F. Hofmann, "Directional control of light by a nano-optical Yagi–Uda antenna", Nature Photonics **4**, 312–315 (2010).

[19] T. Coenen, E. J. R. Vesseur, A. Polman, and A. F. Koenderink, "Directional Emission from Plasmonic Yagi-Uda Antennas Probed by Angle-Resolved Cathodoluminescence Spectroscopy", Nano Lett. **11**, 3779–3784 (2011).

[20] D. Dregely, R. Taubert, J. Dorfmüller, R. Vogelgesang, K. Kern, and H. Giessen, "3D optical Yagi–Uda nanoantenna array", Nature Communications **2** (2011) 10.1038/ncomms1268.

[21] I. S. Maksymov, I. Staude, A. E. Miroshnichenko, and Y. S. Kivshar, "Optical Yagi-Uda nanoantennas", Nanophotonics **1** (2012) 10.1515/nanoph-2012-0005.

[22] A. E. Krasnok, I. S. Maksymov, A. I. Denisyuk, P. A. Belov, A. E. Miroshnichenko, C. R. Simovski, and Y. S. Kivshar, "Optical nanoantennas", Physics-Uspekhi **56**, 539–564 (2013).

[23] M. Ramezani, A. Casadei, G. Grzela, F. Matteini, G. Tütüncüoglu, D. Rüffer, A. F. i Morral, and J. G. Rivas, "Hybrid Semiconductor Nanowire–Metallic Yagi-Uda Antennas", Nano Letters **15**, 4889–4895 (2015).

[24] R. Kullock, M. Ochs, P. Grimm, M. Emmerling, and B. Hecht, "Electrically-driven Yagi-Uda antennas for light", Nature Communications **11** (2020) 10.1038/s41467-019-14011-6.

[25] L. Langguth, D. Punj, J. Wenger, and A. F. Koenderink, "Plasmonic Band Structure Controls Single-Molecule Fluorescence", ACS Nano **7**, 8840–8848 (2013).

[26] L. Langguth, A. H. Schokker, K. Guo, and A. F. Koenderink, "Plasmonic phase-gradient metasurface for spontaneous emission control", Phys. Rev. B **92**, 205401 (2015).

[27] G. Lozano, G. Grzela, M. A. Verschuuren, M. Ramezani, and J. G. Rivas, "Tailor-made directional emission in nanoimprinted plasmonic-based light-emitting devices", Nanoscale **6**, 9223–9229 (2014).

[28] J. Sun, E. Timurdogan, A. Yaacobi, E. S. Hosseini, and M. R. Watts, "Large-scale nanophotonic phased array", Nature **493**, 195–199 (2013).

[29] C. T. DeRose, R. D. Kekatpure, D. C. Trotter, A. Starbuck, J. R. Wendt, A. Yaacobi, M. R. Watts, U. Chettiar, N. Engheta, and P. S. Davids, "Electronically controlled optical beam-steering by an active phased array of metallic nanoantennas", Optics Express **21**, 5198 (2013).

[30] C. V. Poulton, A. Yaacobi, D. B. Cole, M. J. Byrd, M. Raval, D. Vermeulen, and M. R. Watts, "Coherent solid-state LIDAR with silicon photonic optical phased arrays", Optics Letters **42**, 4091 (2017).

[31] J. Notaros, M. Raval, M. Notaros, and M. R. Watts, "Integrated-Phased-Array-Based Visible-Light Near-Eye Holographic Projector", in Conference on Lasers and Electro-Optics (2019).

[32] L. Novotny and N. van Hulst, "Antennas for light", Nature Photonics **5**, 83–90 (2011).

[33] V. F. Gili, L. Carletti, A. Locatelli, D. Rocco, M. Finazzi, L. Ghirardini, I. Favero, C. Gomez, A. Lemaı tre, M. Celebrano, C. D. Angelis, and G. Leo, "Monolithic AlGaAs second-harmonic nanoantennas", Optics Express **24**, 15965 (2016).

[34] R. Camacho-Morales, M. Rahmani, S. Kruk, L. Wang, L. Xu, D. A. Smirnova, A. S. Solntsev, A. Miroshnichenko, H. H. Tan, F. Karouta, S. Naureen, K. Vora, L. Carletti, C. D. Angelis, C. Jagadish, Y. S. Kivshar, and D. N. Neshev, "Nonlinear Generation of Vector Beams From AlGaAs Nanoantennas", Nano Letters **16**, 7191–7197 (2016).

[35] S. Liu, M. B. Sinclair, S. Saravi, G. A. Keeler, Y. Yang, J. Reno, G. M. Peake, F. Setzpfandt, I. Staude, T. Pertsch, and I. Brener, "Resonantly Enhanced Second-Harmonic Generation Using III–V Semiconductor All-Dielectric Metasurfaces", Nano Letters **16**, 5426–5432 (2016).

[36] S. Liu, P. P. Vabishchevich, A. Vaskin, J. L. Reno, G. A. Keeler, M. B. Sinclair, I. Staude, and I. Brener, "An all-dielectric metasurface as a broadband optical frequency mixer", Nature Communications **9** (2018).

[37] E. Rahimi and R. Gordon, "Nonlinear Plasmonic Metasurfaces", Advanced Optical Materials **6**, 1800274 (2018).

[38] J. D. Sautter, L. Xu, A. E. Miroshnichenko, M. Lysevych, I. Volkovskaya, D. A. Smirnova, R. Camacho-Morales, K. Z. Kamali, F. Karouta, K. Vora, H. H. Tan, M. Kauranen, I. Staude, C. Jagadish, D. N. Neshev, and M. Rahmani, "Tailoring Second-Harmonic Emission from (111)-GaAs Nanoantennas", Nano Letters **19**, 3905–3911 (2019).

[39] K. Trofymchuk, A. Reisch, P. Didier, F. Fras, P. Gilliot, Y. Mely, and A. S. Klymchenko, "Giant light-harvesting nanoantenna for single-molecule detection in ambient light", Nature Photonics **11**, 657–663 (2017).

[40] S. E. Ochmann, C. Vietz, K. Trofymchuk, G. P. Acuna, B. Lalkens, and P. Tinnefeld, "Optical Nanoantenna for Single Molecule-Based Detection of Zika Virus Nucleic Acids without Molecular Multiplication", Analytical Chemistry **89**, 13000–13007 (2017).

[41] G. Marino, A. S. Solntsev, L. Xu, V. F. Gili, L. Carletti, A. N. Poddubny, M. Rahmani, D. A. Smirnova, H. Chen, A. Lemaı tre, G. Zhang, A. V. Zayats, C. D. Angelis, G. Leo, A. A. Sukhorukov, and D. N. Neshev, "Spontaneous photon-pair generation from a dielectric nanoantenna", Optica **6**, 1416 (2019).

[42] P. M. Voroshilov, V. Ovchinnikov, A. Papadimitratos, A. A. Zakhidov, and C. R. Simovski, "Light Trapping Enhancement by Silver Nanoantennas in Organic Solar Cells", ACS Photonics **5**, 1767–1772 (2018).

[43] P. K. Dubey and L. N. Tripathi, "Hybrid metal nanoantenna 2D-material photovoltaic device", Solar Energy Materials and Solar Cells **200**, 109918 (2019).

[44] G. Lozano, S. R. Rodriguez, M. A. Verschuuren, and J. G. Rivas, "Metallic nanostructures for efficient LED lighting", Light Sci. Appl. **5**, e16080–e16080 (2016).

[45] A. Vaskin, R. Kolkowski, A. F. Koenderink, and I. Staude, "Light-emitting metasurfaces", Nanophotonics **8**, 1151–1198 (2019).

[46] S. Bidault, M. Mivelle, and N. Bonod, "Dielectric nanoantennas to manipulate solid-state light emission", Journal of Applied Physics **126**, 094104 (2019).

[47] E. Khaidarov, Z. Liu, R. Paniagua-Domínguez, S. T. Ha, V. Valuckas, X. Liang, Y. Akimov, P. Bai, C. E. Png, H. V. Demir, and A. I. Kuznetsov, "Control of LED Emission with Functional Dielectric Metasurfaces", Laser & Photonics Reviews **14**, 1900235 (2019).

[48] N. Bonod, "Controlling spontaneous emission with dielectric optical antennas", in *Dielectric Metamaterials* (Elsevier, 2020), pp. 109–144.

[49] V. Giannini, A. I. Fernandez-Dominguez, S. C. Heck, and S. A. Maier, "Plasmonic Nanoantennas: Fundamentals and Their Use in Controlling the Radiative Properties of Nanoemitters", Chemical Reviews **111**, 3888–3912 (2011).

[50] I. Staude, A. E. Miroshnichenko, M. Decker, N. T. Fofang, S. Liu, E. Gonzales, J. Dominguez, T. S. Luk, D. N. Neshev, I. Brener, and Y. Kivshar, "Tailoring Directional Scattering through Magnetic and Electric Resonances in Subwavelength Silicon Nanodisks", ACS Nano **7**, 7824–7832 (2013).

[51] V. Remesh, G. Grinblat, Y. Li, S. A. Maier, and N. F. van Hulst, "Coherent Multiphoton Control of Gallium Phosphide Nanodisk Resonances", ACS Photonics **6**, 2487–2491 (2019).

[52] H.-J. Lin, K. de Oliveira Lima, P. Gredin, M. Mortier, L. Billot, Z. Chen, and L. Aigouy, "Fluorescence enhancement near single TiO2 nanodisks", Appl. Phys. Lett. **111**, 251109 (2017).

[53] E. Y. Tiguntseva, G. P. Zograf, F. E. Komissarenko, D. A. Zuev, A. A. Zakhidov, S. V. Makarov, and Y. S. Kivshar, "Light-Emitting Halide Perovskite Nanoantennas", Nano Lett. **18**, 1185–1190 (2018).

[54] G. Mie, "Beiträge zur Optik trüber Medien, speziell kolloidaler Metallösungen", Ann. Phys. **330**, 377–445 (1908).

[55] T. Wriedt and W. Hergert, "Mie Theory 1908 - 2008, Present developments and interdisciplinary aspects of light scattering", Halle, Germany **13.-16. 9** (2008).

[56] M. Decker and I. Staude, "Resonant dielectric nanostructures: a low-loss platform for functional nanophotonics", J. Opt. **18**, 103001 (2016).

[57] Q. Zhao, J. Zhou, F. Zhang, and D. Lippens, "Mie resonance-based dielectric metamaterials", Mater. Today **12**, 60–69 (2009).

[58] E. Y. Tiguntseva, K. L. Koshelev, A. D. Furasova, V. Y. Mikhailovskii, E. V. Ushakova, D. G. Baranov, T. O. Shegai, A. A. Zakhidov, Y. S. Kivshar, and S. V. Makarov, "Single-particle Mie-resonant all-dielectric nanolasers", (2019).

[59] I. M. Hancu, A. G. Curto, M. Castro-López, M. Kuttge, and N. F. van Hulst, "Multipolar Interference for Directed Light Emission", Nano Lett. **14**, 166–171 (2013).

[60] A. V. Kildishev, A. Boltasseva, and V. M. Shalaev, "Planar Photonics with Metasurfaces", Science **339**, 1232009–1232009 (2013).

[61] F. Ding, Y. Yang, R. A. Deshpande, and S. I. Bozhevolnyi, "A review of gap-surface plasmon metasurfaces: fundamentals and applications", Nanophotonics **7**, 1129–1156 (2018).

[62] S. M. Kamali, E. Arbabi, A. Arbabi, and A. Faraon, "A review of dielectric optical metasurfaces for wavefront control", Nanophotonics **7**, 1041–1068 (2018).

[63] P. Lalanne, S. Astilean, P. Chavel, E. Cambril, and H. Launois, "Blazed binary subwavelength gratings with efficiencies larger than those of conventional échelette gratings", Opt. Lett. **23**, 1081–1083 (1998).

[64] F. Aieta, P. Genevet, M. A. Kats, N. Yu, R. Blanchard, Z. Gaburro, and F. Capasso, "Aberration-Free Ultrathin Flat Lenses and Axicons at Telecom Wavelengths Based on Plasmonic Metasurfaces", Nano Lett. **12**, PMID: 22894542, 4932–4936 (2012).

[65] A. Arbabi, Y. Horie, A. J. Ball, M. Bagheri, and A. Faraon, "Subwavelength-thick lenses with high numerical apertures and large efficiency based on high-contrast transmitarrays", Nat. Commun. **6**, 7069 (2015).

[66] M. Khorasaninejad, W. T. Chen, R. C. Devlin, J. Oh, A. Y. Zhu, and F. Capasso, "Metalenses at visible wavelengths: Diffraction-limited focusing and subwavelength resolution imaging", Science **352**, 1190–1194 (2016).

[67] R. R. Grote, T.-Y. Huang, S. A. Mann, D. A. Hopper, A. L. Exarhos, G. G. Lopez, E. C. Garnett, and L. C. Bassett, "Imaging a Nitrogen-Vacancy Center with a Diamond Immersion Metalens", (2017).

[68] P. Genevet, N. Yu, F. Aieta, J. Lin, M. A. Kats, R. Blanchard, M. O. Scully, Z. Gaburro, and F. Capasso, "Ultra-thin plasmonic optical vortex plate based on phase discontinuities", Appl. Phys. Lett. **100**, 013101 (2012).

[69] Y. Yang, W. Wang, P. Moitra, I. I. Kravchenko, D. P. Briggs, and J. Valentine, "Dielectric Meta-Reflectarray for Broadband Linear Polarization Conversion and Optical Vortex Generation", Nano Lett. **14**, PMID: 24547692, 1394–1399 (2014).

[70] K. E. Chong, I. Staude, A. James, J. Dominguez, S. Liu, S. Campione, G. S. Subramania, T. S. Luk, M. Decker, D. N. Neshev, I. Brener, and Y. S. Kivshar, "Polarization-Independent Silicon Metadevices for Efficient Optical Wavefront Control", Nano Lett. **15**, PMID: 26192100, 5369–5374 (2015).

[71] M. I. Shalaev, J. Sun, A. Tsukernik, A. Pandey, K. Nikolskiy, and N. M. Litchinitser, "High-Efficiency All-Dielectric Metasurfaces for Ultracompact Beam Manipulation in Transmission Mode", Nano Lett. **15**, PMID: 26280735, 6261–6266 (2015).

[72] G. Zheng, H. Mühlenbernd, M. Kenney, G. Li, T. Zentgraf, and S. Zhang, "Metasurface holograms reaching 80% efficiency", Nat. Nanotechnol. **10**, 308–312 (2015).

[73] A. Arbabi, Y. Horie, M. Bagheri, and A. Faraon, "Dielectric metasurfaces for complete control of phase and polarization with subwavelength spatial resolution and high transmission", Nat. Nanotechnol. **10**, 937–943 (2015).

[74] K. E. Chong, L. Wang, I. Staude, A. R. James, J. Dominguez, S. Liu, G. S. Subramania, M. Decker, D. N. Neshev, I. Brener, and Y. S. Kivshar, "Efficient Polarization-Insensitive Complex Wavefront Control Using Huygens' Metasurfaces Based on Dielectric Resonant Meta-atoms", ACS Photonics **3**, 514–519 (2016).

[75] L. Wang, S. Kruk, H. Tang, T. Li, I. Kravchenko, D. N. Neshev, and Y. S. Kivshar, "Grayscale transparent metasurface holograms", Optica **3**, 1504–1505 (2016).

[76] G. Lozano, D. J. Louwers, S. R. Rodríguez, S. Murai, O. T. Jansen, M. A. Verschuuren, and J. G. Rivas, "Plasmonics for solid-state lighting: enhanced excitation and directional emission of highly efficient light sources", Light Sci. Appl. **2:e66**, e66–e66 (2013).

[77] J. M. Lupton, B. J. Matterson, I. D. W. Samuel, M. J. Jory, and W. L. Barnes, "Bragg scattering from periodically microstructured light emitting diodes", Appl. Phys. Lett. **77**, 3340–3342 (2000).

[78] G. Vecchi, V. Giannini, and J. G. Rivas, "Shaping the Fluorescent Emission by Lattice Resonances in Plasmonic Crystals of Nanoantennas", Phys. Rev. Lett. **102**, 146807 (2009).

[79] J. S. Biteen, L. A. Sweatlock, H. Mertens, N. S. Lewis, A. Polman, and H. A. Atwater, "Plasmon-enhanced photoluminescence of silicon quantum dots: simulation and experiment", J. Phys. Chem. C **111**, 13372–13377 (2007).

[80] A. Abass, S. R.-K. Rodriguez, T. Ako, T. Aubert, M. Verschuuren, D. V. Thourhout, J. Beeckman, Z. Hens, J. G. Rivas, and B. Maes, "Active Liquid Crystal Tuning of Metallic Nanoantenna Enhanced Light Emission from Colloidal Quantum Dots", Nano Lett. **14**, 5555–5560 (2014).

[81] F. J. G. de Abajo, "Colloquium: Light scattering by particle and hole arrays", Rev. Mod. Phys. **79**, 1267–1290 (2007).

[82] N. Meinzer, W. L. Barnes, and I. R. Hooper, "Plasmonic meta-atoms and metasurfaces", Nat. Photonics **8**, 889–898 (2014).

[83] F. Laux, N. Bonod, and D. Gérard, "Single Emitter Fluorescence Enhancement with Surface Lattice Resonances", J. Phys. Chem. C **121**, 13280–13289 (2017).

[84] V. G. Kravets, A. V. Kabashin, W. L. Barnes, and A. N. Grigorenko, "Plasmonic Surface Lattice Resonances: A Review of Properties and Applications", Chem. Rev. **118**, 5912–5951 (2018).

[85] X. Wang, L. C. Kogos, and R. Paiella, "Giant distributed optical-field enhancements from Mie-resonant lattice surface modes in dielectric metasurfaces", OSA Continuum **2**, 32–42 (2019).

[86] G. Marino, C. Gigli, D. Rocco, A. Lemaître, I. Favero, C. De Angelis, and G. Leo, "Zero-Order Second Harmonic Generation from AlGaAs-on-Insulator Metasurfaces", ACS Photonics **6**, 1226–1231 (2019).

[87] S. Liu, A. Vaskin, S. Campione, O. Wolf, M. B. Sinclair, J. Reno, G. A. Keeler, I. Staude, and I. Brener, "Huygens' Metasurfaces Enabled by Magnetic Dipole Resonance Tuning in Split Dielectric Nanoresonators", Nano Letters **17**, 4297–4303 (2017).

[88] J. Sautter, I. Staude, M. Decker, E. Rusak, D. N. Neshev, I. Brener, and Y. S. Kivshar, "Active Tuning of All-Dielectric Metasurfaces", ACS Nano **9**, 4308–4315 (2015).

[89] W. Liu, J. Zhang, B. Lei, H. Ma, W. Xie, and H. Hu, "Ultra-directional forward scattering by individual core-shell nanoparticles", Optics Express **22**, 16178 (2014).

[90] C. F. Bohren and D. R. Huffman, *Absorption and Scattering of Light by Small Particles* (Wiley, Apr. 1998).

[91] B. Rolly, B. Stout, and N. Bonod, "Boosting the directivity of optical antennas with magnetic and electric dipolar resonant particles", Opt. Express **20**, 20376–20386 (2012).

[92] A. E. Krasnok, C. R. Simovski, P. A. Belov, and Y. S. Kivshar, "Superdirective dielectric nanoantennas", Nanoscale **6**, 7354–7361 (2014).

[93] E. Rusak, I. Staude, M. Decker, J. Sautter, A. E. Miroshnichenko, D. A. Powell, D. N. Neshev, and Y. S. Kivshar, "Hybrid nanoantennas for directional emission enhancement", Appl. Phys. Lett. **105**, 221109 (2014).

[94] A. F. Cihan, A. G. Curto, S. Raza, P. G. Kik, and M. L. Brongersma, "Silicon Mie resonators for highly directional light emission from monolayer MoS_2", Nat. Photonics **12**, 284–290 (2018).

[95] P. R. Wiecha, C. Majorel, C. Girard, A. Arbouet, B. Masenelli, O. Boisron, A. Lecestre, G. Larrieu, V. Paillard, and A. Cuche, "Enhancement of electric and magnetic dipole transition of rare-earth-doped thin films tailored by high-index dielectric nanostructures", Appl. Opt. **58**, 1682–1690 (2019).

[96] M. Kerker, D.-S. Wang, and C. L. Giles, "Electromagnetic scattering by magnetic spheres", J. Opt. Soc. Am. **73**, 765–767 (1983).

[97] M. Decker, I. Staude, M. Falkner, J. Dominguez, D. N. Neshev, I. Brener, T. Pertsch, and Y. S. Kivshar, "High-Efficiency Dielectric Huygens' Surfaces", Advanced Optical Materials **3**, 813–820 (2015).

[98] W. Liu and Y. S. Kivshar, "Generalized Kerker effects in nanophotonics and meta-optics [Invited]", Opt. Express **26**, 13085–13105 (2018).

[99] Z. Zhou, J. Li, R. Su, B. Yao, H. Fang, K. Li, L. Zhou, J. Liu, D. Stellinga, C. P. Reardon, T. F. Krauss, and X. Wang, "Efficient Silicon Metasurfaces for Visible Light", ACS Photonics **4**, 544–551 (2017).

[100] I. M. Fradkin, S. A. Dyakov, and N. A. Gippius, "Fourier modal method for the description of nanoparticle lattices in the dipole approximation", Physical Review B **99** (2019) 10.1103/physrevb.99.075310.

[101] W. Liu and A. E. Miroshnichenko, "Beam Steering with Dielectric Metalattices", ACS Photonics **5**, 1733–1741 (2017).

[102] A. I. Väkeväinen, R. J. Moerland, H. T. Rekola, A.-P. Eskelinen, J.-P. Martikainen, D.-H. Kim, and P. Törmä, "Plasmonic Surface Lattice Resonances at the Strong Coupling Regime", Nano Lett. **14**, 1721–1727 (2013).

[103] P. Lunnemann and A. F. Koenderink, "Dispersion of guided modes in two-dimensional split ring lattices", Phys. Rev. B **90**, 245416 (2014).

[104] Y.-l. Xu, "Electromagnetic scattering by an aggregate of spheres", Applied Optics **34**, 4573 (1995).

[105] M. I. Mishchenko, L. D. Travis, and D. W. Mackowski, "T-matrix computations of light scattering by nonspherical particles: A review", Journal of Quantitative Spectroscopy and Radiative Transfer **55**, 535–575 (1996).

[106] A. F. Koenderink, "Plasmon Nanoparticle Array Waveguides for Single Photon and Single Plasmon Sources", Nano Letters **9**, 4228–4233 (2009).

[107] R. N. S. Suryadharma, M. Fruhnert, I. Fernandez-Corbaton, and C. Rockstuhl, "Studying plasmonic resonance modes of hierarchical self-assembled meta-atoms based on their transfer matrix", Physical Review B **96** (2017) 10.1103/physrevb.96.045406.

[108] A. Rahimzadegan, D. Arslan, R. Suryadharma, S. Fasold, M. Falkner, T. Pertsch, I. Staude, and C. Rockstuhl, "Disorder-Induced Phase Transitions in the Transmission of Dielectric Metasurfaces", Physical Review Letters **122** (2019) 10.1103/physrevlett.122.015702.

[109] W. Zhou and T. W. Odom, "Tunable subradiant lattice plasmons by out-of-plane dipolar interactions", Nature Nanotechnology **6**, 423–427 (2011).

[110] A. Krasnok, S. Glybovski, M. Petrov, S. Makarov, R. Savelev, P. Belov, C. Simovski, and Y. Kivshar, "Demonstration of the enhanced Purcell factor in all-dielectric structures", Applied Physics Letters **108**, 211105 (2016).

[111] S. Liu, A. Vaskin, S. Addamane, B. Leung, M.-C. Tsai, Y. Yang, P. P. Vabishchevich, G. A. Keeler, G. Wang, X. He, Y. Kim, N. F. Hartmann, H. Htoon, S. K. Doorn, M. Zilk, T. Pertsch, G. Balakrishnan, M. B. Sinclair, I. Staude, and I. Brener, "Light-Emitting Metasurfaces: Simultaneous Control of Spontaneous Emission and Far-Field Radiation", Nano Lett. **18**, 6906–6914 (2018).

[112] S. T. Ha, Y. H. Fu, N. K. Emani, Z. Pan, R. M. Bakker, R. Paniagua-Domínguez, and A. I. Kuznetsov, "Directional lasing in resonant semiconductor nanoantenna arrays", Nat. Nanotechnol. **13**, 1042–1047 (2018).

[113] L. Novotny and B. Hecht, "Principles of Nano-Optics", Cambridge University Press (2012) 10.1017/cbo9780511813535.

[114] E. M. Purcell, "Spontaneous emission probabilities at radio frequencies", Phys. Rev. **69**, 681 (1946).

[115] R. Z. Sinan Karaveli, *Encyclopedia of Nanotechnology* (Springer, 2012).

[116] R. Shankar, *Principles of Quantum Mechanics* (Plenum Press, 1994).

[117] D. C. Harris and M. D. Bertolucci, *Symmetry and Spectroscopy* (Oxford University Press, 1985).

[118] D. G. Baranov, R. S. Savelev, S. V. Li, A. E. Krasnok, and A. Alú, "Modifying magnetic dipole spontaneous emission with nanophotonic structures", Laser Photonics Rev. **11**, 1600268 (2017).

[119] S. Karaveli and R. Zia, "Spectral Tuning by Selective Enhancement of Electric and Magnetic Dipole Emission", Phys. Rev. Lett. **106**, 193004 (2011).

[120] P. Anger, P. Bharadwaj, and L. Novotny, "Enhancement and Quenching of Single-Molecule Fluorescence", Phys. Rev. Lett. **96**, 113002 (2006).

[121] F. Kaminski, V. Sandoghdar, and M. Agio, "Finite-Difference Time-Domain Modeling of Decay Rates in the Near Field of Metal Nanostructures", J. Comput. Theor. Nanosci. **4**, 635–643 (2007).

[122] L. Novotny, "Single molecule fluorescence in inhomogeneous environments", Appl. Phys. Lett. **69**, 3806–3808 (1996).

[123] J. J. Wierer, A. David, and M. M. Megens, "III-nitride photonic-crystal light-emitting diodes with high extraction efficiency", Nat. Photonics **3**, 163–169 (2009).

[124] A. F. Koenderink, "Single-Photon Nanoantennas", ACS Photonics **4**, 710–722 (2017).

[125] Y. Yang, I. I. Kravchenko, D. P. Briggs, and J. Valentine, "All-dielectric metasurface analogue of electromagnetically induced transparency", Nat. Commun. **5**, 5753 (2014).

[126] S. Campione, S. Liu, L. I. Basilio, L. K. Warne, W. L. Langston, T. S. Luk, J. R. Wendt, J. L. Reno, G. A. Keeler, I. Brener, and M. B. Sinclair, "Broken Symmetry Dielectric Resonators for High Quality Factor Fano Metasurfaces", ACS Photonics **3**, 2362–2367 (2016).

[127] S. Zhang, E. R. Martins, A. G. Diyaf, J. I. Wilson, G. A. Turnbull, and I. D. Samuel, "Calculation of the emission power distribution of microstructured OLEDs using the reciprocity theorem", Synth. Met. **205**, 127–133 (2015).

[128] P. Grahn, A. Shevchenko, and M. Kaivola, "Electromagnetic multipole theory for optical nanomaterials", New J. Phys. **14**, 093033 (2012).

[129] L. Li, "New formulation of the Fourier modal method for crossed surface-relief gratings", Journal of the Optical Society of America A **14**, 2758 (1997).

[130] J. Turunen and J. Tervo, "Fourier Modal Method and Its Applications to Inverse Diffraction, Near-Field Imaging, and Nonlinear Optics", in *Fringe 2013* (Springer Berlin Heidelberg, 2014), pp. 25–33.

[131] A. Vaskin, J. Bohn, K. E. Chong, T. Bucher, M. Zilk, D.-Y. Choi, D. N. Neshev, Y. S. Kivshar, T. Pertsch, and I. Staude, "Directional and Spectral Shaping of Light Emission with Mie-Resonant Silicon Nanoantenna Arrays", ACS Photonics **5**, 1359–1364 (2018).

[132] J. Chaves, *Introduction to Nonimaging Optics* (CRC Press, 2017).

[133] M. Born, E. Wolf, A. B. Bhatia, P. C. Clemmow, D. Gabor, A. R. Stokes, A. M. Taylor, P. A. Wayman, and W. L. Wilcock, "Principles of Optics", Cambridge University Press (1999).

[134] N. Hartmann, "Coupling of emitters to surface plasmons investigated by back focal plane microscopy", (2013).

[135] M. A. Lieb, J. M. Zavislan, and L. Novotny, "Single-molecule orientations determined by direct emission pattern imaging", J. Opt. Soc. Am. B **21**, 1210–1215 (2004).

[136] J. A. Kurvits, M. Jiang, and R. Zia, "Comparative analysis of imaging configurations and objectives for Fourier microscopy", J. Opt. Soc. Am. A **32**, 2082–2092 (2015).

[137] T. H. Taminiau, S. Karaveli, N. F. van Hulst, and R. Zia, "Quantifying the magnetic nature of light emission", Nat. Commun. **3** (2012) `10.1038/ncomms1984`.

[138] A. H. Schokker and A. F. Koenderink, "Lasing at the band edges of plasmonic lattices", Phys. Rev. B **90**, 155452 (2014).

[139] A. E. Krasnok, A. E. Miroshnichenko, P. A. Belov, and Y. S. Kivshar, "All-dielectric optical nanoantennas", Optics Express **20**, 20599 (2012).

[140] B. Rolly, B. Bebey, S. Bidault, B. Stout, and N. Bonod, "Promoting magnetic dipolar transition in trivalent lanthanide ions with lossless Mie resonances", Phys. Rev. B **85**, 245432 (2012).

[141] W. Zhou, M. Dridi, J. Y. Suh, C. H. Kim, D. T. Co, M. R. Wasielewski, G. C. Schatz, and T. W. Odom, "Lasing action in strongly coupled plasmonic nanocavity arrays", Nat. Nanotechnol. **8**, 506–511 (2013).

[142] I. Staude, V. V. Khardikov, N. T. Fofang, S. Liu, M. Decker, D. N. Neshev, T. S. Luk, I. Brener, and Y. S. Kivshar, "Shaping Photoluminescence Spectra with Magnetoelectric Resonances in All-Dielectric Nanoparticles", ACS Photonics **2**, 172–177 (2015).

[143] X. Zeng, W. Yu, P. Yao, Z. Xi, Y. Lu, and P. Wang, "Metallo-dielectric hybrid antenna for high Purcell factor and radiation efficiency", Optics Express **22**, 14517 (2014).

[144] A. Abass, P. Gutsche, B. Maes, C. Rockstuhl, and E. R. Martins, "Insights into directional scattering: from coupled dipoles to asymmetric dimer nanoantennas", Optics Express **24**, 19638 (2016).

[145] L. Langguth, D. Punj, J. Wenger, and A. F. Koenderink, "Plasmonic Band Structure Controls Single-Molecule Fluorescence", ACS Nano **7**, 8840–8848 (2013).

[146] G. Lozano, G. Grzela, M. A. Verschuuren, M. Ramezani, and J. G. Rivas, "Tailor-made directional emission in nanoimprinted plasmonic-based light-emitting devices", Nanoscale **6**, 9223–9229 (2014).

[147] N. Livneh, M. G. Harats, D. Istrati, H. S. Eisenberg, and R. Rapaport, "Highly Directional Room-Temperature Single Photon Device", Nano Letters **16**, 2527–2532 (2016).

[148] S. K. H. Andersen, S. Bogdanov, O. Makarova, Y. Xuan, M. Y. Shalaginov, A. Boltasseva, S. I. Bozhevolnyi, and V. M. Shalaev, "Hybrid Plasmonic Bullseye Antennas for Efficient Photon Collection", ACS Photonics **5**, 692–698 (2018).

[149] W. Geffcken, "The molar absorption of different ions in glases", Glastechn. berichte **35** (1962).

[150] J. S. Stroud, "Optical Absorption and Color Caused by Selected Cations in High-Density, Lead Silicate Glass", Journal of the American Ceramic Society **54**, 401–406 (1971).

[151] D. Ehrt, P. Ebeling, U. Natura, U. Kohlberg, K. Naumann, and S. Ritter, "Redox equilibria and ultraviolett radiation induced defects in glasses.", Int. Congr. Glass **1** (2001).

[152] F. T. Rabouw, N. M. B. Cogan, A. C. Berends, W. van der Stam, D. Vanmaekelbergh, A. F. Koenderink, T. D. Krauss, and C. de Mello Donega, "Non-blinking single-photon emitters in silica", Scientific Reports **6** (2016) 10.1038/srep21187.

[153] I. H. Malitson, "Interspecimen Comparison of the Refractive Index of Fused Silica", Journal of the Optical Society of America **55**, 1205 (1965).

[154] D. Arslan, K. E. Chong, A. E. Miroshnichenko, D.-Y. Choi, D. N. Neshev, T. Pertsch, Y. S. Kivshar, and I. Staude, "Angle-selective all-dielectric Huygens' metasurfaces", Journal of Physics D: Applied Physics **50**, 434002 (2017).

[155] T. Bucher, A. Vaskin, R. Mupparapu, F. J. F. Löchner, A. George, K. E. Chong, S. Fasold, C. Neumann, D.-Y. Choi, F. Eilenberger, F. Setzpfandt, Y. S. Kivshar, T. Pertsch, A. Turchanin, and I. Staude, "Tailoring Photoluminescence from MoS_2 Monolayers by Mie-Resonant Metasurfaces", ACS Photonics (2019).

[156] C. Zhang, Y. Xu, J. Liu, J. Li, J. Xiang, H. Li, J. Li, Q. Dai, S. Lan, and A. E. Miroshnichenko, "Lighting up silicon nanoparticles with Mie resonances", Nature communications **9**, 2964 (2018).

[157] D. Maystre, "Theory of Wood's Anomalies", in *Plasmonics* (Springer Berlin Heidelberg, 2012), pp. 39–83.

[158] A. I. Kuznetsov, A. E. Miroshnichenko, M. L. Brongersma, Y. S. Kivshar, and B. Luk'yanchuk, "Optically resonant dielectric nanostructures", Science **354** (2016) 10.1126/science.aag2472.

[159] V. Rutckaia, F. Heyroth, A. Novikov, M. Shaleev, M. Petrov, and J. Schilling, "Quantum Dot Emission Driven by Mie Resonances in Silicon Nanostructures", Nano Lett. **17**, 6886–6892 (2017).

[160] T. Skauli, P. S. Kuo, K. L. Vodopyanov, T. J. Pinguet, O. Levi, L. A. Eyres, J. S. Harris, M. M. Fejer, B. Gerard, L. Becouarn, and E. Lallier, "Improved dispersion relations for GaAs and applications to nonlinear optics", Journal of Applied Physics **94**, 6447–6455 (2003).

[161] F. J. F. Löchner, A. N. Fedotova, S. Liu, G. A. Keeler, G. M. Peake, S. Saravi, M. R. Shcherbakov, S. Burger, A. A. Fedyanin, I. Brener, T. Pertsch, F. Setzpfandt, and I. Staude, "Polarization-Dependent Second Harmonic Diffraction from Resonant GaAs Metasurfaces", ACS Photonics **5**, 1786–1793 (2018).

[162] A. Leitis, A. Tittl, M. Liu, B. H. Lee, M. B. Gu, Y. S. Kivshar, and H. Altug, "Angle-multiplexed all-dielectric metasurfaces for broadband molecular fingerprint retrieval", Science Advances **5**, eaaw2871 (2019).

[163] A. H. Schokker and A. F. Koenderink, "Lasing at the band edges of plasmonic lattices", Phys. Rev. B **90** (2014) 10.1103/physrevb.90.155452.

[164] A. H. Schokker, F. van Riggelen, Y. Hadad, A. Alú, and A. F. Koenderink, "Systematic study of the hybrid plasmonic-photonic band structure underlying lasing action of diffractive plasmon particle lattices", Phys. Rev. B **95**, 085409 (2017).

[165] A. Kodigala, T. Lepetit, Q. Gu, B. Bahari, Y. Fainman, and B. Kanté, "Lasing action from photonic bound states in continuum", Nature **541**, 196–199 (2017).

[166] G. W. Castellanos, P. Bai, and J. G. Rivas, "Lattice resonances in dielectric metasurfaces", Journal of Applied Physics **125**, 213105 (2019).

[167] M. Kasperczyk, S. Person, D. Ananias, L. D. Carlos, and L. Novotny, "Excitation of Magnetic Dipole Transitions at Optical Frequencies", Phys. Rev. Lett. **114**, 163903 (2015).

[168] N. R. Brewer, Z. N. Buckholtz, Z. J. Simmons, E. A. Mueller, and D. D. Yavuz, "Coherent Magnetic Response at Optical Frequencies Using Atomic Transitions", Phys. Rev. X **7**, 011005 (2017).

[169] R. Hussain, S. S. Kruk, C. E. Bonner, M. A. Noginov, I. Staude, Y. S. Kivshar, N. Noginova, and D. N. Neshev, "Enhancing Eu3+ magnetic dipole emission by resonant plasmonic nanostructures", Optics Letters **40**, 1659 (2015).

[170] V. I. Tsaryuk, K. P. Zhuravlev, V. F. Zolin, V. A. Kudryashova, J. Legendziewicz, and R. Szostak, "Luminescence efficiency of aromatic carboxylates of europium and terbium when methylene bridges and nitro groups are present in the ligands", J. Appl. Spectrosc. **74**, 51–59 (2007).

[171] A. Vaskin, S. Mashhadi, M. Steinert, K. E. Chong, D. Keene, S. Nanz, A. Abass, E. Rusak, D.-Y. Choi, I. Fernandez-Corbaton, T. Pertsch, C. Rockstuhl, M. A. Noginov, Y. S. Kivshar, D. N. Neshev, N. Noginova, and I. Staude, "Manipulation of Magnetic Dipole Emission from Eu3+ with Mie-Resonant Dielectric Metasurfaces", Nano Lett. **19**, 1015–1022 (2019).

[172] N. Noginova, G. Zhu, M. Mavy, and M. A. Noginov, "Magnetic dipole based systems for probing optical magnetism", J. Appl. Phys. **103**, 07E901 (2008).

[173] R. Hussain, D. Keene, N. Noginova, and M. Durach, "Spontaneous emission of electric and magnetic dipoles in the vicinity of thin and thick metal", Opt. Express **22**, 7744–7755 (2014).

[174] L. Aigouy, A. Cazé, P. Gredin, M. Mortier, and R. Carminati, "Mapping and Quantifying Electric and Magnetic Dipole Luminescence at the Nanoscale", Phys. Rev. Lett. **113**, 076101 (2014).

[175] B. Choi, M. Iwanaga, Y. Sugimoto, K. Sakoda, and H. T. Miyazaki, "Selective Plasmonic Enhancement of Electric- and Magnetic-Dipole Radiations of Er Ions", Nano Lett. **16**, 5191–5196 (2016).

[176] A. I. Kuznetsov, A. E. Miroshnichenko, M. L. Brongersma, Y. S. Kivshar, and B. Luk'yanchuk, "Optically resonant dielectric nanostructures", Science **354**, aag2472 (2016).

[177] M. K. Schmidt, R. Esteban, J. J. Sáenz, I. Suárez-Lacalle, S. Mackowski, and J. Aizpurua, "Dielectric antennas - a suitable platform for controlling magnetic dipolar emission", Opt. Express **20**, 13636–13650 (2012).

[178] X. Zambrana-Puyalto and N. Bonod, "Purcell factor of spherical Mie resonators", Phys. Rev. B **91**, 195422 (2015).

[179] T. Feng, Y. Xu, Z. Liang, and W. Zhang, "All-dielectric hollow nanodisk for tailoring magnetic dipole emission", Opt. Lett. **41**, 5011 (2016).

[180] J. Bohn, T. Bucher, K. E. Chong, A. Komar, D.-Y. Choi, D. N. Neshev, Y. S. Kivshar, T. Pertsch, and I. Staude, "Active Tuning of Spontaneous Emission by Mie-Resonant Dielectric Metasurfaces", Nano Lett. **18**, 3461–3465 (2018).

[181] K. Wang, L. Gao, and C. Huang, "Optical properties of the highly ordered Langmuir–Blodgett film of a strongly luminescent Eu(III) complex", Journal of Photochemistry and Photobiology A: Chemistry **156**, 39–43 (2003).

[182] A. Vaskin, S. Liu, S. Addamane, B. Leung, M.-C. Tsai, Y. Yang, P. P. Vabishchevich, G. A. Keeler, G. Wang, X. He, Y. Kim, N. F. Hartmann, H. Htoon, S. K. Doorn, M. Zilk, T. Pertsch, G. Balakrishnan, M. B. Sinclair, I. Brener, and I. Staude, "Manipulation of quantum dot emission with semiconductor metasurfaces exhibiting magnetic quadrupole resonances.", To be submitted **x**, xxxx–xxxx (2020).

[183] M. R. Shcherbakov, S. Liu, V. V. Zubyuk, A. Vaskin, P. P. Vabishchevich, G. Keeler, T. Pertsch, T. V. Dolgova, I. Staude, I. Brener, and A. A. Fedyanin, "Ultrafast all-optical tuning of direct-gap semiconductor metasurfaces", Nature Communications **8** (2017).

Abbreviations and conventions

1D	One dimensional
2D	Two dimensional
3D	Three dimensional
AlGaAs	Aluminium Gallium Arsenide
AlGaO	Aluminium Gallium Oxide
BFP	Back focal plane
CCD	Charge coupled device
CO	Collection optics
CW	Continuous wave
ED	Electric dipole
EMCCD	Electron multiplying CCD
EQ	Electric quadrupole
Eu^{3+}	Trivalent Europium ions
$Eu(TTA)_3L18$	(tris(α-henoyltrifluoroacetone)-(1-octadecyl-2(-2-pyridyl)benzimidazole)europium(III))
FEM	Finite element method
FFP	Front focal plane
FIB	Focused ion beam
FMM	Fourier modal method
FWHM	Full width at half maximum
GaAs	Gallium Arsenide
GaP	Gallium Phosphide
He-Cd	Helium Cadmium
HF	Hydrofluoric acid
HMDS	hexamethyldisilazane

HSQ	Hydrogen silsesquioxane
ICP	Inductively coupled plasma
InAs	Indium Arsenide
InGaAs	Indium Gallium Arsenide
ITO	Indium tin oxide
LED	Light emitting device
LDOS	Local density of states
LiDAR	Light detection and ranging
MBE	Molecular beam epitaxy
MD	Magnetic dipole
ML	Monolayer
MQ	Magnetic quadrupole
NA	Numerical aperture
NIR	Near-infrared
PL	Photoluminescence
PEC	Perfect electric conductor
PMC	Perfect magnetic conductor
PML	Perfectly matched layer
QDs	Quantum dots
Q-factor	Quality factor
SEM	Scanning electron microscope
Si	Silicon
SiO_2	Silicon dioxide
TE	Transverse electric
TiO_2	Titanium dioxide
TM	Transverse magnetic
TMAH	Tetramethylammonium hydroxide
USA	United States of America
UV	Ultraviolet

Acknowledgement

I want to thank Isabelle Staude, my supervisor, for her patience, willingness to help and support at any stage of the doctorate. Working with her allowed me to gain a precious experience and grow as a self-sufficient researcher. The scientific discussions with Isabelle were creative and inspiring.

I sincerely acknowledge my mom, Svetlana Vaskina. She is always supporting me and gives a confidence in my life. I want to thank Igal Brener for the great opportunities that he provided. I want to thank Frank Setzpfandt and Thomas Pertsch for providing a friendly working environment. I would like to thank my colleagues for their help, fruitful discussions and being good friends: Dennis Arslan, Tobias Bucher, Jürgen Sautter, Justus Bohn, Anna Fedotova, Valerio Gili, Polina P. Vabishchevich, Sheng Liu and Ayesheh Bashiri.

This manuscript is based on the research done in collaboration with outstanding scientists from Germany, USA and Australia. The most significant contributions are listed below:

- FMM script was developed by Matthias Zilk from Friedrich Schiller University Jena.
- a-Si:H nanocylinder metasurface samples were fabricated and characterized (SEM imaging and transmittance spectroscopy) by Katie E. Chong.
- PL spectroscopy of fluorescence emission coupled to a-Si:H nanocylinder metasurfaces was performed by Justus Bohn from Friedrich Schiller University Jena.
- Layered wafer used for GaAs metasurfaces were grown by Sadhvikas Addamane from Sandia National Laboratories.
- GaAs metasurface samples were fabricated and characterized (SEM imaging, reflectance and PL spectroscopy) by Sheng Liu from Sandia National Laboratories.
- Time-resolved fluorescence was measured by Xiaowei He and Younghee Kim from Los Alamos National Laboratory.
- a-Si:H nanocylinder metasurface samples were covered by Eu^{3+} containing polymer and PL microscopy images were taken by Soheila Mashhadi from Norfolk State University.

The data presented in this manuscript, except for Figures 1.1, 1.2 and 2.9, is obtained by the author if not specified otherwise. The author also personally performed the linear and PL spectra measurements as well as the fabrication of GaAs metasurfaces for side projects. The results of these projects is out of the scope of this manuscript.

Ehrenwörtliche Erklärung

Ich erkläre hiermit ehrenwörtlich, dass ich die vorliegende Arbeit selbständig, ohne unzulässige Hilfe Dritter und ohne Benutzung anderer als der angegebenen Hilfsmittel und Literatur angefertigt habe. Die aus anderen Quellen direkt oder indirekt übernommenen Daten und Konzepte sind unter Angabe der Quelle gekennzeichnet. Bei der Auswahl und Auswertung folgenden Materials haben mir die nachstehend aufgeführten Personen in der jeweils beschriebenen Weise unentgeltlich geholfen:

- 1. Justus Bohn
- 2. Katie E. Chong.
- 3. Sheng Liu
- 4. Soheila Mashhadi
- 5. Matthias Zilk
- 6. Sadhvikas Addamane
- 7. Xiaowei He

Weitere Personen waren an der inhaltlich-materiellen Erstellung der vorliegenden Arbeit nicht beteiligt. Insbesondere habe ich hierfür nicht die entgeltliche Hilfe von Vermittlungs- bzw. Beratungsdiensten (Promotionsberater oder andere Personen) in Anspruch genommen. Niemand hat von mir unmittelbar oder mittelbar geldwerte Leistungen für Arbeiten erhalten, die im Zusammenhang mit dem Inhalt der vorgelegten Dissertation stehen. Die Arbeit wurde bisher weder im In- noch im Ausland in gleicher oder ähnlicher Form einer anderen Prüfungsbehörde vorgelegt. Die geltende Promotionsordnung der Physikalisch-Astronomischen Fakultät ist mir bekannt. Ich versichere ehrenwörtlich, dass ich nach bestem Wissen die reine Wahrheit gesagt und nichts verschwiegen habe.